RECOMMENDED MEASUREMENT AND INSTRUMENT CHARACTERISTICS FOR AN EARTH VENTURE CONTINUITY EARTH RADIATION BUDGET INSTRUMENT

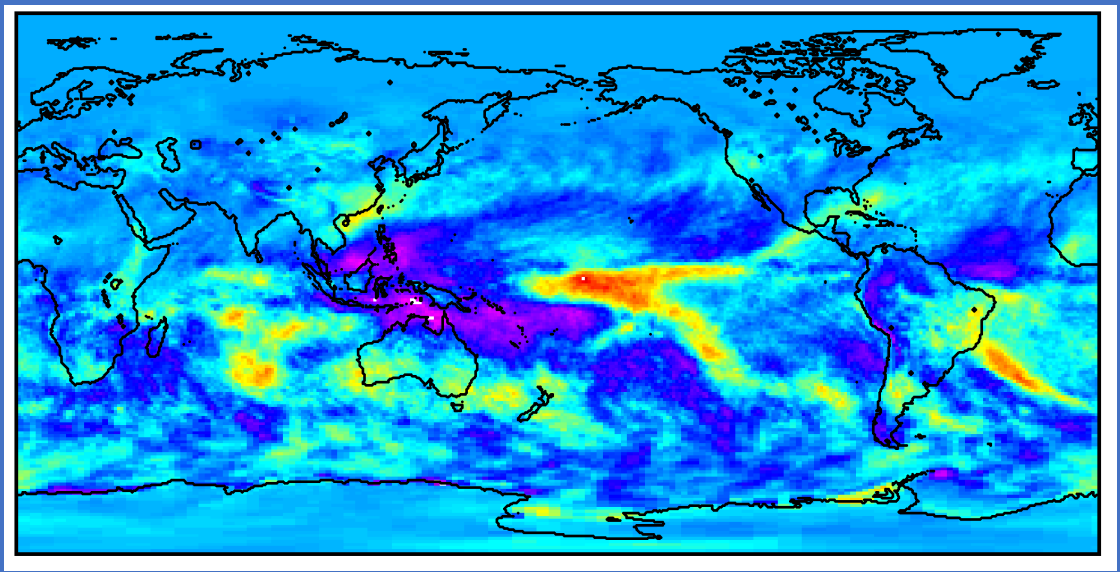

National Aeronautics and Space Administration

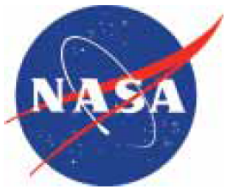

Recommended Measurement and Instrument Characteristics for an Earth Venture Continuity Earth Radiation Budget Instrument

Report of the Earth Venture Continuity
Radiation Budget Science Working Group

Anum Barki, NASA Langley Research Center
Chris Bonniksen, NASA Management Office, JPL
James Butler, NASA Goddard Space Flight Center
David Considine, NASA Headquarters
David Doelling, NASA Langley Research Center
Jonathan Gleason, NASA Langley Research Center
David Johnson, NASA Langley Research Center
Seiji Kato, NASA Langley Research Center
Norman Loeb, NASA Langley Research Center
Lazaros Oreopoulos, NASA Goddard Space Flight Center
Kory Priestley, NASA Langley Research Center
Venkatachalam Ramaswamy, NOAA Geophysical Fluid Dynamics Laboratory
William L. Smith, NASA Langley Research Center
Paul Stackhouse, NASA Langley Research Center
Wenying Su, NASA Langley Research Center
Patrick Taylor, NASA Langley Research Center
Kurtis Thome, NASA Goddard Space Flight Center
George Tselioudis, NASA Goddard Institute for Space Studies
Bruce Wielicki, NASA Langley Research Center
Dong Wu, NASA Goddard Space Flight Center
Xiaoxiong “Jack” Xiong, NASA Goddard Space Flight Center
Xuepeng “Tom” Zhao, NOAA National Centers for Environmental Information

September 2018

Contents

Executive Summary

Earth's climate is determined by the exchange of radiant energy between the Sun, Earth and space. If Earth absorbs more energy from the sun as visible light than it emits to space as thermal infrared radiation, it will eventually warm up, altering precipitation patterns, sea level, and extreme weather. Earth's radiation budget (ERB) describes how radiant energy from the Sun and thermal infrared radiation emitted by Earth are distributed at the surface, within the atmosphere and at the top-of-atmosphere (TOA). State-of-the-art climate models project large changes in our climate due to changes in ERB that result from increases in well-mixed greenhouse gases, changes in aerosol concentration and land-usage. The need to monitor ERB and the components of the climate system that it interacts with cannot be overstated: ERB observations provide crucial constraints on climate model projections of future warming and enable a process-level understanding of the energy flow within the climate system and how it is changing. Observations of ERB were amongst the first recorded from space at the start of the satellite era in the 1950s and have been a key NASA priority ever since.

The longest continuous global observational record of ERB from instruments designed to measure ERB is from the Clouds and the Earth's Radiant Energy System (CERES), which starts in 2000. CERES broadband radiometers, moderate resolution spectral imagers, and meteorological and aerosol assimilation data are combined to provide climate data records (CDRs) of ERB at the TOA, surface and various levels in the atmosphere. The CERES data products provide radiative fluxes and the corresponding cloud, aerosol and meteorological data over a range of time-space scales, from instantaneous footprint (Levels 1b and 2) to global monthly (Levels 3 and 3b). They support research in many areas, including: Earth's energy imbalance, climate feedback, aerosol radiative forcing, regional energy budgets, atmospheric and oceanic energy transports, surface and atmospheric energy balance, general circulation, polar climate and climate model evaluation.

Six CERES instruments are in orbit flying aboard the Terra, Aqua, Suomi National Polar-orbiting Partnership (SNPP) and NOAA-20 satellites. Five of the six CERES instruments are well beyond their nominal five-year design lifetime. As a result, there is a 50% probability that a data gap in the ERB record will occur in the mid-2020s unless another ERB instrument is launched. The intended follow-on to CERES—the Radiation Budget Instrument (RBI)—in development since 2014, was cancelled by NASA HQ in January 2018 due to cost overruns. RBI's cancellation occurred immediately following release of the 2017 Earth Science Decadal Survey (DS), which had recommended that RBI be part of the Earth Science "Program of Record" over the next decade. NASA Earth Science Division (ESD) decided to replace RBI with a lower cost alternative through the new Earth Venture-Continuity (EVC) program, introduced in the 2017 DS to provide competed, cost-capped small missions for sustained observations of selected climate variables. The Announcement of Opportunity (AO) for the EVC ERB instrument is expected in December 2018. Following launch of the EVC ERB instrument and successful completion of its Post-Launch Assessment Review (PLAR), measurements from the new EVC ERB instrument will be ingested into the existing CERES processing system to extend the CERES ERB record. NASA HQ will assign responsibility for operation, health and safety monitoring, instrument calibration and generation of higher level data products to the Radiation Budget Science Project (RBSP) at NASA Langley, which also has responsibility in these areas for CERES.

In preparation for the AO, NASA HQ formed an ERB Science Working Group (SWG) tasked with generating instrument and measurement characteristics that would allow continuation of the CERES ERB CDR under the EVC ERB opportunity. This report summarizes the recommendations of the ERB SWG. It builds upon three earlier community workshop reports: "Achieving Satellite Instrument Calibration for Climate Change (ASIC3)", held in 2002 and 2006, and "Continuity of Earth Radiation Budget (CERB) Observations: Post-CERES Requirements", held in 2011.

Observational Characteristics Recommendations:

Since the aim of the EVC ERB instrument is to continue the CERES record, the ERB SWG recommends that the EVC ERB instrument have many of the same characteristics as CERES. The ultimate goal is to provide an instrument that is "backwards compatible" with CERES to avoid any discontinuities or artificial jumps in the ERB CDR. Following is a list of recommended minimum characteristics for the EVC ERB instrument:

- Filtered radiances should be provided in the shortwave (SW; wavelengths between 0.3 and 5 μm), total (TOT; wavelengths between 0.3 and >100 μm), and longwave (LW; wavelengths between 5 and >35 μm) regions.
- The spatial resolution of CERES is 20 km (nadir equivalent circle diameter) on Terra and Aqua and 24 km on SNPP and NOAA-20. For the EVC ERB instrument, the ERB SWG recommends a spatial resolution that is 25 km or better. Furthermore, the fields-of-view for different channels must be co-registered.
- It is recommended that the EVC ERB instrument provide near-global coverage daily, which is consistent with what CERES provides when in crosstrack mode.
- CERES can be commanded to operate in crosstrack and alongtrack modes as well as rotate in azimuth as it scans in elevation. While it would be preferable if the EVC ERB instrument retained this capability, the ERB SWG recognizes that this may be more challenging technically and therefore more costly. Consequently, the ERB SWG recommends that at a minimum the new EVC ERB instrument operate in crosstrack or fixed azimuth plane mode.
- The radiometric accuracy of the EVC ERB instrument should be 1% SW and 0.5% for TOT and LW (k=1). Radiometric stability should be 0.3%/decade (k=1). The levels of accuracy and stability should be met under all-sky conditions as well as individual scene types (e.g., clear ocean, land, snow, etc.).
- EVC ERB should include onboard calibration for detecting and correcting sensor calibration drifts across the spectral range of each channel.
- EVC should enable periodic solar and lunar calibration to demonstrate accuracy and stability, and cross calibrate and validate with on-board sources.
- Instrument characterization and ground calibration of its spectral, spatial, temporal and radiometric properties need to be traceable to NIST standards. The ground calibration campaign should determine the absolute calibration for the broadband sensors and tie the on-board calibration sources to NIST traceable references on the ground. Pre-launch

calibration activities should also verify the instrument's short-term variability, drift and linearity.

- The EVC ERB instrument should be Class C with a 5-year nominal lifetime.
- As all CERES instruments except those on Terra are in an ascending sun-synchronous orbit with a 13:30 local equator crossing time, it is recommended that the EVC ERB be within 15 min of a 13:30 local equator crossing time.
- The new EVC ERB instrument should provide a minimum of 6 months overlap with at least one of the remaining CERES instruments.
- CERES data processing involves a high level of data fusion that requires coincident imager measurements (MODIS or VIIRS) to provide detailed information about the properties of the scene observed by CERES. It is recommended that the EVC ERB instrument fly on the same satellite or within 3 minutes of an imager that has equivalent spatial resolution and spectral channels as VIIRS (see Table 5-2).

Programmatic Recommendations:

- Key members of the RBSP Instrument Working Group should participate in pre-flight instrument calibration and characterization activities. This will provide critical, first-hand knowledge to the team and enable efficient instrument operations.
- In order to ingest a new EVC ERB instrument into the existing CERES processing system, the EVC ERB instrument provider will need to work closely with the RBSP instrument and data management teams to ensure all the required pre-launch information is collected, instructions and software to operate the instrument are ready at launch, and ERB data needed for the Levels 0, 1B and 2 stages of the processing are captured.
- The instrument development group should use a structured content management system to organize and track configuration of information specific to pre-flight characterization and calibration of the instrument. This information will be key to on-orbit operation, calibration and anomaly resolution and should be made available to the RBSP for use during instrument operations.
- The EVC ERB instrument provider should use the existing ESDIS EDOS system at GSFC to produce Level 0 data if the instrument were to fly on the JPSS-3 platform. Data connectivity is already in place between the JPSS Common Ground System and EDOS and again between EDOS and the ASDC at Langley. Similarly, EDOS is already equipped to produce L0 files for other JPSS missions and the plan was to model this approach for RBI, so the hooks are in place to make this process easy and efficient should this option be exercised.

1. Introduction

Earth's Radiation Budget (or Balance), henceforth ERB, represents a balance between incoming solar radiation reaching the top-of-atmosphere (TOA) and outgoing reflected solar and thermal radiant energy emitted by the Earth–atmosphere system. When the climate system is forced by natural or anthropogenic factors, an imbalance in the TOA ERB results. Examples of natural forcings include changes in solar output and volcanic eruptions, while anthropogenic forcings include emissions of greenhouse gases and aerosols, and changes in land-usage (IPCC, 2013). A positive (negative) Earth Energy Imbalance (EEI) means the Earth is absorbing more (less) solar energy than it is emitting as infrared radiation, causing it to eventually warm (cool). Forcing of the climate system results in perturbations of Earth's energy flows in ways that are not yet fully understood with potentially grave consequences for humanity. At the surface, the radiation budget determines how much energy is available to drive the hydrological cycle: the surface ERB sets the energy limit that enables water to evaporate into the atmosphere and eventually return as precipitation. Regional imbalances in TOA net radiation give rise to atmospheric and oceanic circulations, which transport heat from regions with a surplus of radiant energy (e.g., low latitudes) to regions that have a deficit in radiant energy (high latitudes). Superimposed on the climate change signal associated with radiative forcing is the large internal variability of the climate system, which also causes variations in the ERB. Internal variations can occur over a range of time–space scales, associated with synoptic weather events, atmosphere–ocean interactions (e.g., El Niño–Southern Oscillation, ENSO), volcanic eruptions, and low-frequency multidecadal fluctuations (e.g., Pacific decadal oscillation, PDO).

In order to make reliable projections of climate and plan as a society for potentially significant environmental changes, a process-level understanding of the flow of energy within the climate system and how it interacts with Earth's subsystems (atmosphere, hydrosphere, lithosphere and biosphere) is needed. In this context, accurate long-term ERB observations play a key role. In addition to helping improve our understanding of climate processes, they provide critical constraints on climate model projections of future warming. Sustained, accurate observations of ERB are thus an essential part of the Earth observing system. This is acknowledged in multiple national and international community reports and publications, including the recent 2017 Decadal Survey (DS) (NRC, 2007; NASEM, 2018; GCOS, 2010; Trenberth et al., 2013; Wielicki et al., 2013; von Schuckmann et al., 2016; Weatherhead et al., 2018).

Satellite observations of ERB began in the late 1950s, at the start of the satellite era (House et al., 1986; also see Appendix A). Scientists had long wanted to quantify Earth's albedo, determine how much thermal infrared radiation Earth emits, and describe how energy is distributed and exchanged within the climate system (Hunt et al., 1986). The Explorer-7 satellite provided the first usable wide field-of-view (WFOV) nonscanning measurements of the total (reflected solar and emitted thermal) radiation from Earth. The 1960s was a period of rapid advances with the Television Infrared Observational Satellite series, which brought together broadband ERB instruments and five-channel scanning radiometers on the same platform for the first time. Unfortunately, the early satellite missions had lifetimes limited to roughly 1 year or less. It was not until the Nimbus-7 ERB mission in the late 1970s that a multi-year ERB dataset was collected. Nimbus-7 ERB included total solar irradiance, reflected solar, and emitted thermal measurements from both narrow-field-of-view (NFOV) scanner and WFOV nonscanner

instruments. In the 1980s, the Earth Radiation Budget Experiment (ERBE) flew on multiple satellites and included NFOV and WFOV ERB radiometers and solar radiometers. On the NOAA-9 and NOAA-10 satellites, ERBE instruments flew on the same satellite as AVHRR imagers. The ERBE WFOV instrument on Earth Radiation Budget Satellite (ERBS) was operational from 1985 to 2000 (Wong et al., 2006). During the 1990s, there were two launches of the Scanner Radiation Budget (ScaRaB) instrument onboard the Meteor and Resurs satellites, which lasted less than 1 year due to spacecraft anomalies. A ScaRaB instrument is currently flying on the Megha-Tropiques mission (Roca et al., 2015), which provides coverage over the Tropics from an inclined orbit. The only geostationary ERB instruments to fly are the four Geostationary Earth Radiation Budget (GERB) instruments (Harries et al., 2005), which were successively launched on the EUMETSAT Meteosat Second Generation geostationary satellites, covering Africa, South America and Europe.

Following the ERBE experience, NASA decided to build multiple NFOV scanner instruments as part of the Clouds and the Earth's Radiant Energy System (CERES) (Wielicki et al., 1995; Wielicki et al., 1996). The choice of NFOV over WFOV was deliberate based upon science and practical considerations. ERBE WFOV instruments presented significant calibration challenges (especially thermal offsets), and due to their coarse spatial resolution of thousands of kilometers, provided limited scientific return compared to what had been obtained with the ERBE NFOV scanners. The pre-launch hopes that the WFOV instruments would achieve absolute accuracies sufficient to directly measure EEI were never realized owing to calibration and algorithm uncertainties (Wong et al., 2018). To this day, the same challenges exist in modern WFOV instrument designs.

CERES scanner instruments built in the 1990s have launched on TRMM, Terra, Aqua, SNPP and NOAA-20 satellites. Unlike most of the earlier missions involving scanners, CERES instruments have lasted remarkably long. While the CERES Proto-flight model (PFM) on TRMM failed after only 8 months of operation, CERES FM1-FM5 are all well beyond their nominal 5-year design lifetime, at 18, 16 and 7 years for Terra, Aqua and SNPP, respectively. CERES FM6 on NOAA-20 launched in 2017. CERES instruments fly alongside imagers (MODIS, VIIRS), which play a critical role in CERES data product generation. The CERES record starts in 2000 and represents the longest continuous global ERB record available. The observations from CERES have provided a wealth of information for climate model evaluation and improved understanding of NASA's focus areas: climate variability and change, water and energy cycle, weather and applied sciences. With improved understanding about the coupled nature of the climate system, many more scientific questions involving ERB have emerged since the beginning of the satellite era. The questions are primarily associated with how Earth's energy budget is changing and how clouds, aerosols, surface, atmosphere-ocean circulations, and atmosphere-ocean-land processes respond and further alter Earth's energy budget (Boucher et al., 2013; Bony et al., 2015; Stevens and Bony, 2013). To help address these questions, NASA's Radiation Budget Science Project (RBSP) (also known as the CERES Science Team) is producing a comprehensive ERB Climate Data Record (CDR) from CERES and other observational datasets (Loeb et al., 2016a). The RBSP is the only project worldwide whose prime objective is to produce global, climate-quality ERB data from dedicated ERB satellite instruments.

In recognition of the continued scientific importance of ERB and NASA's significant contributions, the 2007 and 2017 DS reports (NRC, 2007; NASEM, 2018) recommended that ERB satellite observations be continued beyond CERES. The 2017 DS identified the CERES data record

and Radiation Budget Instrument (RBI) follow-on as the primary means to address Science Question C-2: "*How can we reduce the uncertainty in the amount of future warming of the Earth as a function of fossil fuel emissions, improve our ability to predict local and regional climate response to natural and anthropogenic forcings, and reduce the uncertainty in global climate sensitivity that drives uncertainty in future economic impacts and mitigation/adaptation strategies?*"

Following the release of the 2017 DS, the RBI instrument was cancelled by NASA HQ due to cost overruns. In light of this, and in response to the DS recommendation that ERB observations be continued beyond CERES, NASA HQ formed an ERB Science Working Group (SWG), which was tasked with defining the instrument and measurement characteristics needed in order to extend the ERB CDR beyond CERES under a cost-capped Earth Venture-Continuity opportunity, anticipated to be released in December 2018. This report summarizes the findings of the ERB SWG. It builds upon three earlier community workshop reports on ERB observational requirements. The first two, "Achieving Satellite Instrument Calibration for Climate Change ($ASIC^3$)", were held in 2002 and 2006 and are documented both as workshop reports and publications (Ohring et al., 2004, 2005, 2007). The second workshop, "*Continuity of Earth Radiation Budget (CERB) Observations: Post-CERES Requirements*", was held in 2011 and documented in Bates and Zhao (2011).

Since the prime objective of ERB continuity is to continue an existing ERB CDR, it is worthwhile defining what is meant by "CDR" and "continuity". According to the U.S. National Research Council (NRC, 2004), a CDR is defined as "*a time series of measurements of sufficient length, consistency, and continuity to determine climate variability and change*". Here, "continuity" refers to more than merely acquiring measurements of a "continuity variable" without regard to the current characteristics of the measurement. According to the NRC Continuity Report (NASEM, 2015), continuity of an Earth measurement "*exists when the quality of the measurement for a specific quantified Earth science objective is maintained over the required temporal and spatial domain set by the objective*". In this context, "quality" is characterized by the "*combined standard uncertainty, which includes instrument calibration uncertainty, repeatability, time and space sampling, and data systems and delivery for climate variables (algorithms, reprocessing, and availability)*". A multi-instrument measurement campaign aimed at producing a CDR is thus subject to the requirement that subsequent instruments produce "backward compatible" observations that allow continuation of the CDR without introducing discontinuities in the record.

In Section 2 of this report, we provide some background information on NASA's current ERB observations and describe a roadmap for future ERB observations through the new Earth Venture-Continuity opportunity. We also provide more detail about the purpose, composition and objectives of the ERB SWG, and discuss the likelihood of a data gap in the ERB record given the current and planned ERB instruments. This is followed in Section 3 by an overview of the science addressed by ERB observations. In Section 4, we focus specifically on how a new ERB instrument would feed into the existing processing system in order to extend the CERES CDR. A summary of the observational characteristics recommended by the ERB SWG is given in Section 5. Additional background information and detail about some of the areas covered in the main body of this report are provided as appendices: Appendix A provides a brief history of ERB observations; Appendix B describes the CERES instrument characteristics, algorithms and data

products; Appendix C lists selected science highlights involving CERES datasets that have been published in peer-reviewed scientific journals.

2. Status of Current and Future ERB Observations

2.1 CERES

CERES instruments are currently flying on Terra, Aqua, SNPP, and NOAA-20 satellites (Figure 2.1). CERES instruments FM1-FM5 are all well beyond their nominal mission lifetimes, and FM6 on NOAA-20 launched in November 2017. Terra is in a descending sun-synchronous orbit with an equator-crossing time of 10:30 local time, while Aqua, SNPP, and NOAA-20 are in ascending sun-synchronous orbits with a 13:30 local time equator-crossing time. CERES FM1-FM6 provide global coverage daily and fly alongside imagers that measure spectral radiances at a spatial resolution of 1 km or better (MODIS or VIIRS).

CERES instruments measure filtered radiances. A filtered radiance is the radiance incident at the instrument aperture convolved with the spectral responsivity of the instrument. An unfiltered radiance has had the instrument effects removed. CERES FM1-FM5 instruments measure filtered radiances in the shortwave (SW; wavelengths between 0.3 and 5 μm), total (TOT; wavelengths between 0.3 and 200 μm), and window (WN; wavelengths between 8 and 12 μm) regions. CERES FM6 on NOAA-20 also has SW and TOT channels but the WN channel was replaced with a longwave channel (LW; wavelengths between 5 and 35 μm). The spatial resolution of CERES footprints varies with satellite altitude because the telescopes for all CERES instruments are identical. On TRMM, the footprint size was 10 km (nadir equivalent circle diameter), while on Terra and Aqua it is 20 km. On SNPP and NOAA-20, the CERES footprint size is 24 km.

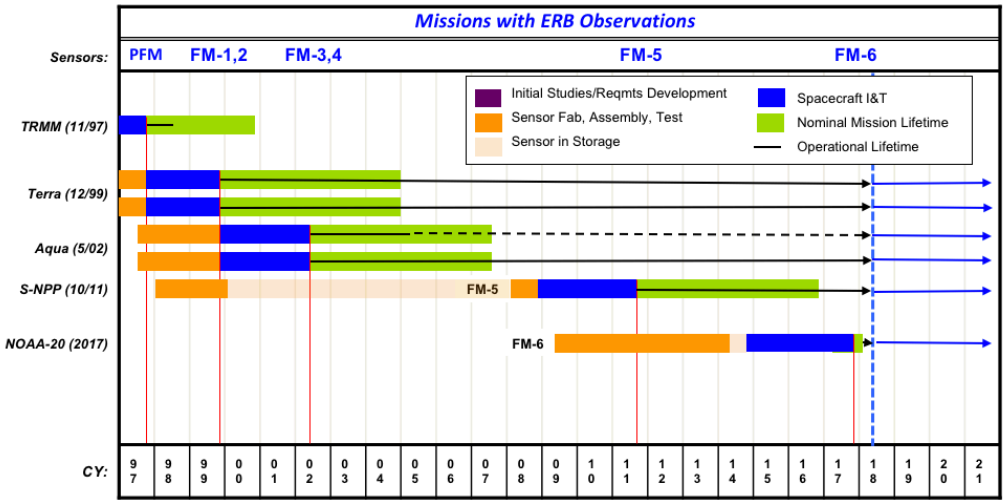

Figure 2.1 Timelines of each phase of development for CERES instruments on different satellites.

A unique feature of CERES is that it can be commanded from the ground to scan in different modes. In crosstrack mode, the scan is perpendicular to the ground track so that spatial sampling is optimized, providing global coverage daily. This is the primary mode used to produce CERES Level-3 gridded data products. The CERES rotating azimuth plane (RAP) scan mode relies on the instrument's azimuthal axis drive system to optimize angular sampling. When in RAP mode, the instrument scans in elevation as it rotates in azimuth, thereby acquiring radiances over a full hemispheric range of viewing zenith and relative azimuth angle combinations. CERES RAP data were used in order to construct CERES angular distribution models (ADMs) (Loeb et al., 2005;

Su et al., 2015a), which describe how TOA radiances normalized by flux vary with sun-Earth-satellite viewing geometry and scene type. A "scene type" is a specific Earth view with distinct characteristics and properties (e.g., clear ocean, desert, cloud, etc.). The ADMs are needed in order to convert measured radiances to radiative fluxes (see also Appendix B). CERES can also be placed in alongtrack mode in order to acquire measurements of a target from multiple viewing zenith angles. Finally, in the programmable azimuth plane (PAP) mode, the CERES angular sampling is commanded from the ground by uploading instructions to the instrument to acquire multiangle measurements for specific scientific experiments (e.g., field campaigns, intercalibration with other instruments, etc.). In addition, azimuth rotation enables the moon to come into view between the nadir side of the instrument and the limb of the Earth, enabling validation of in-orbit instrument stability performance (Daniels et al., 2015).

Prior to launch, the CERES instruments underwent extensive ground calibration at a radiometric calibration facility (RCF) located at Northrop Grumman Aerospace Systems (formerly TRW Space and Technology Group) in Redondo Beach, CA (Lee III et al., 1998). The primary in-flight calibration systems used to detect drifts in CERES sensor gains are the Internal Calibration Module (ICM) and the Mirror Attenuator Mosaic (MAM) (Lee et al., 1992; Priestley et al., 2000; Priestley et al., 2011). The ICM consists of two blackbody calibration sources for the TOT and WN sensors and a Shortwave Internal Calibration Source (SWICS) for the SW sensor. The blackbodies operate at temperatures of 295K, 305K and 315K, and are monitored by a platinum-resistance thermometer. The SWICS consists of an evacuated quartz tungsten lamp operating at three discrete current levels producing spectra equivalent to 2100 K, 1900 K and 1700 K brightness temperatures. The radiometers observe the ICM in every normal cross-track elevation scan. Monthly gains are determined from ICM calibrations performed weekly, and a 5-month running mean is used to reduce noise. The MAM is a solar diffuser plate used for calibrating the SW and TOT sensors. It consists of a baffle to block stray light and a nickel substrate with aluminum coated spherical divots that attenuate and redirect the solar radiation into the field of view of the sensors.

CERES data products provide a comprehensive set of observed parameters required in order to address climate research involving ERB (Wielicki et al., 1996; Loeb et al., 2016a). Radiative fluxes are determined at the TOA, surface and within the atmosphere for all-sky and clear-sky conditions together with the associated cloud, aerosol and meteorological properties. The data products are available over a range of time-space scales, from instantaneous footprint to global monthly mean. As an example, Figure 2.2 shows Earth's global mean energy budget derived from CERES data products. At the TOA, observations from CERES instruments and a total solar irradiance monitor (Kopp et al., 2005) are the primary data sources, subject to a constraint on EEI from in-situ observations (Loeb et al., 2009a; 2018a). Surface and within-atmosphere radiative fluxes are derived from imager-based cloud, surface and aerosol property retrievals, meteorological input from reanalysis, and microwave radiometer snow/ice maps (Kato et al., 2013; Rose et al., 2013; Rutan et al., 2015; Kratz et al., 2010).

Figure 2.3 shows the CERES data processing flow, providing further detail about the high level of data fusion involved in CERES data product generation. Data products (colored boxes) are either footprint scale (levels 1b and 2), instantaneous gridded (1°x1° latitude-longitude), or time-averaged gridded (level 3). The coincident imager measurements (MODIS or VIIRS) provide detailed physical and optical properties within the coarser CERES footprints. This enables

improved accuracy in converting CERES radiances to radiative fluxes (Su et al., 2015a,b) and reliable identification of cloud-free areas within CERES footprints (Minnis et al., 2011; Trepte et al., 2018). In addition to the imager flying alongside CERES, contiguous geostationary imager measurements covering latitudes equatorward of 60° are used to infer hourly cloud-radiation data between CERES observation times (Doelling et al., 2013). This produces the synoptic stream ("SYN Stream") of data products. An alternate treatment of the diurnal cycle is to interpolate radiative fluxes between observation times using empirical models of the diurnal cycle (single scanner footprint, or "SSF Stream", Earth Radiation Budget Experiment, or "ERBE-Like Stream"). Both the SYN1deg and SSF1deg approaches are used to produce the Energy Balanced and Filed (EBAF) products, which serve as the primary CERES ERB CDR (Loeb et al., 2018a; Kato et al., 2018).

Since the start of CERES, the RBSP has processed data from 7 CERES instruments, 1 VIRS, 2 MODIS, 2 VIIRS and 20 geostationary imagers, all integrated to obtain climate accuracy in radiative fluxes from the top to the bottom of the atmosphere. A total of 25 unique input data sources are used to produce 18 CERES data products. Over 90% of the CERES data product volume involves two or more instruments. Periodic reprocessing of the entire CERES record is performed to ensure that the data record reflects variations in the climate system as opposed to artifacts associated with algorithm and/or input data changes. Currently, the CERES data products are in their fourth edition. A more detailed description of the CERES instrument, algorithms and data products is provided in Appendix B.

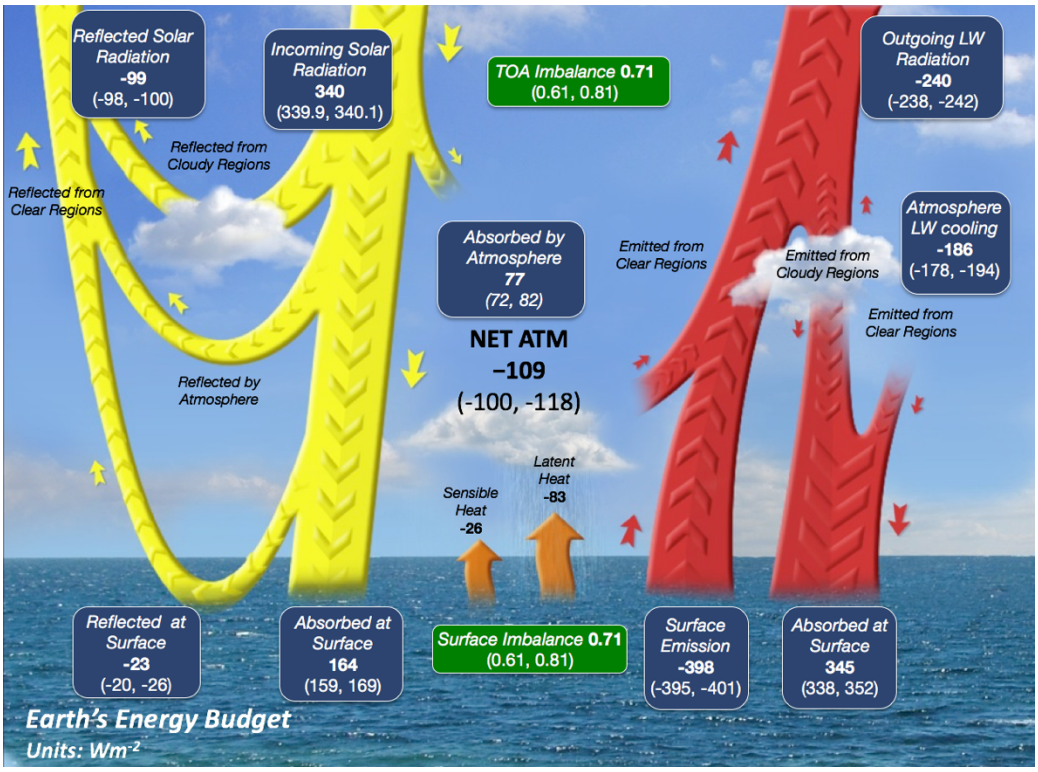

Figure 2.2 Earth's global mean energy budget for July 2005-June 2015. Radiative components (boxes) are determined from CERES data products. Latent and sensible heat are derived from Stephens and L'Ecuyer (2015). Uncertainties (1σ) are in parentheses beneath global mean values. (Updated from Loeb and Wielicki, 2016b).

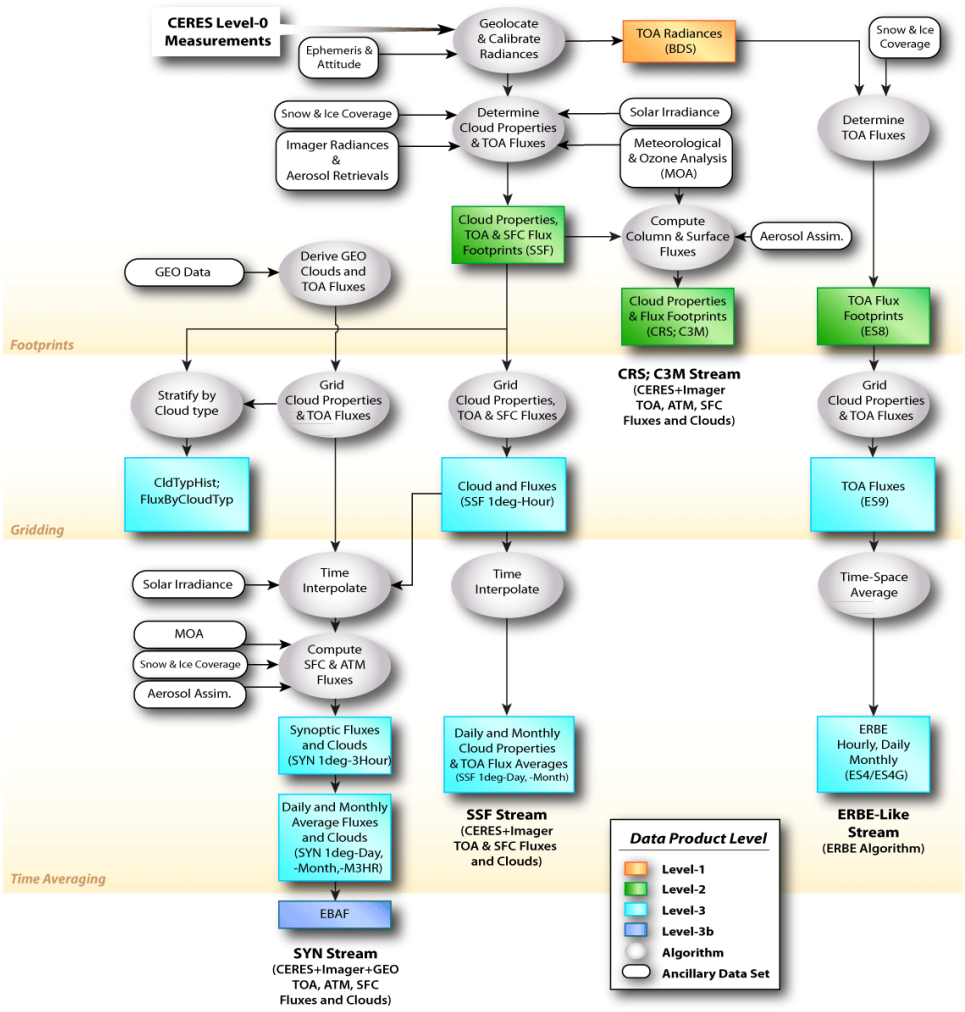

Figure 2.3 CERES data processing flow.

2.2 RBI

NASA was overseeing the build of the RBI, a broadband radiometer functionally similar to the CERES instruments, to enable the continuation of the CERES ERB CDR, intended for launch on the JPSS-2 platform in 2021. Responsibility for ERB measurements was transferred from NOAA to NASA in the 2014 President's Budget. A contract with Harris Corporation (formerly ITT Space Systems, a subsidiary of Excelis, Inc.) was initiated in 2014 for this purpose. It was intended to be an improved copy of the CERES FM6 instrument, with a 7 year rather than 5-year design lifetime. However, RBI ran into cost and schedule problems almost immediately. Cost to build, originally set at 179.4 million dollars, ballooned to over 300 million dollars by January 2018. NASA SMD therefore decided to cancel the build in January 2018.

2.3 EV-Continuity

Due to the importance of ERB measurements, its congressionally-mandated responsibility, and a commitment to continuing the long history of radiation budget measurements at NASA, the RBI cancellation decision memo included an action for the NASA

Earth Science Division (ESD) to develop a "detailed programmatic plan and associated schedule and budget" to replace the RBI mission with a lower cost alternative, exploiting a recommendation in the 2017 Earth science DS [NASEM, 2018] for ESD to initiate a new line of its "Earth Venture" program, to be known as Earth Venture-Continuity (EVC). The action to replace the RBI mission with an EVC alternative was also taken by NASA in recognition of the fact that RBI was considered in the 2017 DS to be part of the Earth Science "Program of Record," and that its implementation as planned was recommended in the DS (Recommendation 3.2). The DS envisioned that the program would solicit new and innovative ways to continue existing measurements, but at a reduced cost.

The "Earth Venture" program within NASA's ESD focuses on low-cost, cost-capped, competed Principal Investigator (PI)-led flight missions that provide an opportunity for innovative Earth science approaches. It was established in response to recommendations of the 2007 DS [NRC 2007]. There are currently three versions of the Earth Venture (EV) program: Earth Venture-Instrument (EVI), Earth Venture-Mission (EVM), and Earth Venture-Suborbital (EVS). EVI funds the construction of a flight instrument and its operation. Accommodation and launch costs are provided by NASA ESD. EVM funds small whole missions, including launch. Here, the PI has a choice of finding their own access to space or purchasing launch services from NASA. EVS funds suborbital missions. This component focuses on acquisition of measurements from airborne or balloon-borne platforms.

As recommended in the 2017 DS (Recommendation 3.2), the EVC program would consist of competed, cost-capped small missions–similar to the Earth Venture Mission program–to add a focus in NASA ESD's portfolio on continuity-driven observations and provide opportunity for sustained observations. The DS recommendation is based on the idea that some important scientific questions require long data sets to address them, and that in order to be sustainable over the long term, acquisition of these data sets cannot be so costly that they disrupt the ability to make new measurements.

NASA has created an EVC program with the first mission to focus on construction and flight of an affordable radiation budget instrument that can continue the current radiation budget data record. Since the ideal platform to host a follow-on radiation budget instrument is JPSS-3, due to launch in 2027, this instrument needs to be built no later than 2025, allowing time for integration. Given a nominal 5-year build, a date for selection of the instrument would be 2020. The current planned release date for the Announcement of Opportunity (AO) to solicit the instrument is December, 2018.

The intent of the NASA EVC program in general is to produce, launch, and operate instruments that will demonstrate an approach for the long-term continuation of important data sets such as those for ERB. However, doing so at a reduced cost presents a stiff challenge, as the cost of an instrument that would provide seamless continuity (i.e., a carbon copy of previous instruments) likely exceeds the EVC cost cap. NASA ESD is therefore looking to the ERB community to provide an innovative solution that maintains continuity to the best degree possible, without exceeding the mission cost cap. In addition to the required cost cap and capability to continue observations, the NASA EVC program will also use the following as evaluation criteria for submitted proposals: the cost of future copies of the proposed instrument, accommodability of the instrument on different platforms, instrument producibility, and ease of future technology infusion to improve the measurements.

As noted earlier, “continuity” does not mean simply acquiring some sort of measurement of a “continuity variable” without regard to the characteristics of the current measurement (e.g., spatial, temporal, and spectral resolution, precision, accuracy, and stability). Without a close match to those characteristics, the scientific utility of a combined dataset–typically set by the ability to detect long-term geophysical trends in the data–could be compromised. Characteristics of the continuity measurement must therefore be guided by the characteristics of the CERES CDR.

In order to be ingested into the CERES data processing flow shown in Figure 2.3, a new ERB instrument would need to provide results from pre-launch calibration activities, instrument flight software for instrument operations, spectral response function (SRF) and point-spread function (PSF) data, and an in-flight calibration protocol to identify and correct for instrument changes. This information would enable the creation of calibrated filtered and unfiltered radiance measurements and imager PSF-averaged properties that will ultimately be part of the new instrument’s instantaneous footprint-level data products. In Section 5, we return to a discussion about the specifics of how a new ERB instrument would feed into the existing processing system in order to extend the CERES CDR.

2.4 Constitution of ERB SWG

In order to accomplish the goals set forward in this document, a science working group was assembled. The working group was limited to civil servant participants, due to difficulty of complying with Federal Advisory Committee Act (FACA) rules and producing a report in time to meet the required schedule for launch on JPSS-3. A general invitation with an explanation was sent to a large mailing list of ERB scientists who could potentially participate. In addition, specific invitations to key personnel were also made. The working group was constituted from those who were willing and interested in participating, and therefore represents a “coalition of the willing.” Working group members were not barred by FACA rules from discussing and receiving input/advice from non-civil-servant participants. Any such discussions could inform the opinion of the participants in this working group and therefore be represented in this document, as guided by the discretion of the working group members. In order to dispel community conflict of interest concerns, the following actions were taken:

i. This report was published in draft form and to solicit comments from the broader community prior to finalization.
ii. Comments received informed the content of the report.
iii. The working group will be disbanded upon formal completion of this report, and will not participate in drafting the AO. It is expected that members will therefore be free to participate in responses to the AO without restriction.
iv. While this report recommends specific instrument and observational characteristics and refers to these characteristics in places as "requirements", there is no either explicit or implied constraint that report recommendations will be followed in drafting the AO. Thus the recommended instrument and measurement characteristics provided here, even when referred to in this document as "requirements," are not intended to be and should not be taken as formal instrument requirements for responses to the EVC AO.
v. The AO will be published in draft form prior to its official release, again allowing for comments/input from the broader community.

2.5 ERB Gap Risk Analysis

With five of the six CERES flight models operating beyond their design lifetimes, the risk of a temporal data gap occurring between the last remaining CERES instrument's end-of-mission and beginning of the EVC ERB mission is a real concern. While CERES instruments are precise enough to track changes in ERB, their absolute calibration accuracy is insufficient to ensure that measurements on successive platforms will be on the same absolute radiometric scale should a data gap occur. A period of overlap between the two missions is needed so they can be intercalibrated against each other. According to Loeb et al. (2009b), at least 6 months of overlapping global data or one year of tropical data is needed to tie together the records of instruments on successive platforms through intercalibration.

In order to assess the likelihood that a data gap will occur between the current fleet of CERES instruments and the planned EVC ERB mission, we perform a gap risk analysis. Figure 2.4a-b provides estimates of the probability that a data gap will occur given the ERB instrument flight schedule (Figure 2.1) and historical spacecraft and instrument survival rates (Castet et al., 2009). We assume the EVC ERB instrument flies on the JPSS-3 satellite and that a mission terminates if either the ERB instrument, imager it flies with, or spacecraft fails. A further assumption is that an ERB instrument can bridge a data gap and maintain radiometric continuity of the ERB CDR even if its orbit drifts in mean local time (MLT) past its nominal mission requirement. According to projections, the Terra and Aqua missions will de-orbit when fuel becomes too low for science data acquisition, which occurs in 2026 for Terra and 2025 for Aqua. For the other satellites, less is known about their end-of-mission plans. For comparison, two sets of assumptions are made. In Figure 2.4a, we assume SNPP, NOAA-20 and the EVC ERB instruments reach their end-of-life 3-years past their nominal prime missions of 5 years. In Figure 2.4b, we assume a more optimistic case in which SNPP, NOAA-20 and the EVC ERB each last 15 years. In the first case (Figure 2.4a), the probability of a data gap reaches 50% in 2026 regardless of whether or not the EVC ERB instrument launches. In subsequent years, the data gap probability reaches unity in 2028 if no further ERB instrument is launched and remains < 70% with an EVC ERB. In the more optimistic case shown in Figure 2.4b, the probability of a data gap reaches 25% in 2026 regardless of whether the EVC ERB flies and climbs to >50% the following year if it does not fly. With the EVC ERB, the data gap probability remains <40% through 2032, and <60% through 2034. Thus, according to this analysis, for the EVC instrument to significantly reduce the probability of a data gap in the ERB record, the Terra and Aqua instruments must last into the mid-2020s and the SNPP and JPSS-1 instruments must both remain operational three times longer than their nominal 5-year prime missions.

Should a data gap in the ERB record occur, a reasonable question to ask is whether or not it can be "bridged" using other data sources. We examine the feasibility of using less-accurate imager retrievals to compute radiative fluxes and tie the time series before and after a data gap together (see illustration Figure 2.5). We construct a time series of observed CERES Aqua SW, LW and Net TOA fluxes from the SSF1deg-month product between 2003 and 2016 and consider all possible 1-year gaps in different parts of the record (12 total). In each case, we regress computed and observed TOA fluxes prior to and after the gap and calculate adjustment factors that can be applied to the post-gap record in order to place it on the same scale as the pre-gap record. Here, the regressions consist of observed and computed zonal annual mean TOA fluxes between 20°S-20°N. The computed TOA fluxes are taken directly from the CERES SYN1deg-Month product,

which uses MODIS Terra, Aqua and geostationary cloud retrievals as input to the NASA Langley Fu-Liou radiative transfer model. We apply the adjustment factors for the 12 possible 1-year gaps in the record and compute the root-mean-square error (RMSE) between the post-gap flux estimate and the "true" value in CERES Aqua SSF1deg-month. Results, shown in Figure 2.6, indicate that the uncertainty in placing the pre- and post-gap records on the same radiometric scale is $\pm$0.32 Wm^{-2} for SW, $\pm$0.37 Wm^{-2} for LW, and $\pm$0.49 Wm^{-2} for net TOA flux at the 1σ level. We note that this analysis requires that imager remain healthy and stable across the gap. The longer the gap, the greater the risk. The uncertainty in global mean net TOA flux obtained in Figure 2.6 is too large to enable decade-to-decade changes in EEI to be resolved, as that is ~0.25 Wm^{-2} according to Allan et al. (2014), which is a factor of 2 smaller than the error in net TOA flux due to a data gap. An uncertainty of this magnitude would also add considerable uncertainty to linear trends in the data, both globally and regionally. Alternate methods that are less dependent upon model assumptions should thus need to be considered to further reduce the error should a gap in the ERB record occur.

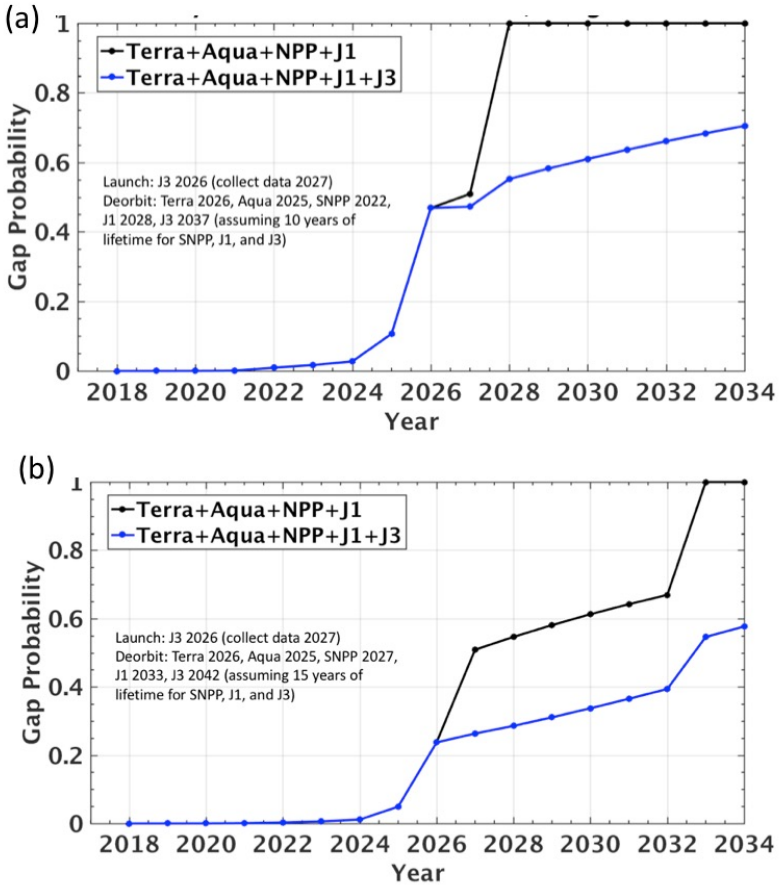

Figure 2.4 Probability of a data gap in the global satellite ERB time series from present through a given year for Terra and Aqua de-orbit dates in 2026 and 2025, respectively, and (a) SNPP de-orbit in 2022, NOAA-20 de-orbit in 2028, and JPSS-3 de-orbit in 2037, and (b) SNPP de-orbit in 2027, NOAA-20 de-orbit in 2033, and JPSS-3 de-orbit in 2042. The black curve includes all CERES instruments currently flying while the blue curve also includes the EVC ERB instrument on JPSS-3 satellite.

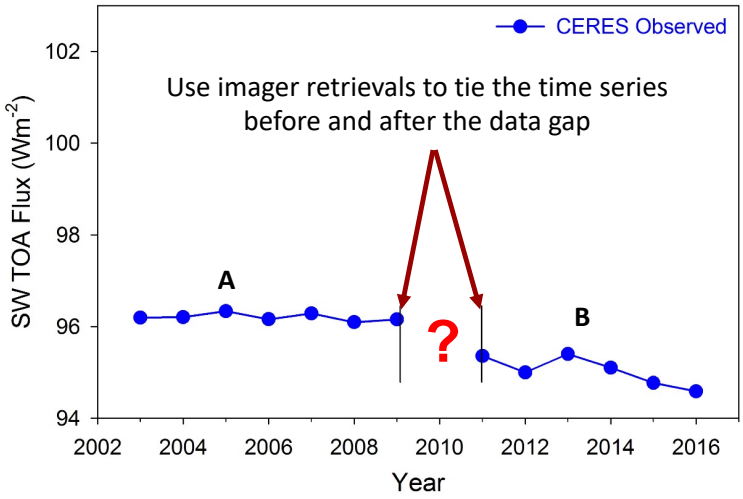

Figure 2.5 Illustration of a data gap between successive ERB instruments. Shown is the global annual mean SW TOA flux from ERB instrument A through 2009, followed by a data gap in 2010, and observations from ERB instrument B from 2011 onwards.

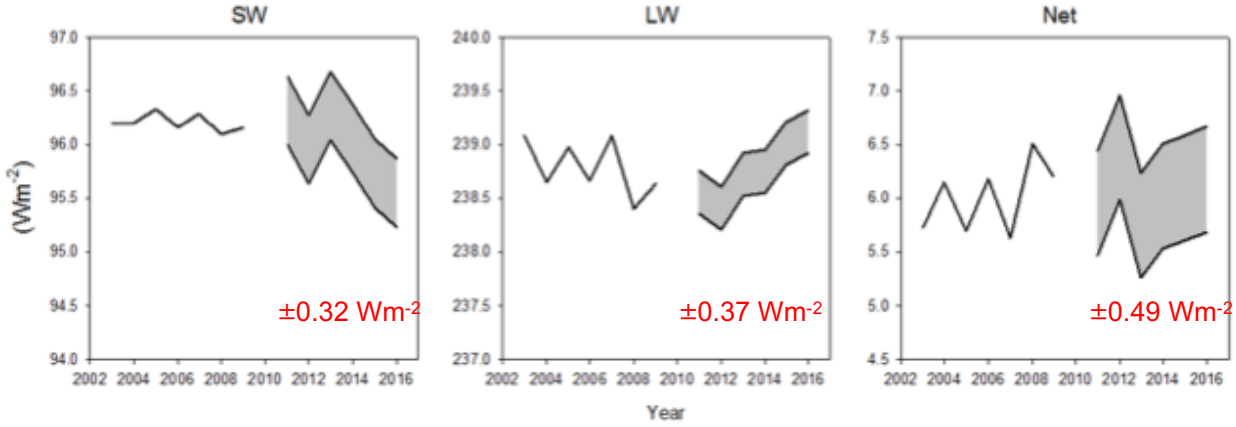

Figure 2.6 Reconstructed global annual mean TOA flux for a 1-year gap in 2010 showing the uncertainty (1σ) envelope (gray regions) that results when the data gap is "bridged" using imager-based computed TOA fluxes from CERES SYN1deg for SW, LW and Net TOA flux.

3. ERB Science Focus Areas

In the following, we provide an overview of the science that CERES data products support. Selected highlights from peer-reviewed journal publications are provided for each science focus area in Appendix C for reference. The science highlights are by no means complete. A more comprehensive list of papers is provided on the CERES website at the following address: (https://ceres.larc.nasa.gov/ceres_library_search.php).

3.1 Earth's Energy Budget

Climate is determined by the amount and distribution of incoming solar radiation absorbed by Earth. In response to energy imbalances, complex processes give rise to energy flows within the atmosphere, hydrosphere, lithosphere, cryosphere and biosphere occurring over a range of time-space scales. The coupled nature of the system is such that external perturbations to the Earth's energy budget impact all of the Earth subsystems to varying degrees. For an Earth system in equilibrium, these energy flows must produce outgoing LW radiation at the TOA that is equal to the incoming absorbed solar radiation. A positive TOA imbalance indicates that the planet is taking up heat, with 93% ending up as heat storage in the oceans and only 1% of the excess energy used to warm the atmosphere. The remainder is used to melt snow/ice and warm land (Trenberth, 2009; Church et al., 2011; Rhein, et a., 2013). The defining challenge for climate science is to understand and predict the timing and intensity of the changes to Earth's subsystems in response to anthropogenic forcing. Because EEI is a measure of heat uptake by the planet, there is a critical need to observe, track and understand EEI and the underlying processes that influence it (von Schuckmann et al., 2016).

The substantial internal variability of the climate system complicates matters, as it can temporarily mask or enhance the system's response to anthropogenic forcing. A good recent example of this is the so-called "hiatus" or slowdown in global mean surface warming over the first 15 years of the 21st century (Stocker et al., 2013; Yan et al., 2016). Despite the slowdown in surface warming, CERES satellite observations of changes in Earth's energy budget indicate that the Earth has been continually accumulating energy at a constant rate during the hiatus period (Figure 3.1). Recent studies have shown that the most likely cause of the slowdown in surface warming is a vertical redistribution of heat in the ocean associated with an intensification of the Pacific trade winds linked to a switch to a negative phase of the Interdecadal PDO in 1999 (England et al., 2014; Trenberth and Fasullo, 2013). More recently, sea-surface temperature (SST) pattern changes over the eastern Pacific associated with a shift to the positive phase of the PDO resulted in a marked decrease in low cloud amount, which reduced reflected SW radiation, and increased EEI (Loeb et al., 2018b). CERES captured the changes at monthly temporal and regional spatial scales, enabling process-level understanding of the variability, and providing unique data to test weather and climate models.

At longer timescales, a forcing leading to an increase (decrease) in global mean temperature must be accompanied by a decrease (increase) in EEI. However, when forced with Representative Concentration Pathways (RCP) greenhouse gas concentration trajectories, CMIP5 climate models project that EEI can either increase or decrease with surface temperature, depending upon the RCP scenario: for RCP8.5, representing elevated greenhouse gas emissions, there is a rapid increase in EEI, while it decreases for RCP2.6, the lowest emissions scenario. Outgoing LW radiation increases similarly in each RCP scenario with warming while reflected SW

radiation decreases far more rapidly for RCP8.5 due to marked decreases in cloud cover and snow/sea-ice (Collins et al., 2013). Long-term measurements of EEI, its SW and LW components and their regional distribution are thus critical to determine Earth's actual climate trajectory. Because EEI can be approximated as the difference between climate forcing and climate temperature response, one can think of EEI as a measure of the climate forcing the Earth has yet to respond to (Hansen et al., 2005). It is related to sea-level rise through the steric component (Church et al., 2013) because most of the excess energy is stored in the ocean.

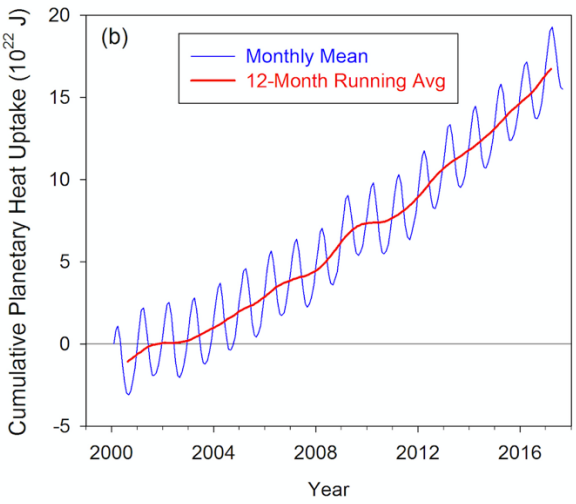

Figure 3.1 Cumulative planetary heat uptake from monthly CERES observations for March 2000-September 2017. A one-time adjustment to CERES SW and LW fluxes is made within observational uncertainty to ensure the global mean net TOA flux for July 2005-June 2015 is consistent with an in-situ based EEI value determined primarily from Argo ocean profiling floats (Johnson et al., 2016). (From Loeb et al., 2018b).

With daily global coverage, the CERES record is the only available observation-based data source that enables monthly variability in EEI together with its SW and LW TOA flux components at finer time-space scales. Because of its complete sampling of Earth, CERES compliments in-situ based determinations of EEI (e.g., Argo network), which provide highly accurate absolute values of EEI when calculating tendencies in ocean heat content anomalies from at least a decade of observations. At interannual and shorter timescales, in-situ EEI is more uncertain due primarily to sampling uncertainties, as illustrated in Figure 3.2 (see also Trenberth et al., 2016). In contrast, CERES can resolve monthly anomalies in EEI with great precision. This is shown in Figure 3.3, which compares monthly anomalies between the CERES EBAF product and CERES instruments on Terra, Aqua and SNPP. The standard deviation in monthly anomaly differences are < 0.12 Wm^{-2} for SW, < 0.16 Wm^{-2} for LW and < 0.17 Wm^{-2} for EEI (net TOA flux).

In addition to providing critical information about EEI, CERES data products improve our understanding of regional energy budgets, atmospheric and oceanic energy transports, surface and atmospheric energy balance, general circulation, and polar climate (see Appendix C.1).

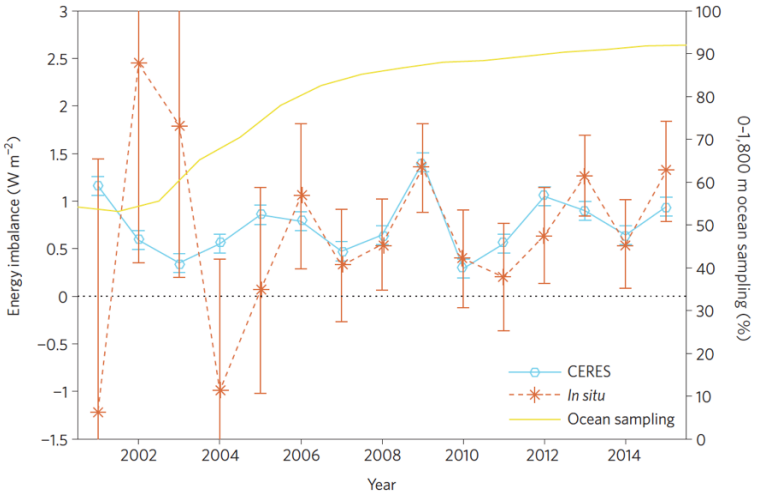

Figure 3.2 Comparison of year-to-year net TOA annual energy flux from the CERES EBAF Ed2.8 product with an in situ observational estimate of uptake of energy by Earth's climate system. The in situ estimate is composed of first differences of annual 0–1,800 m ocean heat content anomalies estimated from Argo float profiles and other sources. CERES data are adjusted to agree with the 2005 through 2015 in situ heat uptake rate of 0.71 ± 0.10 W m–2 (5–95% confidence intervals) (From Johnson et al., 2016).

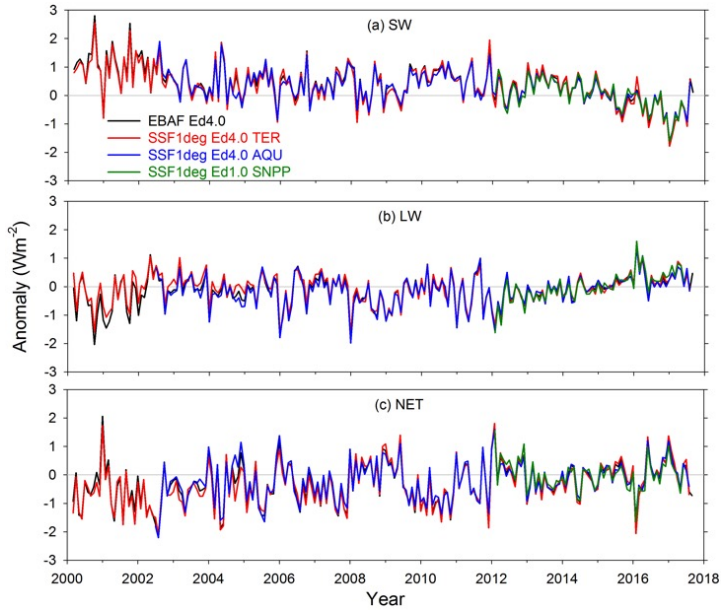

Figure 3.3 Deseasonalized monthly anomalies in global mean (a) SW, (b) LW and NET TOA radiation from EBAF Ed4.0, SSF1deg-Ed4.0 Terra (TER), Aqua (AQU) and Suomi-NPP (SNPP). Anomalies are calculated using a common climatology from February 2012-June 2017. (From Loeb et al., 2018b).

3.2 Cloud Processes and Feedback

The Earth's surface temperature is expected to rise between 1.5° and 4.5°C in response to a doubling of atmospheric CO_2 concentrations (IPCC, 2013). Despite much effort by the climate science community, the large range of uncertainty has not narrowed appreciably over the past 30 years. A key reason is due to the representation of climate feedbacks in climate models. Increased CO_2 in the atmosphere alters the Earth's energy balance by reducing how much

thermal infrared radiation is emitted to space. To restore a balance between absorbed solar radiation and outgoing LW radiation, the Earth system must emit more infrared radiation to space. In the absence of other changes, a CO_2 doubling would require Earth's temperature to eventually increase ~1.2 K (Colman, 2003). As Earth warms, other processes and properties of the climate system are altered, leading to further changes in Earth's energy balance and temperature. The key feedbacks in the climate system are associated with surface temperature, water vapor, clouds, snow and ice, and the vertical temperature structure of the atmosphere (Soden and Held, 2006). A climate feedback is quantified through its climate feedback parameter, given by the change in downward TOA flux for a given temperature change. Thus, an increase in downward net TOA flux with warming temperatures yields a positive climate feedback parameter.

Climate models agree that feedbacks collectively amplify the surface temperature response to external forcing, but the strength of the feedbacks varies greatly (Boucher et al., 2013). The main stabilizing (negative) feedback is the temperature response (Planck feedback), which is well represented in models. Water vapor provides the largest positive feedback, and vertical changes in water vapor and temperature are tightly coupled. Accordingly, the sum of the lapse rate and water vapor feedbacks are well represented by the majority of climate models. Feedbacks due to clouds and surface albedo (associated with snow and ice changes) are also positive in all models, but cloud feedbacks constitute the largest source of uncertainty in current predictions of climate sensitivity.

Given the large inter-model spread in climate sensitivity due to uncertainties in climate feedbacks, ERB observations play a key role in helping narrow the uncertainty. Historically, the cloud feedback community has tried to understand cloud feedback processes by: (i) examining cloud and radiation variability with changes in atmospheric patterns like shifts of the midlatitude jets or expansion of the Hadley cell (e.g. Li et a. 2014, Tselioudis et al 2016), and (ii) by quantifying the contribution of feedbacks to the global energy balance through examination of the interannual co-variability of clouds, radiative fluxes, and surface temperature (e.g. Dessler 2010, Zhou et al. 2015). In the first line of research, CERES retrievals have been used extensively along with flux estimates from datasets that utilize cloud and atmospheric properties to derive the radiative flux components, such as ISCCP-FD (Zhang et al. 2004) and SRB (Stackhouse et al. 2004). In the second line of research, CERES flux retrievals have been the primary data source. Owing to substantial internal variability of the climate system, a long data record that is free of calibration drifts is needed for cloud feedback science. This will enable long-term trends and small variations in ERB to be observed. A dedicated Earth radiation budget instrument that extends the existing CERES record satisfies this requirement. From estimates of radiative forcing, observations of the covariability between surface temperature and TOA radiation can be used to infer empirical estimates of climate feedback (Forster, 2016; Dessler, 2010; Zhou et al., 2015; Dessler et al., 2018). TOA net downward radiative flux is equated with the difference between TOA radiative forcing and the surface temperature change multiplied by the climate feedback parameter. Since the Earth is not in radiative equilibrium, the climate feedback derived under transient warming is often referred to as effective global climate feedback in order to distinguish it from equilibrium global climate feedback (Armour et al., 2013). Recent studies have used ERB data to show that with the exception of the Planck feedback, feedbacks from water vapor, clouds, snow and ice,

and the vertical temperature structure of the atmosphere are collectively positive and therefore amplify warming (Dessler, 2010; Zhou et al., 2015; Dessler et al., 2018).

Zhou et al. (2015) show that global mean cloud feedbacks derived from year-to-year (or interannual) variations in 27 CMIP5 models are correlated with their corresponding global mean long-term cloud feedback. They find that low cloud cover change in response to surface warming explains most of the covariance between interannual and long-term cloud feedback. The average interannual cloud feedback is about twice as large as the long-term cloud feedback due primarily to differences in interannual and long-term SST warming patterns. Assuming the relationship between interannual and long-term cloud feedback from the climate models holds true in nature, the observed interannual cloud feedback from CERES can then provide a direct constraint on model-predicted long-term cloud feedback (Figure 3.4a). In their study, only 10 years of CERES data were used. In that case, the interannual cloud feedback of most models is within the ±2σ uncertainty interval of CERES. The large uncertainty range in the CERES-derived cloud feedback is due to large internal variability of the climate system. With a longer observational record, the observational uncertainty decreases significantly providing a tighter constraint on model cloud feedback. This is illustrated in Figure 3.4b, which shows the relationship between the 2σ uncertainty of interannual cloud feedback and the number of years used to calculate the interannual cloud feedback.

Chung et al. (2012) also addressed the question of how long an observational record is needed to constrain climate feedback. Using coupled atmosphere-ocean model simulations, they computed climate feedbacks from differences between climate states as a function of the averaging length used to define the climate states and the time separation between the climate states. In order to reduce the upper bound of uncertainty in climate sensitivity by a factor of 2 (equivalent to a 2σ uncertainty in climate feedback of 0.26 W m^{-2} K^{-1}), an averaging length of at least 10 years would be required to define the climate states and the climate states would need to be separated by 40 years, thus requiring an observational record of at least 50 years. The main driver for such a long record is the cloud feedback contribution, which exhibits considerably more variability than other feedback contributions (e.g., lapse rate, water vapor, and surface albedo). Importantly, the Chung et al. (2012) analysis does not factor in observational uncertainties, which would further increase the length of the record needed.

It is worth noting that both clear-sky and all-sky ERB observations are needed to constrain cloud feedback. The observed cloud feedback is inferred from the change in cloud radiative effect, defined as the all-sky minus clear-sky net downward radiative flux at the TOA. This requires an ERB instrument with a relatively NFOV (see Section 5). A NFOV is also important in order to observe the regional distribution of cloud feedback and to improve our understanding of how clouds influence ERB on a process level. Different cloud types respond to warming in distinct ways and these changes can alter the local environment and circulation patterns through various pathways.

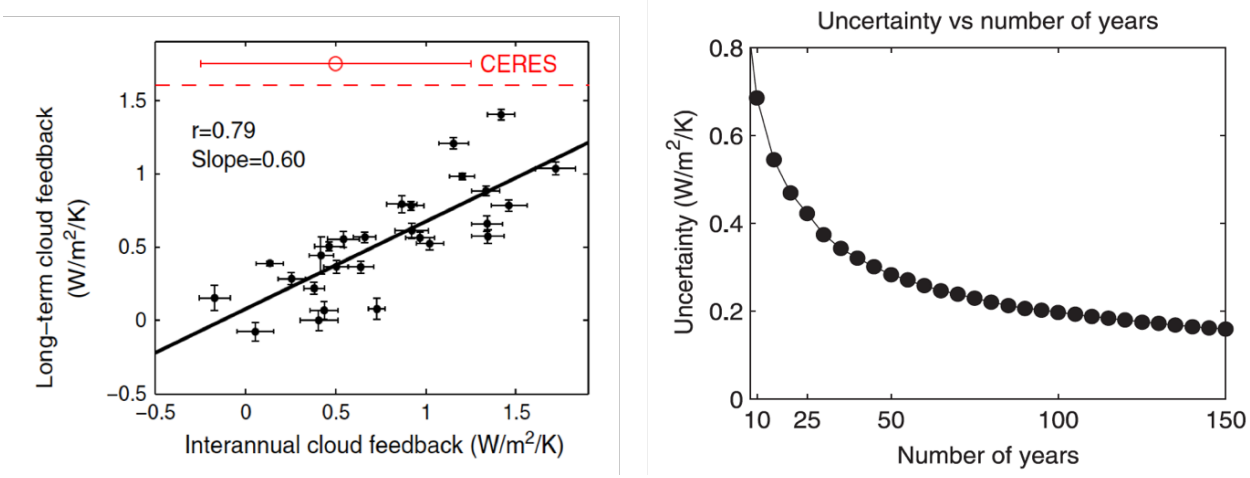

Figure 3.4 (a) Global mean interannual cloud feedbacks in 27 CMIP5 models plotted against their corresponding global mean long-term cloud feedback. The red circles denote observed interannual cloud feedback estimated using CERES TOA fluxes over the period 2000–2010. (b) Relationship between the 2σ uncertainty of interannual cloud feedback and the number of years used to calculate the interannual cloud feedback. (From Zhou et al., 2015).

3.3 Aerosol Radiative Forcing

Aerosols influence ERB at the TOA, surface and within the atmosphere by scattering and absorbing solar and infrared radiation (aerosol direct radiative effect, or ADRE) and by altering cloud microphysics by acting as cloud condensation or ice nuclei, thereby modifying the optical properties and lifetime of clouds (aerosol indirect radiative effect, or AIRE). The total effect of aerosols is comprised of both natural and anthropogenic components. The anthropogenic component is referred to as a forcing of the climate system. Since aerosol forcing is negative, it offsets the radiative forcing of climate by well-mixed greenhouse gases. However, uncertainty in aerosol radiative forcing is large. Its magnitude ranges from -0.1 to -1.9 Wm^{-2} (at 90% confidence) in climate models, making it the largest source of uncertainty in radiative forcing of the climate system. Furthermore, state-of-the-art climate models that match the historical temperature record exhibit a negative correlation between aerosol radiative forcing and climate sensitivity (Forster et al., 2013). Therefore, in order to reduce the uncertainty in climate sensitivity, it is necessary to reduce uncertainties in both aerosol forcing and cloud feedback.

Early in the CERES project, Satheesh and Ramanathan (2000) demonstrated the usefulness of CERES observations for determining aerosol radiative forcing in polluted regions. In their approach, CERES instantaneous TOA fluxes are regressed against surface-measured aerosol optical depths for clear scenes as determined from the surface. Their approach was later generalized to global clear-sky ocean scenes by combining CERES TOA fluxes and coincident imager-derived AODs (Loeb and Kato, 2002; Loeb and Manalo-Smith, 2005; Zhang et al., 2005; Christopher et al., 2006; Zhao et al., 2008). The advantage is that the outgoing SW flux with aerosols at TOA is directly obtained from CERES measurements, eliminating the need to use models to estimate the aerosol properties to infer ADRE. The CERES data have also been used to determine aerosol radiative effects over land (Patadia et al., 2008 a,b; Sena et al., 2013, 2015; Feng and Christopher, 2013; Sundström et al., 2015). Recently, Paulot et al. (2018) use the CERES EBAF TOA and surface products to determine TOA clear-sky SW ADRE over ocean and land between 2001-2015 and compare trends over this period with those based on the GFDL

chemistry climate model AM3, driven by CMIP6 historical emissions (Figure 3.5). Both CERES and AM3 show increases in ADRE (reduced aerosol reflection) over the US and Europe and decreases over India (increased aerosol reflection). However, over China and the Western Pacific, AM3 simulates a large decrease in ADRE, which is inconsistent with the CERES results. Paulot et al. (2018) argue that this bias is partly due to the decline of SO_2 emissions after 2007, which is not captured by the CMIP6 emissions.

The CERES instantaneous footprint data combined with MODIS imager measurements have also enabled studies of aerosol-cloud interactions. The CERES SSF product provides radiative fluxes, aerosol and cloud properties and meteorological parameters for each individual CERES footprint, making this an ideal dataset for such studies (Loeb and Schuster, 2008; Quaas et al., 2008; Jones et al., 2009; Su et al., 2010; Sundström et al., 2015; Engström et al., 2015; Gryspeerdt et al., 2016). Others have supplemented CERES and MODIS data in the Aqua SSF with other A-Train data sets from CALIPSO, CloudSat, AMSR-E, enabling a truly synergistic approach to improving our understanding of the complex interactions among aerosols, clouds, precipitation and meteorology (Lebsock et al., 2008; Yorks et al., 2009; Painemal et al., 2014; Chen et al., 2014; Christensen et al., 2016).

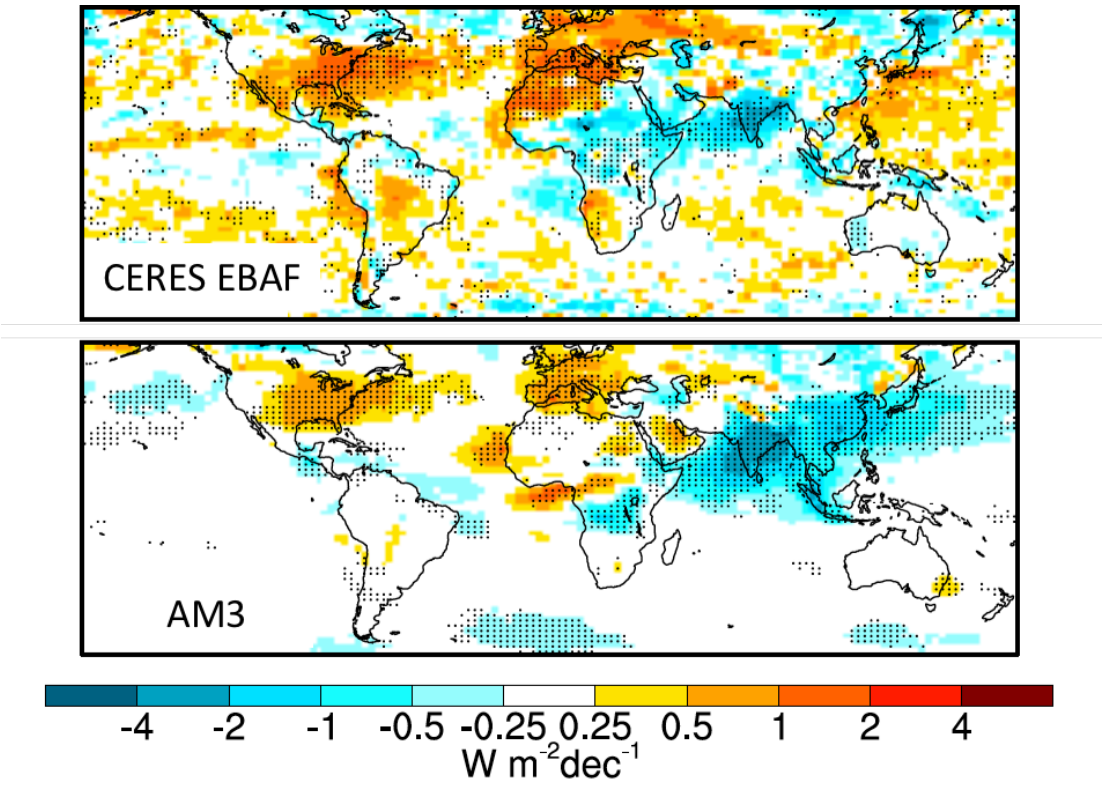

Figure 3.5 Decadal rate of change in the clear-sky SW ADRE from CERES EBAF (top) and the GFDL AM3 model (bottom). A positive (negative) trend indicates a decrease (increase) in the amount of radiation scattered to space by aerosols. (From Paulot et al., 2018).

4. Extending the CERES ERB CDR with a New EVC ERB Instrument

To address the ERB science focus areas, the strategy is to produce long-term CDRs of TOA and SFC ERB together with the associated atmospheric and surface properties that seamlessly continues CDRs from the RBSP. This requires observing reflected solar radiation (RSR) and outgoing LW radiation (OLR) for both all-sky and clear-sky conditions that can be incorporated into the existing CERES data processing system. In CERES processing, calibrated filtered radiances (Priestley et al., 2011) are converted to unfiltered SW, LW, and WN radiances (Loeb et al., 2001), which in turn are converted to instantaneous TOA radiative fluxes using empirical ADMs that have been developed using the CERES instrument's ability to acquire measurements by rotating in azimuth as it scans in elevation (Loeb et al., 2005, Su et al., 2015a). The CERES instruments provide global coverage daily, and monthly mean regional fluxes are based upon daily samples over the entire globe (Doelling et al., 2013). The standard CERES data products (Table 4-1) are produced using data from the CERES instrument together with coincident imager data from the Moderate Resolution Imaging Spectrometer (MODIS) and the Visible Infrared Imaging Radiometer Suite (VIIRS). To provide a diurnally complete representation of ERB, five contiguous geostationary imagers between 60°S and 60°N are also used. This accounts for cloud-radiation changes between CERES observation times. In addition, several other ancillary data products are required to characterize the meteorological state, ozone, aerosol, and snow/ice coverage.

Measurements from the ERB instrument are thus one of many inputs to a processing stream (Figure 2.3) that accounts for changes in radiation budget over a range of time/space scales at climate accuracy. Because the ERB instrument provides the only truly broadband observations, it plays a central role in and ultimately determines the accuracy and stability of the ERB CDR. In essence, the ERB instrument serves as the anchor used to adjust or normalize many of the ancillary inputs. For example, the geostationary imager data provide diurnal information hourly between ERB instrument observations, but they are based upon narrowband radiances and are less accurate than CERES or even MODIS and VIIRS. In order to benefit from the increased temporal sampling that geostationary data provides, while at the same time ensuring the CDR maintains the accuracy and stability of the ERB instrument, the geostationary imager data are normalized monthly to ensure consistency with the ERB TOA fluxes (Doelling et al., 2013). The quality of the ERB CDR therefore depends critically on the quality of the ERB instrument. A less capable ERB instrument or one that deviates significantly from the CERES instrument in terms of accuracy, stability and space-time sampling capability will likely fail to achieve the required continuity that is being sought in the EVC program.

In the following sections, we focus specifically on how a new ERB instrument would feed into the existing processing system in order to extend the ERB CDR beyond CERES. For clarity, we use information specific to a CERES-type instruments in order to illustrate the kind of information required. We recognize that the actual details will vary from one instrument to another and may also require some changes to the ground processing system. Therefore, to facilitate maximum reuse of the existing processing system, we encourage a strategy that produces a level 1B data file of geolocated and calibrated radiances organized and structured similarly to the CERES Level 1B file. This approach would focus software development efforts on the Level 1 software while requiring only minor software changes to the existing CERES Level 2 software elements to enable them to interface with the new Level 1 file. The focus for the remainder of this section is on pre-launch activities, instrument operations and the Levels 0, 1B and 2 stages of the CERES processing

system. We refer readers to the CERES Subsystem 1.0 Algorithm Theoretical Basis Document (ATBD) (Lee et al., 1997) and the CERES BiDirectional Scans (BDS) Collection Document (Cooper et al., 2013) for a detailed discussion of these topics.

Table 4-1 Processing descriptions for CERES level 1–3 data products.

Level	Description	Data Product
0	Raw digitized instrument data for all engineering and science data streams with all communication artifacts (e.g. synchronization frames, communication headers, duplicate data) removed. Level 0 data maintains Consultative Committee for Space Data Systems (CCSDS) packet format.	-
1B	Instantaneous filtered broadband calibrated radiances at the CERES footprint resolution and organized in scan order. Includes geolocation and viewing geometry, solar geometry, satellite position and velocity, and all raw engineering and instrument status data.	Bidirectional Scans (BDS)
2	Instantaneous geophysical variables at the CERES footprint resolution. Includes some level-1B parameters and retrieved or computed geophysical variables (e.g., filtered and unfiltered radiances, viewing geometry, radiative fluxes, imager radiances, and cloud and aerosol properties).	SSF
3	Radiative fluxes and cloud properties spatially averaged onto a uniform grid. Includes either instantaneous averages sorted by hour in UTC or temporally interpolated averages at 1-hourly, 3-hourly, daily, monthly, or monthly hourly intervals.	SSF1deg-hour, SSF1deg-day, SSF1deg-month, SYN1deg-1hour, SYN1deg-3hour, SYN1deg-day, SYN1deg-month, or SYN1deg-mhour
3B	Monthly and climatological averages of TOA and surface all-sky and clear-sky (spatially complete) fluxes, cloud radiative effect (CRE) and clouds properties. A one-time adjustment is applied to all-sky fluxes to ensure consistency between global mean net TOA flux and an in-situ based determination of EEI for a 10-year period (July 2005-June 2015). Surface fluxes are derived with a constraint by TOA fluxes.	EBAF-TOA, EBAF-SFC

a. Pre-Launch Calibration Activities

The goal of the ground calibration activities is to characterize and calibrate the instrument spectrally (SRF), spatially (PSF), temporally, and radiometrically (gain), traceable to the current NIST standards. This allows for cross comparisons (validation) with other Earth science data sets. With a rigorous calibration campaign, it is important to ensure that the future ERB instrument's performance enables all science objectives to be met. The future ERB instrument should include on-board calibration sources for all channels, allowing an independent check on their calibration across their spectral ranges. The purpose for the ground calibration is to determine the absolute calibration for the broadband sensors and to tie the on-board calibration sources to the ground NIST traceable references. Furthermore, the pre-launch activities also verify the instrument's design, its functionality and performance, the short-term variability and drift, and linearity.

The instrument characteristics required to convert the instrument detector output signals to radiances are the instrument gain coefficients, the SRFs, also known as the sensitivity (S) of

each of the CERES sensors, and the PSF, which describes the spatial responsivity of the instrument, accounting for the scanning motion, detector time constant and optical prescription.

b. Instrument Operations for Cal/Val

In order to satisfy the science objectives, a variety of operations should be performed to verify sensor response changes with respect to on-board calibration sources for the future ERB instrument. On-orbit calibration should include solar and lunar measurements to demonstrate accuracy and stability, and cross calibrate and validate the on-board sources. In order to maintain continuity with the current CDR, the future ERB instrument should enable intercalibration between 1) existing on-orbit CERES instruments on multiple spacecraft to tie the instruments to the same radiometric scale and 2) other Earth observing instruments to validate the science data products. Daily spacecraft and instrument activity reports should be included in the information provided to facilitate calibration activities.

c. Level 0: Raw Digitized Instrument Data

To seamlessly ingest into the existing CERES data processing system (Figure 2.3), the future ERB instrument should provide the sensor measurements from all channels, the gimbal measurements, and all engineering parameters sufficient to ensure the health and safety monitoring of the instrument. Ancillary spacecraft attitude and ephemeris data are also required to geolocate measurements in Level 1B processing. The CERES data processing system leverages EOS and JPSS ground system networks and the EOS Data and Operations System (EDOS) to retrieve instrument output and aggregate into Level 0 data. Once produced, Level 0 data transits a common data pipe between the EDOS system and the Atmospheric Science Data Center at NASA Langley where the data is archived and ingested into the remainder of the CERES data processing system to facilitate production of higher level data products.

d. Level 1b: Instantaneous Filtered Broadband Radiances

The CERES Level 1B product is called the BiDirectional Scan (BDS) and consists of geolocated and calibrated radiances organized by instrument scan. The Level 1B software applies instrument conversion equations and gain coefficients derived during pre-flight instrument characterization to convert digital detector counts to calibrated radiance values. The Level 1B software also coverts digitized engineering parameters to corresponding engineering units (e.g. temperature, current, voltage) and converts raw gimbal counts to gimbal elevation and azimuth positions to specify geolocation and viewing geometry and the TOA and surface. The BDS product includes each of these values in raw count and converted form.

e. Level 2: Instantaneous Unfiltered Radiances and Radiative Fluxes

The primary CERES Leve 2 data product is the Single Scanner Footprint (SSF). The SSF contains imager-derived cloud properties and aerosols from coincident MODIS or VIIRS radiances, CERES observed TOA fluxes and surface flux values. The Level 2 SSF software first derives scene information and cloud properties from imager radiances. Next, CERES ground derived and flight verified SRFs and level 1B CERES filtered radiances are used to calculate spectrally unfiltered broadband radiances. Scene ID and CERES ADMs are then used to produce CERES instantaneous observed TOA fluxes. Parameterized surface fluxes (not observed) are also produced. To ensure CERES measurements and Imager-derived properties are properly matched

spatially, each imager pixel is weighted by the CERES instrument's PSF prior averaging over the footprint.

5. Observational Characteristics: Recommendations by the ERB SWG

Arguably the most important characteristic for an ERB CDR is to enable observation of changes in ERB for a wide range of time and space scales. This requires as long an ERB time series as possible that will extend the best ERB time series currently available. The latter comes from the CERES instrument which provides data products for time scales ranging from hourly to decadal and spatial scales ranging from ~20 km (footprint) to global, enabling a range of scientific investigations. Since ERB time series continuity is the primary driver for a future ERB EVC mission, the ERB SWG recommends that the EVC ERB observational characteristics be comparable to those of CERES. Given this, the EVC ERB instrument characteristics are also similar to those for the CERES instrument. An ERB mission with different science objectives that do not include ERB continuity as a focal point, would quite possibly require an instrument with different characteristics, but such a mission and instrument does not pertain this report. In the following, we only discuss the ERB SWG recommendations for an instrument appropriate for an EVC ERB mission, and its accompanying imager. These are essential for satisfying the continuity requirement. The recommendations are based upon the CERES instrument capabilities (Threshold characteristics), the NCDC workshop report (Bates and Zhao, 2011) characteristics (Objective characteristics), and the recommendations in the 2017 DS.

5.1 ERB Instrument

5.1.1 Spectral Range

To be backward compatible with CERES, the new ERB radiometer should measure SW reflected solar radiation in the 0.3 to 5 μm wavelength range, outgoing LW outgoing radiation with wavelengths between 5 and over 35 μm (LW), and total outgoing radiation between 0.3 and over 100 μm (TOT). CERES instruments FM1-FM5 include SW, TOT and window (8-12 μm) (WN) channels, while CERES FM6, currently flying on NOAA-20, includes SW, LW and TOT channels. In each CERES instrument, three independent and identical coaligned and co-registered telescopes are used with filters sitting between the aperture and detector in the SW, LW and WN channels.

For all CERES instruments the LW measurement is obtainable by differencing the TOT and SW channels. Because FM6 has a LW channel, it is possible to also derive a LW measurement directly. This provides risk reduction not available on FM1 – FM5, and was the primary reason why the WN channel was replaced with a LW channel on FM6. With a TOT, SW and LW channel combination, failure of one will not mean loss of the science return as a differencing approach would still be possible to produce SW and LW radiances. With only two channels available, loss of either channel would result in a significant science loss. In addition, having these three channels enables 3-channel consistency tests to verify instrument calibration across a range of Earth scene types. While the loss of the WN channel is unfortunate, the record length (currently 18 years) will likely reach beyond 25 years, thereby providing sufficient science data for most research studies.

The ERB SWG considered the value of incorporating additional channels on the new ERB instrument. While interesting scientifically, this could increase cost. As a result, it was concluded that a better characterization of the SW and LW measurements (e.g., calibration) is preferable in the context of an ERB continuity instrument than additional spectral channels.

Table 5-1 EVC ERB instrument and mission characteristics. Threshold characteristics are consistent with CERES. Objective characteristics are consistent with Bates and Zhao (2011).

Category	Threshold	Objective	Note
Spectral Range	0.3 to 5 μm (SW)	0.3 to 5 μm (SW)	Three channels to buy down risk for redundancy and validation.
	5 to >35 μm (LW)	5 to >50 μm (LW)	
	0.3 to >100 μm (TOT)	0.2 to >100 μm (TOT)	
Field-of-View (IFOV)	~25km equivalent diameter @ nadir	~25km equivalent diameter @ nadir	FOVs for different channels must be co-registered.
Geographic Coverage	Near-Global	Near-Global	
Angular Sampling	Fixed Azimuth*	Rotating Azimuth; Programmable	*Requires reuse of existing CERES ADMs
Radiometric Accuracy	1.0% (SW), k=1	1.0% (SW), k=2	5-year requirement
	0.5% (LW), k=1	0.5% (LW), k=2	
	0.5% (TOT), k=1	0.5% (TOT), k=2	
Radiometric Stability	0.3%/decade, k=1	0.3%/decade, k=2	Allocated from accuracy requirement; All wavelength ranges
Radiometric Precision	<0.2 Wm^{-2} sr^{-1} + 0.1% of measured (SW)	<0.2 Wm^{-2} sr^{-1} + 0.1% of measured (SW)	
	<0.45 Wm^{-2} sr^{-1} + 0.1% of measured (LW)	<0.45 Wm^{-2} sr^{-1} + 0.1% of measured (LW)	
	<0.3 Wm^{-2} sr^{-1} + 0.1% of measured (TOT)	<0.3 Wm^{-2} sr^{-1} + 0.1% of measured (TOT)	
Linearity	0.3% from linear over dynamic range, k=2	0.3% from linear over dynamic range, k=2	
Onboard Calibration	SW Internal Cal Source LW Blackbody Source	SW Internal Cal Source LW Blackbody Source	Across all wavelength ranges
Vicarious Calibration	Enable periodic solar & lunar calibration	Enable periodic solar & lunar calibration	
Mission Class	C	C	
Lifetime	5 yrs	5 yrs	
Orbit	Sunsync. 1:30 pm ascending orbit	Sunsync. 1:30 pm ascending orbit	Consistent with CERES FM3-FM6
Overlap	6 months	1 yr	
Scene Identification	VIIRS-Class Imager	VIIRS-Class Imager	On same platform or within 3 min of and in the same viewing geometry

5.1.2 Field-of-View

The need to acquire clear-sky sampling and 1°x1° latitude-longitude regional all-sky TOA fluxes requires that the ERB instrument be NFOV as opposed to a WFOV. Clear-sky fluxes are needed to provide observations of cloud radiative effect (CRE), defined as the clear-sky minus all-sky SW and LW fluxes. The CRE observations are used to provide observational constraints on cloud feedback. This directly addresses DS Recommendation C-2a: “Reduce uncertainty in low and high cloud feedback by a factor of 2”, which is designated as a “most important” question. In addition, clear-sky footprints are necessary in order to enable the ERB instrument to be used for reducing uncertainties in aerosol radiative forcing, another major scientific objective in the 2017 Decadal Survey. Note that the 20-25 km footprint recommendation is an upper bound. In some respects, 20-25 km is actually coarser than desirable because it under-samples cloud free regions, but it is consistent with CERES. The CERES footprint was chosen after trade studies in the

1990's determined that this was an optimal value given detector response times and the need for daily global geographic coverage, which established the required scan rate given the orbital speed of the spacecraft. It is also worth noting that a smaller footprint is unlikely to affect the ability to create a continuous ERB data set from the EVC instrument in combination with CERES.

It is critical that the fields of view of the NFOV instrument channels be co-registered. That is, that they simultaneously measure the same ground location. This is required in order to determine SW and LW radiative fluxes by differencing a combination of TOT and SW or TOT and LW.

5.1.3 Geographic Coverage

In order to continue the CERES data products at a comparable accuracy to what is currently provided, the new ERB instrument should provide near-global coverage daily. To better understand the impact of reduced geographical coverage, we compare TOA fluxes for CERES sampling with those for viewing zenith angles (VZA) $< 45°$, where VZA is defined at the surface. Although the CERES algorithms can determine TOA fluxes for VZA $\leq 70°$, the imager (e.g., MODIS) is restricted to a maximum VZA of $\approx 65°$, so we assume 65° as representative of the VZA limit for the current CERES data products. Figure 5.1a-d compare daily (24-h) mean SW and LW TOA fluxes for VZA $< 45°$ and VZA $< 65°$ for January 4, 2008. In the SW, the geographic coverage is significantly reduced everywhere except poleward of 60°S for VZA $< 45°$ (Figure 5.1a), while only a small area at the swath edges is missing for VZA $< 65°$ (Figure 5.1b). Since LW includes both daytime and nighttime overpasses, geographic coverage improves in both cases (Figure 5.1c-d). However, biases of ± 20 Wm^{-2} in the 24-h mean LW TOA flux occur for VZA $< 45°$ in regions sampled only during daytime or nighttime satellite overpasses (Figure 5.2).

Figure 5.3a-d show the error in monthly mean TOA flux for January and July 2008. In the SW, errors reach 20 Wm^{-2} over the South Pacific Convergence Zone and Southern Ocean. Errors are also appreciable for both SW and LW over central Africa in January. In these locations, day-to-day variability in TOA flux is pronounced, resulting in a greater sensitivity to reduced geographical coverage. The global monthly RMSE is ≈ 6 Wm^{-2} for SW and ≈ 3 Wm^{-2} for LW. This causes the overall regional monthly mean TOA flux uncertainty to more than double in the SW and increase by 67% in the LW.

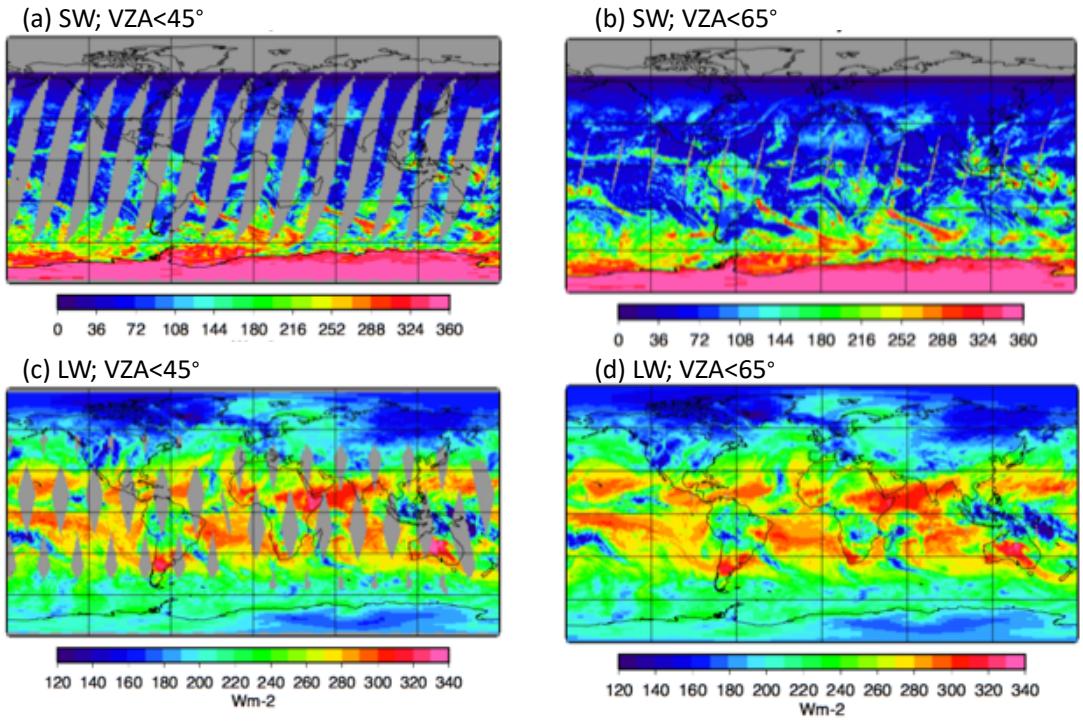

Figure 5.1 All-sky SW (top) and LW (bottom) TOA flux for January 4, 2008 for (a, c) VZA< 45° and (b, d) VZA< 65°.

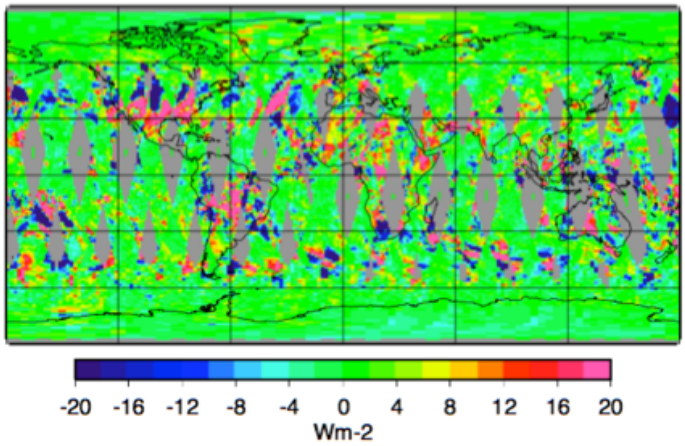

Figure 5.2 All-sky LW TOA flux difference for January 4, 2008 (LW(VZA<45°) minus LW(VZA< 65°)).

The error in regional TOA flux monthly variability for VZA $< 45°$ is 50% for SW and 30% for LW. Variability is determined from the standard deviation of deseasonalized monthly anomalies over 17.5 years (March 2000-September 2017). Globally, the corresponding error for both SW and LW monthly variability is ≈18%. In these comparisons, the 45° VZA cut-off is applied over the entire record. If we instead retain full VZA coverage for part of the record and apply the 45° VZA cut-off for the remainder, the above errors increase. This is because there is a VZA dependence in CERES TOA flux that is not entirely removed by the CERES ADMs (Su et al., 2015b).

Regional trend differences due to a 45° VZA cut-off are roughly 0.8 Wm^{-2} per decade for both SW and LW (for 17 years of Januaries). In addition, regional trend differences are quite noisy, with the satellite tracks apparent in the regional difference plots. Global trend differences due to

45° VZA cut-off are generally quite small, remaining < 0.055 Wm^{-2} per decade for SW and < 0.03 Wm^{-2} per decade for LW, at the 95% confidence level.

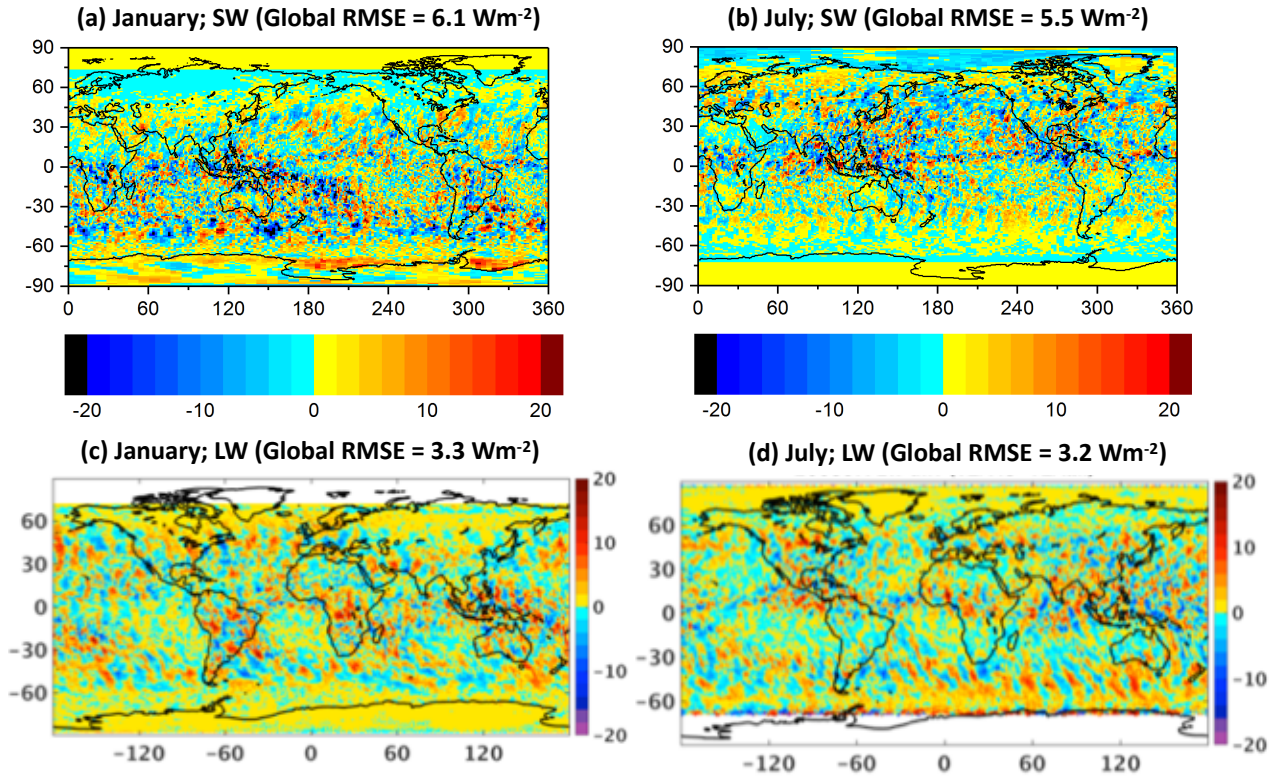

Figure 5.3 Regional monthly mean TOA flux error due to reduced geographical coverage (Wm^{-2}). SW TOA flux difference for VZA < 45° minus VZA < 70° for (a) January, (b) April, (c) July and (d) October 2008.

Reduced geographic coverage has both practical and scientific implications. First, it hinders the ability to assess and attribute inter-satellite differences since it reduces the number of coincident samples that can be acquired from instruments on different platforms. Secondly, in order to produce a consistent record, the entire CERES CDR would need to be reprocessed with the same geographical coverage throughout. In the example above, this would mean discarding all CERES observations with VZAs > 45° from the start of the CERES record onwards, resulting in larger errors over the entire CERES CDR. The increase in error associated with reduced geographic coverage would impact research in each of the ERB science focus areas in Section 3. For example, in order to determine the contributing factors explaining the spatio-temporal variations in ERB, it is necessary to resolve ERB both regionally and daily. This is because regional ERB variations are strongly influenced by phenomena occurring over short time scales. In the tropics, this includes equatorial waves, Madden-Julian oscillation and monsoons, which occur at synoptic, intraseasonal and seasonal time scales. In addition, it is becoming increasingly evident that regional patterns of warming and the associated patterns of low cloud response to the warming play a crucial role in determining the magnitude of global cloud feedback (Andrews et al., 2012; Armour et al., 2013; Zhou et al., 2016, 2017). This means that in order to constrain cloud feedback due to global warming from observational records, ERB observations need to provide CRE changes with time at both regional and global scales. Because reduced geographic coverage results in large regional TOA flux errors, our ability to observationally constrain cloud feedback

would be degraded. Finally, restricting geographical coverage would reduce clear-sky sampling, which is required to infer aerosol radiative effects. Thus, in order to preserve the quality of the ERB CDR at the present level and continue to support ERB science, the ERB SWG recommends that the new ERB instrument provide near-global coverage daily.

5.1.4 Angular Sampling

Each of the CERES instruments is designed to scan from limb-to-limb in different scan modes. In crosstrack mode, the scan is perpendicular to the groundtrack, enabling global coverage daily. In alongtrack mode, the instrument scans along the ground track to provide multiangle views of the same target. CERES is also able to rotate in azimuth as it scans in elevation (RAP mode), thereby acquiring radiance measurements from multiple Sun-Earth-satellite viewing geometries. Finally, in the programmable azimuth plane scan mode (PAP), commands are uploaded and sent to the instrument in order to optimize sampling over specific targets (e.g., field campaigns) or to intercalibrate with other instruments by aligning the CERES scan plane with that of the other instrument. This ability to scan in different modes has been a tremendous asset during the CERES project. It has been a critical part of CERES algorithm development and validation efforts.

CERES radiative fluxes are determined from measured radiances by applying empirically derived ADMs that describe the angular dependence of the TOA radiation field (Loeb et al., 2005, Su et al., 2015a). Since the angular dependence is a strong function of scene type, the ADMs are classified according to imager-derived scene properties. In order to acquire sufficient sampling to construct ADMs, multiple years of RAP data are needed. Thus far, separate ADMs have been developed for CERES PFM on TRMM, CERES FM1 and FM2 on Terra, and CERES FM3 and FM4 on Aqua. For CERES PFM on TRMM, sampling was limited due to its premature failure. For Terra, just under 5 years of RAP data were used, while just under 3 years were available for Aqua (Su et al., 2015a). The CERES team plans to produce ADMs from CERES FM5 on SNPP and use those to infer TOA fluxes from the CERES instruments on both SNPP and NOAA-20. These two missions fly virtually identical instruments at the same altitude (825 km).

While it would be highly desirable to retain the unique angular sampling capability of CERES in the new ERB instrument, the ERB SWG recognizes that this could be technically challenging and costly. Since ADMs have already been developed on Terra and Aqua and will soon be developed with FM5/SNPP, it would be possible to apply those ADMs to the new ERB instrument, obviating the need to build a new set of ADMs. Eliminating the need to construct ADMs with the new ERB instrument significantly relaxes the needed angular sampling characteristics compared to that for CERES and RBI. However, reducing the angular sampling on the new ERB instrument would preclude validation of the accuracy in instantaneous radiative fluxes for the new instrument based upon the kinds of multiangle consistency checks used routinely with the CERES sensors. It will also significantly limit our ability to perform intercalibration checks with other instruments or support field campaigns as they arise. The choice to relax the angular sampling capability is therefore entirely pragmatic, based upon the cost constraints of the EVC program rather than science.

Thus, the ERB SWG recommends angular sampling that is consistent with CERES cross-track mode as a threshold characteristic and angular sampling consistent with all CERES scan modes as an objective.

5.1.5 Radiometric Accuracy

The CERES instrument has absolute accuracies of 1% (k=1) for SW and 0.5% for LW and TOT. While recommended here for the EVC instrument given the program's continuity mission, these accuracies are insufficient to provide an accurate independent value of EEI. However, as has been demonstrated in several studies, the CERES record is able to accurately track variations in EEI on time scales ranging from monthly to interannual due to instrument stability characteristics, careful attention to in-flight calibration, and near-global coverage daily (Loeb et al., 2012a, 2016c). With a longer record, it will also enable observation of decade-to-decade variations in EEI and an assessment of feedback contributions to EEI for the first time. In order to overcome the absolute calibration uncertainty, the CERES global mean net TOA flux is anchored to a long-term mean EEI, based primarily on the Argo ocean profiling network. The approach used to anchor the CERES global net flux to EEI is by adjusting global mean SW and LW TOA flux values within their respective uncertainties via a Lagrange multiplier objective constrainment technique (Loeb et al., 2009a). If the SW and LW absolute uncertainties were too large owing to poor absolute calibration, this would result in a situation in which the SW and LW components of net TOA flux would be erroneous even though the net TOA flux was well constrained. This arguably would defeat the purpose of constraining to in-situ EEI and make the ERB observations of questionable value for climate model evaluation, which depends upon having accurate SW and LW observations. The SWG therefore recommends maintaining the radiometric accuracy of the new ERB instrument at least at the CERES level. With coincident intercalibration measurements from the Climate Absolute Radiance and Refractivity Observatory (CLARREO) (Wielicki et al., 2013), improved absolute accuracy beyond what is achievable with CERES is feasible with sufficient intercalibration opportunities, but that would still be insufficient to provide an absolute accuracy of EEI to better than 0.3 Wm^{-2} (1σ).

Recently, some have proposed mission concepts to measure EEI to 0.3 Wm^{-2} absolute accuracy (1σ) using nonscanner WFOV instruments. The ERB SWG is highly skeptical that such an absolute accuracy is achievable solely from satellites. Since the total outgoing radiation is ≈340 Wm^{-2}, this means an absolute accuracy of < 0.09% would be required to achieve this goal. The use of broadband WFOV instruments for measuring the global net radiation budget is not a new concept, with such instruments aboard the Nimbus 7 satellite between 1978 and 1988 as well as on the ERBE mission between 1985 and 2005. More recently, a European-lead PICARD satellite mission produced a limited 37-month data record of global net radiation from a WFOV instrument. Unfortunately, the on-orbit accuracies of these WFOV instruments failed to meet their prelaunch accuracy goals owing to inherent challenges in calibrating these types of instruments. Importantly, the absolute accuracies of these early missions (Nimbus 7 and ERBE) were of order 2-5 Wm^{-2}, roughly an order-of-magnitude less stringent compared to those promised for future WFOV instruments. However, these new missions have not addressed how to overcome the on-orbit challenges experienced during the earlier WFOV missions and meet such stringent absolute accuracy characteristics. For a detailed discussion about the calibration challenges with WFOV instruments, see Wong et al. (2018).

5.1.6 Radiometric Stability

One of the most challenging characteristics for a CDR is to enable unambiguous detection of long-term trends in the climate system. This requires a well-characterized set of instruments

on multiple platforms whose calibration systems can detect and correct instrument changes so that real climate system changes can be identified without the confounding influence of instrument artifacts or calibration drifts. In practice, achieving a given stability goal requires use of both onboard calibration sources and vicarious calibration (Priestley et al., 2011). For CERES Terra and Aqua, after applying instrument gains determined from onboard calibration sources, SW channel SRF changes are determined vicariously through a direct comparison of coincident CERES nadir radiances from instrument pairs on the same platform (Thomas et al., 2010). The loss of transmission with wavelength (or spectral degradation) is represented by an exponential relationship with one free parameter, which is inferred monthly from CERES nadir radiances. We assume the instrument in RAP mode degrades relative to the crosstrack instrument and account for any drift in the ratio of coincident unfiltered radiances. After applying this approach independently to CERES instruments on Terra and Aqua, trends in monthly anomalies are consistent to 0.21 Wm^{-2} per decade for ocean, and 0.31 Wm^{-2} per decade for land (Loeb et al., 2016c). Relative to the global mean SW flux, this consistency corresponds to < 0.25% per decade.

In the LW, daytime measurements are the most challenging, as they involve removing the contribution from the SW portion of the TOT channel with the SW channel radiance measurement. To account for SRF changes in the SW portion of the TOT channel, a spectral degradation relation similar to that for the SW channel is assumed (Loeb et al., 2016c). After applying instrument gain coefficients to the TOT and SW channels, and accounting for SRF changes in the SW, linear regression coefficients are computed each month for tropical daytime-nighttime LW versus daytime-nighttime WN radiance differences for all-sky ocean and all-sky land/desert scene types. A correction to the SW portion of the TOT SRF is derived using the spectral degradation curve that yields the smallest variation in regression fits compared to the first month of the mission. This ensures that the relationship between tropical daytime-nighttime LW and daytime-nighttime WN radiance differences remains consistent throughout the mission. When this method is applied to Terra and Aqua, global daytime–nighttime LW differences remain stable throughout the missions over both global ocean and land/desert. When the CERES Terra and Aqua Edition 4 LW TOA fluxes are compared, their trends are consistent to 0.16 Wm^{-2} per decade (Loeb et al., 2016c). Relative to the global mean LW flux, this consistency is < 0.1% per decade. As with SW, this is well below the threshold capability of 0.3% per decade (k=1) in Table 5-1, indicating that the stability capability recommended in Table 5-1 is not overly restrictive. In addition to showing consistent trends, monthly anomalies are very close. Differences between global monthly anomalies from CERES instruments on Terra, Aqua and SNPP are < 0.12 Wm^{-2} for SW, < 0.16 Wm^{-2} for LW and < 0.17 Wm^{-2} for net TOA flux (Loeb et al., 2018b). Recent comparisons between CERES LW and AIRS narrowband-to-broadband LW monthly anomalies and short-term trends also show a remarkable degree of consistency (Susskind et al., 2012; Huang et al., 2012; Su et al., 2017).

5.1.7 Radiometric Precision and Linearity

The needed instrument radiometric precision capability is < 0.2 Wm^{-2} sr^{-1} + 0.1% of measured for SW, < 0.45 Wm^{-2} sr^{-1} + 0.1% of measured for LW, and < 0.3 Wm^{-2} sr^{-1} + 0.1% of measured for TOT. The linearity capability is 0.3% from linear over dynamic range (k=2).

5.1.8 Onboard Calibration System

The primary purpose of an instrument's onboard calibration subsystem is to: 1) provide traceability post-launch to the primary absolute standards utilized during the pre-launch calibration testing, and 2) enable detection, quantification and correction of changes in instrument sensitivity (temporal, spatial, spectral, and dynamic response) throughout the mission so that subtle changes in the climate system can be unambiguously detected. For a broadband instrument, this typically involves variable temperature blackbodies in the infrared part of the spectrum and visible calibration sources and targets in the reflected solar or SW portion. These multiple sources/targets should cover the broad dynamic and spectral ranges of the earth observations. In the SW, both the gain and spectral response of the instrument can change with time. Inferring LW from TOT minus SW can require calibration corrections to the SW channel and/or the SW portion of the TOT channel, both of which can degrade independently.

It is well established that instrument UV exposure and molecular contamination cause a loss of measurement sensitivity with time, particularly in the blue end of the solar spectrum (Priestley et al., 2011). Evidence of spectral darkening exists from MODIS, VIIRS, GOME, and many other instruments (Coldewey-Egbers et al., 2008; Xiong et al., 2016), as well as from the Long Duration Exposure Facility (LDEF) experiment (Herzig et al., 1993), a dedicated experiment to measure spectral degradation of different materials exposed to space. In each case, the loss of sensitivity is wavelength dependent: the degradation is most pronounced at wavelengths less than 0.5 μm. The degree of radiometric degradation varies from mission-to-mission in an unpredictable manner, depending on the specific species of contaminant and operational scenario. For MODIS and GOME, the changes are easily corrected because these instruments have functioning onboard calibration equipment. It should also be noted that the MODIS and GOME sensors make measurements in narrow spectral bands and have small (~1km and less) fields-of-view with accuracy requirements a factor of 2 to 5 less stringent than CERES, all of which simplify their task.

Lacking such capability, the only viable option is to use Earth scenes to gauge the stability of the instrument. That approach requires considerable effort by the instrument calibration team and depends on the stability of the scenes considered, which is generally not known a priori at the required accuracy levels. For example, if one wanted to correct for spectral degradation at short wavelengths, a logical choice would be to monitor measured reflected solar radiances from cloud-free ocean scenes since they contain proportionately more energy than cloudy scenes at wavelengths below 0.5 μm, where spectral degradation is most pronounced. However, the spectral content and magnitude of reflected solar energy from cloud-free ocean scenes is heavily influenced by aerosol and surface albedo changes, and there is no known way to accurately distinguish between these potential changes and changes occurring in the instrument. Hence, reliable independent onboard calibration is vital to sort between changes in the instrument and Earth targets. Use of Earth scenes as an absolute stability metric is not viable for the CERES calibration requirements. With sufficient temporal and angular matching of observations, Earth scenes are nonetheless useful for relative comparisons amongst channels/instruments and as a validation that onboard calibration sources are performing as expected.

During the CERES design phase, spectral darkening due to molecular contamination of optical components was determined not to be an issue. Therefore, the primary criteria for the onboard calibration subsystems were knowledge and traceability of the radiometric sources

utilized, rather than spectral stability of the entire optical path (including the sources) within the subsystem. However, early in Phase-E of the CERES Terra and Aqua missions the science team noticed significant decreases in albedo that varied as a function of scene-type. The results demonstrated a decreasing trend for deep convective cloud of 0.25% and 2.8% per decade for FM1 and FM2, respectively, and a decreasing trend in tropical mean clear ocean of 3.5% and 7.5% per decade for FM1 and FM2, respectively. The clear ocean change significantly exceeded expectation based upon MODIS radiance and aerosol optical depth changes for the same period. Because the magnitude of the change was different for these two scene types, it could not be explained as a drift in the SW channel radiometric gain since such a change would be independent of scene type.

Unfortunately, the main tool for monitoring long-term on-orbit SW calibration stability (i.e., the Mirror Attenuator Mosaic, or MAM, a solar diffuser plate that attenuates direct solar view) provided no insight for unscrambling these trends, as the surface reflectance properties of the attenuator changed significantly with time, and the design of the legacy MAM subsystem did not include an independent reference detector to quantify and correct this change. Consequently, the CERES calibration team decided not to use the MAMs as a discriminator in their cal/val protocol for Flight Models 1-4 on Terra and Aqua. For FM5 and FM6, MAM performance improved significantly.

The CERES SW Internal Calibration Source (SWICS), a single evacuated quartz tungsten lamp operated at three discrete current levels producing spectra roughly equivalent to 2100 K, 1900 K and 1700 K brightness temperatures, showed changes of only a few tenths of a percent, or an order-of-magnitude smaller than the clear-ocean albedo trends. This apparent contradiction occurs because the bulk of the energy for the SWICS is concentrated at wavelengths > 1 μm, where spectral darkening is suspected to be minimal. The solar diffuser (MAM), by nature of the solar spectra, would provide information in the wavelength range below 1 μm. Consequently, the CERES onboard calibration equipment failed to help detect, quantify, and correct for the spectral darkening observed on CERES FM1-FM4. Instead, the CERES team relied on the direct comparison of CERES radiances from the CERES instrument pairs on both platforms to compensate for the spectral darkening. They noted that the spectral darkening was a strong function of instrument scan mode, with the RAP instrument showing enhanced degradation relative to the instrument in crosstrack mode. Assuming the crosstrack instrument was stable, calibration corrections were made to the RAP instrument by adjusting its SRF in time to ensure consistency between coincident nadir measurements from the two instruments. We note that this approach was only possible because Terra and Aqua flew pairs of CERES instruments. Because FM5 and FM6 fly 'solo' on the SNPP and NOAA-20 satellites, respectively, this approach is not feasible. Consequently, the instruments have remained in crosstrack mode. In the case of FM6, careful attention was also paid to potential contamination of optical surfaces during ground testing, and the MAM underwent additional pre-conditioning.

Based upon the CERES experience, it would be highly desirable for the future ERB instrument to provide a way of monitoring instrument degradation across a range of wavelengths, including the 0.3 to 0.5 μm region. As noted earlier, all instruments degrade in the space environment. The onboard calibration system needs to account for these changes so that Earth changes can be detected independently of changes in the instruments themselves. The RBI design included a visible calibration target as part of its onboard calibration system to monitor

spectral degradation in narrow spectral bands at short wavelengths (<1.8 μm). It is unclear how well that approach would have worked in practice had RBI flown, but it appeared to be a promising step forward. Alternately, another way to minimize the impact of instrument degradation is to design and operate the instrument to reduce exposure to in-orbit degradation. This could also involve "pre-conditioning" the instrument prior to launch in order to minimize the post-launch changes, as was done on CERES FM6. The ERB SWG recommends that the EVC instrument be designed with careful attention to the onboard calibration system to enable characterization across the broad spectral and dynamic range of the Earth Scenes being measured.

5.1.9 Vicarious Calibration

As an independent check that the onboard calibration system is functioning adequately and that there are no unexpected spurious drifts that go undetected by the instrument, it is useful to monitor Earth targets known to be relatively stable, such as deserts and deep convective clouds (DCCs), as well as other sources such as the sun (e.g., via a solar diffuser) and the moon. At infrared wavelengths, onboard calibration systems are usually robust so there is less need for vicarious calibration. In the UV to visible region, onboard calibration has historically been more challenging, making vicarious calibration a useful part of the instrument calibration protocol. For CERES, the CERES team routinely performs three-channel intercomparisons to verify calibration (Priestley et al., 2011). In that approach, daytime LW is derived using both daytime TOT minus SW, and via nighttime-derived TOT vs WN regressions applied during daytime for DCC scenes. With a WN channel, the approach only works for DCCs because water vapor variability above DCCs is minimal, resulting in a tight relationship between TOT and WN radiances. The LW channel on FM6 greatly expands the three-channel intercomparison to all scenes, not just DCCs. SW channel stability checks using DCCs and desert scenes are useful but are generally less reliable compared to their use in narrowband stability checks owing to particle size variations in DCCs and spectral variations of desert targets. Similarly, while clear-sky ocean has more energy in the blue region, where instrument degradation is generally stronger, it is a challenge to unambiguously separate systematic changes in aerosol concentration and type from potential instrument drift.

As noted earlier, degradation at wavelengths below 0.5 μm impacts virtually all instruments that measure reflected solar radiation, and arguably can only be independently corrected for using the instrument's onboard calibration system. Some have proposed using the moon or the sun as stable calibration targets for monitoring and correcting broadband instrument calibration changes. While these are indeed quite useful, the moon and sun have their own unique spectral signatures that differ markedly from the wide range of reflected spectral shapes of Earth scenes, and also have a fixed brightness level that provides a two-point calibration (space to solar/lunar target) that is unable to separate a dynamic gain change from offset, or a change in spectral transmission. As a result, the sun and moon add value and complement a broad and robust calibration and validation protocol, but on their own cannot be used to account for spectrally dependent changes that we know can occur for a broadband instrument.

Thus, while vicarious calibration is extremely useful and should be an integral component of an ERB instrument's calibration protocol, the SWG does not believe that it is a substitute for onboard calibration.

5.1.10 Potential for Future Reference Spectrometer Intercalibration

The 2007 and 2017 Decadal Surveys called for reference spectrometers in orbit to support on orbit calibration of a wide range of reflected solar and thermal infrared sensors at climate change accuracy (NRC, 2007, NASEM 2018). These spectrometers are designed to provide international standards (SI) traceability across the full reflected solar and infrared spectrum with the ability to match other sensors such as CERES, VIIRS or geostationary imagers and sounders in space, time, viewing angle, and spectral response. The resulting matched Earth viewing observations during orbit crossings then provide an independent path to SI traceability for these sensors over decadal time periods and thereby reduce the impact of calibration drifts or calibration shifts across data gaps in CDR space based observations (Wielicki et al. 2008, Lukashin et al. 2012, 2013, Roithmayr et al. 2014a, 2014b, Tobin et al. 2016). The reflected solar reference spectrometer is designed to use a 2-axis gimbal to allow time/space/angle of view matching across the entire scan swath of a low Earth orbiting radiometer or a geostationary radiometer. The gimbal enables intercalibration as a function of scan angle thereby allowing verification of calibration changes with scan angle mirror degradation, as well as determination of scan angle dependent polarization dependence (e.g MODIS, VIIRS). Finally, the ability to match across scan angles provides 100 times more coincident observations than current GSICS Simultaneous Nadir Overpass (SNO) methods. This greatly increased matched sampling enables separate characterization of calibration accuracy as a function of dynamic range (nonlinearity), orbit position (thermal heating effects on performance) and Earth scene type (CERES and other sensors spectrally dependent degradation dependence on scene type), and scan angle dependent polarization sensitivity (Lukashin et al. 2013).

Since the 2007 Decadal Survey, these reference calibration spectrometers have been developed and demonstrated in the laboratory and on high altitude balloon flights (Kopp et al. 2017). The accuracy of these spectrometers would be sufficient to calibrate CERES type broadband sensors across data gaps, with 0.3% k=2 SI traceable absolute accuracy in the reflected solar spectrum and 0.07K k=2 accuracy in the infrared spectrum (Wielicki et al. 2013). The spectrometers are designed to cover over 95% of all broadband SW and LW energy to space to enable intercalibration of CERES-like broadband sensors (Wielicki et al. 2013).

The current status of CLARREO-like reference spectrometers is that no long-term observations of this type are planned. Instead, the next step toward this type of climate reference calibration is a CLARREO Pathfinder mission to the International Space Station. This mission is currently in phase A development with a planned launch to ISS in early 2023. Its goal is to demonstrate both SI traceable absolute accuracy of a reflected solar spectrometer at 0.3% k=1 and to demonstrate intercalibration of CERES and VIIRS at the same level of uncertainty. The spectrometer is based on an existing University of Colorado LASP instrument that demonstrated the new capability in a high-altitude balloon flight in 2016 (Kopp et al. 2017). The spectrometer has contiguous spectral coverage from 350 nm to 2300 nm covering over 95% of reflected solar energy to space, with spectral sampling of 3 nm.

As a low cost demonstration mission, CLARREO Pathfinder is currently funded for 1 year of operations on ISS. Additional lifetime on orbit is to be determined at a later time based on successful demonstration on ISS. Operation of ISS is currently only assured to 2024 with international discussions to potentially continue to 2028. The launch of JPSS-3 relevant to the EVC competition is planned for launch 4 years after the CLARREO Pathfinder ISS mission. Currently NASA has not committed to extending the Pathfinder lifetime beyond 1 year. As a result, Pathfinder will provide a calibration reference for the CERES instruments still operating at that time. It is not clear, however, if the instruments will be allowed to operate on ISS long enough to overlap with the EVC broadband sensor relevant to this study. The Pathfinder spectrometer is required to have a lifetime design of at least 1 year on orbit at 0.85 survival (Class D mission). Likelihood of survival to provide reference calibration overlap with EVC in an extended mission operations would therefore be approximately 0.50. The final constructed instrument reliability analysis may exceed the 1 year requirement, but this will not be known for several years further into the Pathfinder project. There is currently no commitment by NASA or other space agencies to maintain long term reference calibration spectrometers in orbit that could be used to determine the stability of the EVC broadband instrument over its expected lifetime. We conclude that the CLARREO Pathfinder reference spectrometer cannot be counted on at this time to reduce the impact of data gaps on this CDR, or to affect its need for onboard calibration.

5.1.11 Mission Class and Lifetime

The RBI was a Class B instrument with a lifetime design requirement of 7 years with a survival probability of 0.85. While long lifetime is desirable, the cost of designing and building to such a requirement is prohibitive. It is therefore necessary to lower the lifetime requirement to fit with the cost cap of the EVC program. The recommendation is for a Class C instrument with design lifetime of 5 years with a survival probability of 0.7. The existing CERES instruments were built to a design lifetime of 5 years at 0.85 survivability.

5.1.12 Orbit

In order to exploit the current CERES processing software and provide for continuity, the radiometer needs to be placed into a sun-synchronous polar orbit at an altitude of between 700 and 850 km, with an afternoon (1:30 PM) equator crossing time. The CERES instruments on the Aqua and Terra satellites orbit at 705 km, which results in a ground footprint of approximately 20 km (equivalent circle diameter at nadir). At the 824 km orbit of the Suomi-NPP and JPSS-1 satellites, the ground footprint is about 25 km.

This range orbit will allow for reuse of the ADMs created by the CERES instruments, which convert the radiances measured by the instrument to radiative flux. Since the current ADMs do not have sampling for solar zenith angles less than 20 degrees, equator-crossing times closer to local noon would require an instrument design that would allow for the production of new ADMs. In addition, the strong diurnal variability of clouds makes it difficult to move too far away from the CERES equator-crossing time without causing a potentially large discontinuity in the radiation budget data record. That is, there is a limit to the degree to which we can adjust for cloud diurnal variability. Estimates made of the impact of proposed changes in the Terra equator crossing time on the Terra/CERES data set suggest that no more than a 15-minute variation in crossing time is acceptable.

Another critical characteristic is that the ERB instrument either fly on the same platform or in formation with a capable imager (Section 5.2). The CERES algorithms combine imager data (MODIS or VIIRS) with CERES broadband measurements in order to apply the CERES ADMs. The imager-derived aerosol and cloud properties are also used in order to determine surface radiative fluxes. If the imager is not on the same platform as the ERB instrument, the two should observe the same scene within 3 min of each other and in the same viewing geometry.

5.1.13 Overlap

While ERB instruments are precise enough to track changes in ERB, there is a need for overlap between successive missions to enable intercalibration to the same radiometric scale and thereby prevent large artificial discontinuities in the record. Without overlap between successive instruments, there would be a loss of accuracy in the long-term record. Based upon an analysis of overlapping CERES Terra and Aqua data, Loeb et al. (2009b) recommend that at least 6 months of global or 1 year of tropical overlapping measurements between successive instruments are needed.

Ideally, intercalibration of two instruments involves using coincident measurements from the same viewing geometry and adjusting the calibration of one instrument so that its radiance is consistent with that of the other. In order to minimize the influence of spatial matching noise, it is best to collect many matched footprint pairs during the overlap period and average them over larger domains for a range of surface types and clear and cloud conditions. Radiometric scaling is best achieved by adjusting the instrument's SRF via a grey scale adjustment and, if necessary, adjusting the shape of the SRF within uncertainty to minimize differences across the different scene types. The procedure requires using unfiltered radiances and, for best results, involves using the imager to identify clear FOVs.

Alternatively, if coincident measurements are unavailable due to differences in orbit phasing, the overlap correction can be performed statistically using large-scale all-sky averages from time interpolated and space averaged data products for the individual instruments (e.g., CERES SSF1deg). Scatterplots of monthly zonal means can provide the data needed to fit a slope and intercept, which in turn can be used to scale one instrument to the other. The drawback of this technique is that it precludes making adjustments to the SRF to minimize differences across different scene types. However, one advantage is that in addition to radiometric scaling calibration differences between the instruments, this approach can account for additional non-calibration differences, for example, due to input datasets, algorithm implementation, etc.

When coincident instantaneous measurements are available for intercalibration, a useful consistency check after radiometric scaling is to compare zonal averages as described in the preceding paragraph as a final check on whether or not non-calibration differences are important. Ideally, the slope of the regression should be close to unity and the offset zero. If that is not the case and there is a large discrepancy, further investigation into the root cause of the difference is needed.

5.2 Imager

The spectral information and higher spatial resolution of the imager complements the broadband ERB instrument by providing detailed information about the clouds, aerosols and surface properties within ERB instrument footprints (Minnis et al., 2011; Minnis et al., 2018; Trepte et al., 2018; Levy et al., 2007; Hsu et al., 2004). This information is key to enabling accurate

radiative fluxes from measured ERB radiances and for identifying clear scenes used to determine clear-sky radiative fluxes. Because the angular dependence of radiance depends strongly upon the properties of the observed scene, the CERES ADMs are a function of imager-derived scene information, acquired at the same time as the CERES measurement. The relevant imager information includes whether the scene is clear or cloudy, its surface properties, cloud amount, phase, optical depth, and temperature.

Since the ADMs are constructed using scene information derived from a specific imager and retrieval approach, it is recommended that a very similar imager and retrieval approach be used when the ADMs are applied to determine instantaneous TOA fluxes from measured radiances. Using consistently derived imager-based properties to both develop and apply the ADMs minimizes possible systematic error that could arise if different scene-identification approaches are used in developing and applying the ADMs (Su et al., 2017). This is analogous to what is recommended in neural network applications: the inputs used to train a neural network should be consistent with those used when applying the neural network. If a scene type is identified differently when applying the ADMs from how it was identified when the ADMs were developed, this could cause the anisotropic factor used to convert the radiance to flux to be systematically biased.

This places an important constraint on the imager and scene identification algorithm that is used with the new EVC ERB instrument. If the new EVC ERB instrument is not equipped to produce ADMs, and ADMs from CERES FM5 on SNPP are used to determine TOA fluxes from the EVC ERB instrument, the scene identification from the imager that flies alongside the EVC ERB should be as consistent as possible with the scene identification that was used to develop the SNPP ADMs. Otherwise, there could potentially be large systematic errors in TOA fluxes from the EVC ERB due to inconsistent scene identification. This problem would be less severe if ADMs could be generated from EVC ERB since the same scene identification could be used in both developing and applying the EVC ERB ADMs. In order to increase the likelihood that the scene identification from the imager that flies alongside the EVC ERB remains consistent with that based upon VIIRS on SNPP, the two imagers arguably should have similar characteristics (e.g., spectral bands, spatial resolution, etc.). The optimal solution would be to have another VIIRS imager flying alongside the EVC ERB (e.g., on JPSS-3).

The imager is also critical for correctly identifying clear-sky areas observed by the ERB instrument. The imager spectral information and high spatial resolution can discriminate dust from cloud, identify thin cirrus, and enable cloud and clear-sky properties in broken cloud conditions, which occur frequently over ocean. Imager-derived properties are also used in CERES processing to produce surface radiative fluxes using the NASA Fu-Liou radiative transfer model (Kato et al., 2013; Rose et al., 2013; Rutan et al., 2015). To minimize inconsistencies between clear-sky identification from MODIS on Aqua and VIIRS on SNPP and NOAA-20, only spectral bands that are common to both imagers are used in CERES processing. In addition, MODIS and VIIRS are placed on the same radiometric scale through intercalibration in order to ensure cloud property retrievals derived from the two imagers are as consistent as possible.

Table 5-2 lists the imager characteristics that would satisfy this condition. The nominal spatial resolution should be 1 km, which is similar to MODIS and VIIRS. Also shown in Table 5-2 are the required spectral bands and how they are used in CERES processing to: identify pixels that are clear and cloudy (cloud mask), infer cloud properties, infer sub-footprint resolution clear-sky

TOA fluxes in partly cloudy conditions (EBAF), apply CERES ADMs for clear scenes, and determine CERES surface radiative fluxes. In the Comments column, we provide specific information about how the spectral bands are used and what each band enables.

If a MODIS or VIIRS class imager is not available to fly alongside the EVC ERB instrument, the minimum set of imager spectral bands that could still be used for scene identification are the first five shown in Table 5-2. These are essentially the AVHRR bands. They can enable discrimination between clear and optically thick clouds and provide some cloud property retrievals, but they are of limited use in distinguishing between clear and cloudy pixels in heavy aerosol conditions (dust, smoke, pollution), over snow and ice, and over thin cirrus. As a result, the ERB data product would provide a less accurate constraint on cloud feedback and aerosol forcing. In addition, in order to ensure a consistent ERB CDR, the entire CERES record would need to be reprocessed using only spectral channels common to all imagers. This would also require that the CERES ADMs on Terra, Aqua and SNPP be reconstructed from scratch using a scene identification algorithm based upon the limited imager spectral bands. Thus, a lesser imager would significantly reduce the reliability of the ERB CDR and dramatically increase the level of effort required in order to produce the most consistent ERB record possible. It follows that an EVC ERB instrument capable of measuring broadband SW and LW radiances at a 1-km resolution would not eliminate the need for an imager since it would not have sufficient spectral information to discriminate between clear and cloudy pixels.

5.3 Impact of Observing System Inconsistencies

Differences in spatial and temporal sampling between the new ERB instrument and CERES would have important implications on the quality of the entire ERB CDR. For example, a reduction in swath width would require the entire CERES CDR to be reprocessed using the same reduced swath width throughout the CDR. Similarly, if the new ERB instrument flies with a less capable imager than MODIS or VIIRS, the CERES algorithms and production code would need to be modified to use consistent imager characteristics. Thus, if the new imager has fewer spectral bands than MODIS or VIIRS, only those spectral bands common to all imagers would be used across the CDR. While these changes would likely degrade the quality of the ERB record during the 20+ years of CERES, they would minimize the chance of a discontinuity in the record when the new ERB instrument and imager are added to extend the ERB CDR beyond CERES. The algorithm and code changes required would also result in significant additional effort (and therefore cost) during Phase E.

Table 5-2 Imager characteristics needed to address various tasks within the current CERES processing system. M=Mask; R=Retrieval; *f*=cloud fraction; τ=cloud optical depth; *T*=cloud-top temperature; *Re*=effective radius; ch=channel; NB2BB=narrow-to-broadband; BB=broadband.

Task	Center Wavelength (μm)	Nadir Resolution (km)	Primary Use	Comments
To discriminate between clear and cloudy imager pixels within CERES footprints and retrieve cloud properties (*f, τ, Re, phase, T*) from pixels identified as cloudy	0.645	0.25-1.0	M, R: τ, *T*	(C1)
	1.64	1	M, R: detection and τ over snow	M: Core channels allow discrimination between clear and optically thicker clouds.
	3.792	1	M, R: *Re* , nighttime τ	
	11.03	1	M, R: *T*, nighttime τ	R: Enable cloud optical properties over wide range of conditions during daytime and for optically thin clouds at night .
	12.02	1	M, R: cirrus, aerosol, nighttime τ	
	1.375	1	M: thin cirrus detection	(C2)
	1.24	1	M, R: τ over snow, Re	M: Improve discrimination between clear and cloudy areas in difficult conditions: dust and pollution, over snow/ice, and in the presence of optically thin clouds.
	8.55	1	M, R: dust, night cloud phase	
	6.72	1	M, R: polar cloud mask, night τ	R: Enable cloud optical properties over wider range of τ. Improve information on cloud vertical structure and layering.
	13.34	1	M, R: polar night, CO2 slicing	
	2.13	1	M, R: land aerosols (w/0.469 μm ch), detection & τ over snow, Re	(C3)
	0.469	1	M: land aerosols (w/2.13 μm ch)	Further support enhancements listed in C2. May be some overlap in information content in C1 + C2 channels.
	0.858	1	M: clouds over ocean	
To infer clear-sky TOA fluxes from partially cloudy CERES footprints in order to supplement clear-sky sampling from completely cloud-free CERES footprints (EBAF-TOA)	0.469	1	SW	- N2BB regression coefficients are derived separately for each imager+CERES combination on a given
	0.645	1		
	0.858	1		
	1.24	1		- Monthly regional NB2BB bias corrections are derived from clear CERES footprints.
	6.7	1	LW	- NB2BB bias corrections are used to adjust imager-based TOA fluxes to remove NB2BB error.
	8.55	1		
	11.03	1		
	12.02	1		
	14.2	1		
To infer instantaneous clear-sky SW TOA fluxes using ADMs	0.645	1	Clear-sky land ADM scene identification	
	0.858	1		
	0.47	1	Clear-sky sea-ice ADM scene identification	
	0.858	1		
	0.47	1	Clear-ocean ADM aerosol classification	
	0.55	1		
	0.66	1		
	0.87	1		
	1.24 or 2.13	1		
To derive surface albedo over land, snow and ice surfaces from partly cloudy CERES fotprints. Used as input for surface radiative flux calculations.	0.645	1	Clear-sky snow and ice identification	Also used for NB2BB conversion to dervie BB radiacnes over a clear portion of partly clear footprints for land, snow, and ice surfaces
	0.858	1		
	1.64	1		
	3.792	1		
	11.03	1	Clear-sky snow and ice identification	
	0.469	1	NB2BB conversion to dervie BB radiacnes over a clear portion of partly clear footprints for land, snow, and ice surfaces	
	0.55	1		
	1.24	1		

Appendix A History of Satellite ERB Measurements at NASA and NOAA

The history of satellite Earth radiation budget measurements at NASA and NOAA can be traced back to the WFOV radiometers on NASA Explorer 7 satellite, which was launched into orbit on October 13, 1959. Numerous satellite missions, carrying the WFOV nonscanning and/or NFOV scanning (i.e., scanner) radiometers, were followed to measure the Earth radiation budget from space. This appendix highlights these missions.

A.1 First Generation Mission: NASA Explorer 7 WFOV Radiation Budget Detectors

In October 1957 the Soviet Union placed the world's first artificial satellite, Sputnik 1, in orbit, resulting in the 'Space Race'. NASA Explorer 7 satellite was put in space in 1959 with a set of detectors for measuring radiation from Earth. This experiment by Vern Suomi was the first instrument to study weather and climate from space.

The instrument consisted of two pairs of hemispherical sensors mounted on opposite sides of the spacecraft. The matching hemispheres on opposite sides of the spacecraft effectively constituted a sphere which was thus insensitive to the orientation relative to Earth. One of each pair was black and the other was white. The black sensors absorbed all radiation and the white sensors reflected most of the reflected solar radiation but absorbed most Earth-emitted radiation, or outgoing LW radiation OLR. From these measurements the reflected solar radiation and OLR could be retrieved.

The measurements clearly showed patterns of clouds and of clear sky, and variations of albedo and OLR over the Earth. Although primitive, these early results demonstrated the possibility of Earth radiation measurements from satellites.

A.2 Second Generation Mission: Flat Plate WFOV Radiometers on ESSA Satellites

In the second half of the 1960's the Environmental Science Services Administration (ESSA), which became NOAA, flew a series of satellites. These space crafts were in Sun-synchronous orbits and flew in cartwheel manner, i.e. with the spin axis normal to the orbit plane. The ESSA-3, -5, -7 and -9 spacecraft each carried a Low Resolution Infrared instruments. This instrument consisted of a pair of flat plate radiometers on the equator of the spacecraft on opposite sides. Each pair had a black flat plate radiometer and a white flat plate radiometer. The black radiometer measured the total radiation from Earth, i.e. the reflected solar radiation flux and the outgoing LW radiation flux. The white plate reflected most reflected solar radiation and absorbed most outgoing LW flux. The two types of radiation could be separated by the analysis, so that although the instrument was labeled as an Infrared instrument, it did give information about albedo.

While the data were available at the National Space Science Data Centre, there was no operational plan to analyze these data. These data were used mostly for basic research purposes. For example, Weaver and House (1979, NASA-TP-1402) analyzed radiometer data from ESSA 7 for September 1968 through February 1969. They developed analyses for retrieving the reflected solar radiation and OLR at the spacecraft, for calibrating the instruments in orbit and taking into account degradation of the absorbing surfaces of the radiometers, and computing shape factors for the hemispheres on a satellite spinning in a cartwheel manner. Due to resolution of the measurements and spatial sampling limitations they computed monthly-mean 10° zonal averages of reflected solar radiances and OLR. They also noted large longitudinal variations in the Tropics. Vonder Harr and Suomi (1969, 1971) used thirty-nine months of WFOV measurements

from the first generation TIROS IV and second generation Nimbus II and ESSA III satellite to determine the mean annual planetary albedo of 29%. They also analyzed the latitudinal distribution of SW and LW radiation for the first time and compared these with pre-satellite estimates from London (1957). The observations showed that Earth was warmer and darker than previously thought, especially in the Tropics. As a result, approximately 40% more energy needed to be transported poleward by the atmosphere and ocean circulations compared to pre-satellite estimates.

A.3 Second Generation Mission: ERB Information Extracted from Scanners of Opportunity

To answer other needs for radiation budget data, data products were generated using scanners designed for other uses. The National Environmental Data Information Service (NESDIS) of NOAA has produced monthly mean heat budgets from 1974 to the present. These data are reflected solar radiation flux and OLR flux and are derived from the narrowband visible and infrared channels of the scanning radiometer SR of the NOAA- 3 and NOAA-5 from 1974 through 1978 and since then from the Advanced Very High Resolution Radiometer (AVHRR). Maps of 2.5 degree resolution are produced for monthly, seasonal and decadal periods.

The Nimbus 2 and 3 spacecraft carried the Medium-Resolution Infrared Radiometer (MRIR) experiment, which measured radiation emitted by and reflected from the Earth and its atmosphere in five selected wavelength intervals from 0.2 to 23 micrometers. Four channels measured infrared radiation from 6.5 microns to 23 microns and the fifth channel measured the reflected solar radiation from 0.2 to 4 microns. Earth radiation budget information was extracted from these Nimbus 2 and 3 measurements (Raschke and Bandeen, 1970; Raschke et al. 1973).

A.4 Third Generation Mission: Earth Radiation Budget (ERB) Project

The Earth Radiation Budget (ERB) project was conducted by the Satellite Meteorology Laboratory of NOAA. The instrument (Smith et al. 1977; Jacobowitz et al. 1984) consisted of a biaxial scanning radiometer with four LW channels and four SW channels, a set of WFOV radiometers, and several solar-viewing radiometers. The biaxial scanning feature was to measure outgoing LW and reflected solar radiances from the Earth in all directions so as to construct bidirectional reflectance functions of the anisotropic radiances. The instrument was built and calibrated by Gulton Industries, except for the WFOV and solar-viewing radiometers, which were built and calibrated by the Eppley Laboratory. One ERB instrument flew on the Nimbus 6 spacecraft and another on Nimbus 7. Both the Nimbus 6 and 7 were placed in Sun-synchronous orbits with ascending nodes at noon so the data covered the Earth.

The scanning radiometer operated in several biaxial modes which were designed to gather data with which to develop Bidirectional Reflectance Distribution Functions (BDFRs), for describing the anisotropy of the radiances from the Earth in order to compute fluxes. These BDRFs (Taylor and Stowe 1984; Suttles et al. 1988, 1989) were to be used also in future projects for measuring Earth radiation budget, in particular ERBE, ScaRaB and CERES. Because of the scan patterns and the large footprint size of the measurements, measurements from the scanner were used to produce monthly-mean maps of reflected solar fluxes and outgoing LW flux with 4.5^{o} equal-area resolution. The scanning radiometer on Nimbus 6 operated for a month, September 1975. The scanning radiometer on Nimbus 7 operated from November 16, 1978 to June 20, 1980 to generate the data needed for BRDFs.

The WFOV radiometers measured the flux at spacecraft altitude and had a field of view from nadir to the limb of the Earth in all directions. The orbit altitude of Nimbus 6 and 7 was about 1100 km and 950 km, respectively, with a field of view size between 1.5 to 2 thousand km. Measurements from these radiometers were processed by use of shape factors to make monthly-mean maps of albedo and OLR. Because of the large FOV and the temporal and spatial sampling, these maps had a resolution of 10^{o}.

The Nimbus 7 ERB and other instruments gave an unprecedented view of the entire Pacific Ocean. For the first time, the movement of the inter-tropical convergence zone could be seen and related to the southern oscillation and the relation to the El Nino, known by Peruvian fishermen for centuries was recognized.

The WFOV radiometers on Nimbus 6 gave data from July 1975 through June 1978. The ERB instrument data on Nimbus 7 consisted of data from November 1978 to October 1987. These ERB WFOV data provided the first high quality global coverage by radiometers designed for broadband measurements. These data over the period month 1975 through October 1987, with missing months from July to October 1978 and in May 1986, to begin the Earth Radiation Budget CDR.

A.5 Fourth Generation Mission: ERBE Project

ERBE was developed on the basis of the recommendations of the National Academy of Sciences and a new start was funded in 1978. The project would continue the Earth radiation data record begun by the ERB project and attempt to resolve issues which ERB had raised. These issues included the requirement to calibrate all sensors and the need for a method to compute the daily-mean fluxes for a region on the basis of limited observations during the day (usually two). The WFOV radiometers were put in a separate package in order to calibrate them in orbit. Active cavity radiometers were used for the WFOV detectors. A set of scanning and WFOV radiometers was flown on three spacecraft: operational meteorological spacecraft NOAA-9, NOAA-10 and a dedicated spacecraft, the Earth Radiation Budget Satellite ERBS (Harrison et al., 1983).

NOAA 9 went into an orbit with ascending node of 0230 hours in December 1984 and the contamination covers of the ERBE instruments were opened in February 1985. The scanning radiometer provided measurements until January 1987 and the WFOV radiometers operated till 1992. NOAA 10 was placed in orbit in September 1986 and the ERBE radiometers began making measurements of Earth radiation in January 1987. The scanning radiometer stopped working in May 1989 and the WFOV continued until 1995. Information about the diurnal cycle of radiation is needed to compute the daily-mean radiation over any given region. To get this information, the ERBS was placed into an orbit with 57º inclination so as to precess through all local times in a 72 day period. The scanner aboard ERBS operated for five years, ceasing operation in February 1990 and the WFOV gave data until October 1999, to provide a 15-year CDR with one instrument. In October 1999 a calibration procedure during which the radiometers were rotated to view the Sun as a calibration source, the radiometers did not return to the nadir viewing position, but remained tilted. The tilt angle was computed and an algorithm was developed to retrieve SW flux from the WFOV. The nonscanner provided five more years of data and was turned off in August 2005.

Data from the ERBE scanning radiometers were used to produce daily maps of Earth radiation with a resolution of 2.5º. The WFOV measurements were processed by use of shape factors to generate monthly-mean maps with 10º resolution.

ERBE data were used to demonstrate that the net effect of clouds is to cool the Earth (Ramanathan et al., 1989). Measurements from the scanner aboard the precessing ERBS were used to define the diurnal cycles of OLR and albedo (Harrison et al., 1988, Smith et al., 2003; Rutan et al., 2014). Minnis et al. (1992) used WFOV data to compute the effects of the eruption of Mount Pinatubo on albedo and OLR and demonstrated there was a net cooling effect of the aerosols thrown into the stratosphere. WFOV data was also used to study decadal variability of tropical mean earth radiation budget (Wielicki et al., 2002 and Wong et al., 2006).

A.6 Fifth Generation Mission: Clouds And Earth Radiant Energy System (CERES) Project

The CERES project continued the radiation budget data record after ERBE and CERES instruments are currently operating. The primary goal of the CERES project is to produce high quality Earth radiation budget data set at TOA, surface, and at various levels within the atmosphere. A secondary objective was to collect measurements from which improved models of bidirectional reflectance functions BDRFs of scenes over the Earth could be developed so as to improve the accuracy of fluxes computed from measured radiances. At this time, researchers wanted improved spatial resolution, so the CERES data products would have 1º resolution. This in turn required the instrument have a smaller field of view. Also, greater accuracy was demanded, which required improved calibration on ground and in-orbit. The CERES instrument was designed as an upgrade of the ERBE scanner. To make measurements needed for improved BDRFs, the CERES instrument was designed to rotate in azimuth so as to measure radiances in all directions as had been done by the ERB instrument and greatly expand that data base. The WFOV nonscanner was not included in the CERES mission due to its inability to accurately determine the instrument offset in space as learned from the ERBE mission.

The Proto-Flight Model of CERES was put in orbit on the Tropical Rain Measurement Mission TRMM in November 1997. It operated for eight months, at which time an electronic component began to malfunction. The instrument was turned off in September 1998. During this time data were collected for comparing with the ERBE nonscanning radiometers, thus giving overlapping data to provide continuity of the ERB CDR. Two CERES instruments, Flight Models 1 and 2 were placed on the Terra spacecraft, one to map the geographic distribution of radiation, and the other to map the directional distribution of radiance. Terra is on a 10:30 am morning orbit. These instruments began operating in February 2000 and currently continue to work with no problems after more than 16 years. The Proto-Flight Model aboard TRMM was turned back on in March 2000 so as to give data with which to compare with FM-1 and -2. CERES Flight Models 3 and 4 were included on the Aqua spacecraft to measure radiation in the afternoon. Aqua is on a 1:30 pm orbit. These instruments started Earth observations in June 2002. FM-3 continues to work well after more than a decade. The SW channel of FM-4 ceased to function after 2.75 years. CERES FM-5 was placed in orbit in October 2011 aboard the Suomi/NPP spacecraft and began measuring the Earth in January 2012. The last copy of CERES instrument (Flight Model 6) was placed in orbit in November 2017 aboard the JPSS-1 spacecraft and began measuring the Earth in January 2018. Suomi/NPP and JPSS-1 are both on a 1:30 pm orbit.

The 18 years of measurements from CERES aboard Terra and 16 years of measurements from Aqua have been used to generate robust radiation fluxes at the top of the atmosphere TOA,

at the surface and within the atmosphere. The scientific requirements for greater accuracy of the measurements have been tightened to 1% for reflected solar radiances and OLR.

A successor to the CERES instrument is now being considered. It is intended to fly with a launch readiness date of 2026.

Appendix B CERES Radiation Budget Measurements Description

This appendix provides an overview of the CERES instruments, data products and algorithms generated by the RBSP. The ERB data products are produced at multiple levels from the TOA to the surface, but we focus here on TOA only and refer to papers by Rose et al. (2013), Rutan et al. (2015), Kato et al. (2013) and Kratz et al. (2010) for further information about CERES surface radiation products. A key advance of CERES over previous ERB datasets is extensive use of coincident higher spatial resolution spectral imager measurements on both low-Earth orbit and geostationary platforms. These instruments enable a host of other variables describing cloud, aerosol and surface properties to be retrieved alongside CERES radiative fluxes. CERES has an integrated instrument/algorithm/validation science team that is responsible for monitoring the health of the CERES sensors, provide calibrated radiances (Level 1), instantaneous (Level 2) and temporally and spatially averaged (Level 3) data products, perform validation, and enable scientific investigations using the CERES data. The CERES CDRs account for the regional and global diurnal cycle of radiative fluxes and include coincident cloud, aerosol, surface, and meteorological properties so that changes in the ERB and climate system components can be investigated in an integrated manner.

Figure 2.3 provides the CERES data processing flow diagram, listing the algorithm steps and ancillary input data needed to produce the CERES TOA radiation data products. The CERES data products are divided into processing levels, defined in Table 4-1. In the following sections we will describe the CERES instruments, their calibration, and briefly discuss the algorithm steps and ancillary input data used to produce the CERES data products.

B.1 CERES Instruments

The CERES instrument (Figure B1) is a 3-channel scanning radiometer that uses precision thermistor bolometer detectors to observe radiation between 0.3 and 200 μm (TOT channel), 0.3 and 5 μm (SW channel), and 8 and 12 μm (WN channel) (Wielicki et al., 1996). Table B-5-2 provides the instrument characteristics for CERES instruments aboard the Tropical Rainfall Measuring Mission (TRMM), Terra, Aqua, and Suomi National Polar-orbiting Partnership (SNPP) satellites. The characteristics are for CERES FM6 on NOAA-20 are the same as those for CERES FM5 on SNPP except that the WN channel is replaced with a LW channel. Each channel has a Cassagrain telescope that houses the detector, primary and secondary mirrors, and forward and rear filters (Figure B2). The detector lies behind a hexagonal field stop that determines the 1.3° x 2.6° field-of-view (FOV), which is approximately a factor of 2 smaller than ERBE. The 3 CERES telescopes are coaligned so that they have a 98% common field of view. The mirrors are silver coated, providing spectrally flat response functions, except between 0.3–0.4 μm, where there is a sharp decrease in spectral response. Because the CERES scanning radiometer has a finite response time, it has a PSF that describes the response of the radiometer to a point source of radiation from a given direction (Smith, 1994). The PSF characteristics are determined by the shape of the field stop, time response of the detector (8 ms), and signal conditioning circuit.

The CERES channels are coaligned and mounted on a spindle that rotates about the elevation axis. Every CERES scan takes 6.6 s and involves a scan from space beyond the Earth limb, across the Earth to space on the opposite side, a pause at the internal calibration source, and

a scan back across the Earth to space on the other side (Wielicki et al., 1996). CERES instruments can be commanded from the ground to scan in different modes. In crosstrack mode, the scan is perpendicular to the ground track so that spatial sampling is optimized, providing global coverage daily. This is the primary mode used to produce CERES Level-3 gridded data products. The CERES rotating azimuth plane (RAP) scan mode relies on the instrument's azimuthal axis drive system to optimize angular sampling. When in RAP mode, the instrument scans in elevation as it rotates in azimuth, thereby acquiring radiances over a range of viewing zenith and relative azimuth angle combinations. CERES RAP data are needed in order to construct CERES ADMs, described in Section B.3.4. CERES can also be placed in alongtrack mode in order to acquire measurements of a target from multiple viewing zenith angles. Finally, in the programmable azimuth plane (PAP) mode, the CERES angular sampling is commanded from the ground by uploading instructions to the instrument to acquire multiangle measurements for specific scientific experiments (e.g., field campaigns, intercalibration with other instruments, etc.).

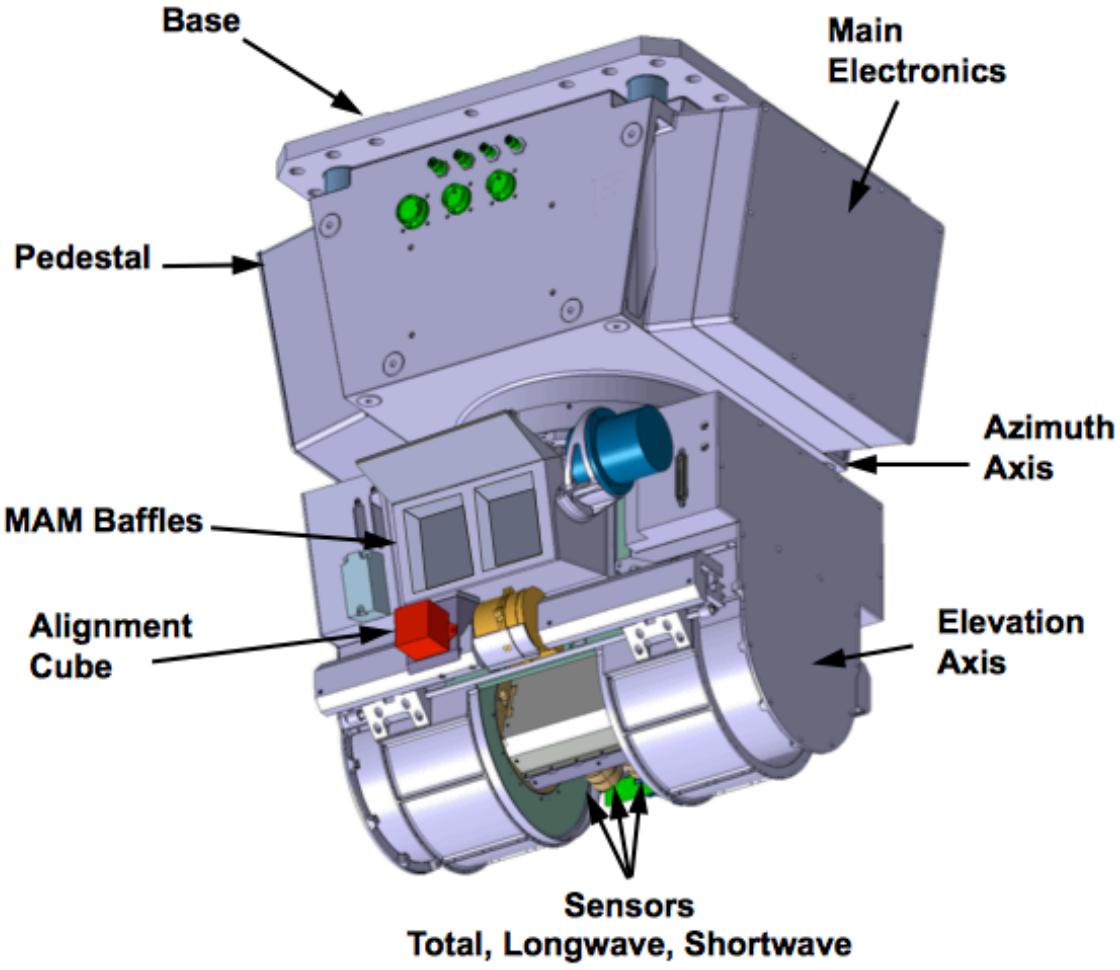

Figure B1 CERES scanning radiometer.

Table B-5-2 CERES instrument characteristics for TRMM, Terra, Aqua and SNPP missions.

	TRMM (PFM)	Terra (FM1, FM2)	Aqua (FM3, FM4)	SNPP (FM5)
Orbit	35° inclination	Sun-synchronous, near polar, 10:30 am descending node	Sun-synchronous, near polar, 1:30 pm ascending node	Sun-synchronous, near polar, 1:30 pm ascending node
Altitude (km)	705	705	705	824
Spatial Resolution (km)	10	20	20	24
Spectral Channels	Shortwave: 0.3 - 5.0 μm; Window: 8 - 12 μm; Total: 0.3 - 200 μm			
Swath Dimensions	Limb to limb			
Angular Sampling	Cross-track scan and 360° azimuth biaxial scan			
Duty Cycle (%)	100			
Mass (kg)	45			
Power (W)	45			
Data Rate (kbps)	10			
Size (cm)	60 x 60 x 70 (deployed)			
Design Life (years)	6			

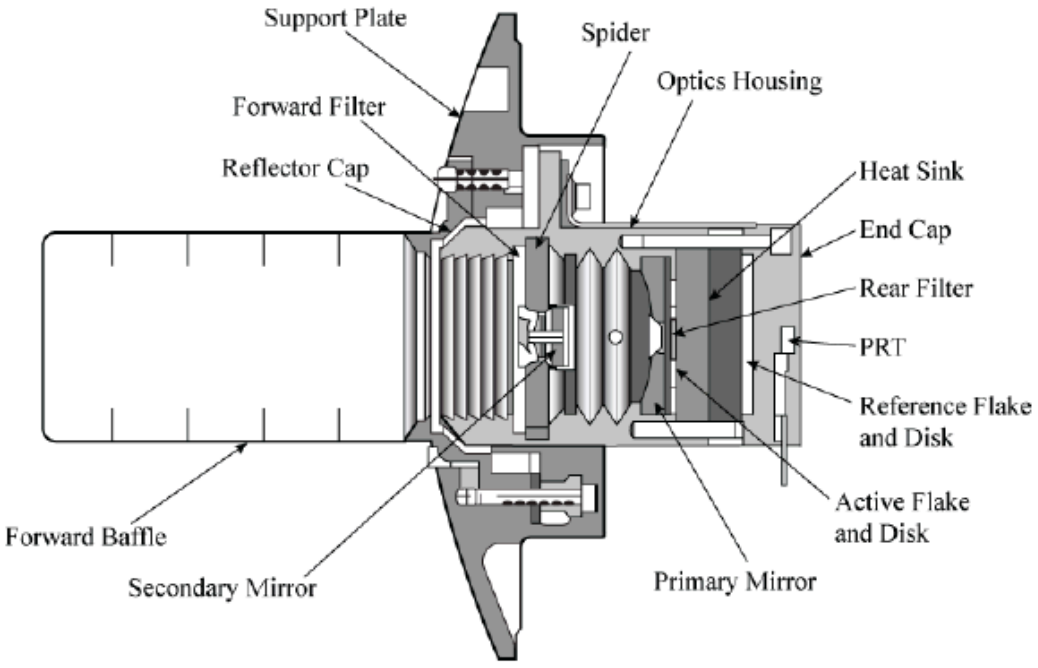

Figure B2 Cross-section of CERES telescope.

B.2 Instrument Calibration

B.2.1 Ground Calibration

Prior to launch, the CERES instruments underwent extensive ground calibration at a radiometric calibration facility (RCF) located at Northrop Grumman Aerospace Systems (formerly TRW Space and Technology Group) in Redondo Beach, California (Lee et al., 1998). It is during ground calibration that the CERES instruments are traced to absolute standards. The RCF is a calibration vacuum chamber that simulates the space environment. The CERES instrument is placed on a carousel that can be rotated and moved vertically so that it can be calibrated against different reference sources (Figure B3). These include cryogenically cooled blackbodies for LW calibration, a SW reference source, a cold space reference source, a PSF measurement source, a constant radiance reference source to test for scan-dependent variations, and a solar simulator to emulate solar calibrations. The absolute calibration for the TOT and WN channels is performed using a NFOV Blackbody (NFBB), tied to the International Temperature Scale of 1990. The blackbody source along with a Transfer Active Cavity Radiometer (TACR) is used to calibrate the Shortwave Reference Source (SWRS), which in turn brings the SW channel to the same calibration reference. The sensor responsivity is determined using the on-board sources during the pre-launch calibrations. CERES goals for absolute calibration of radiance are 0.5% for LW and 1% for SW.

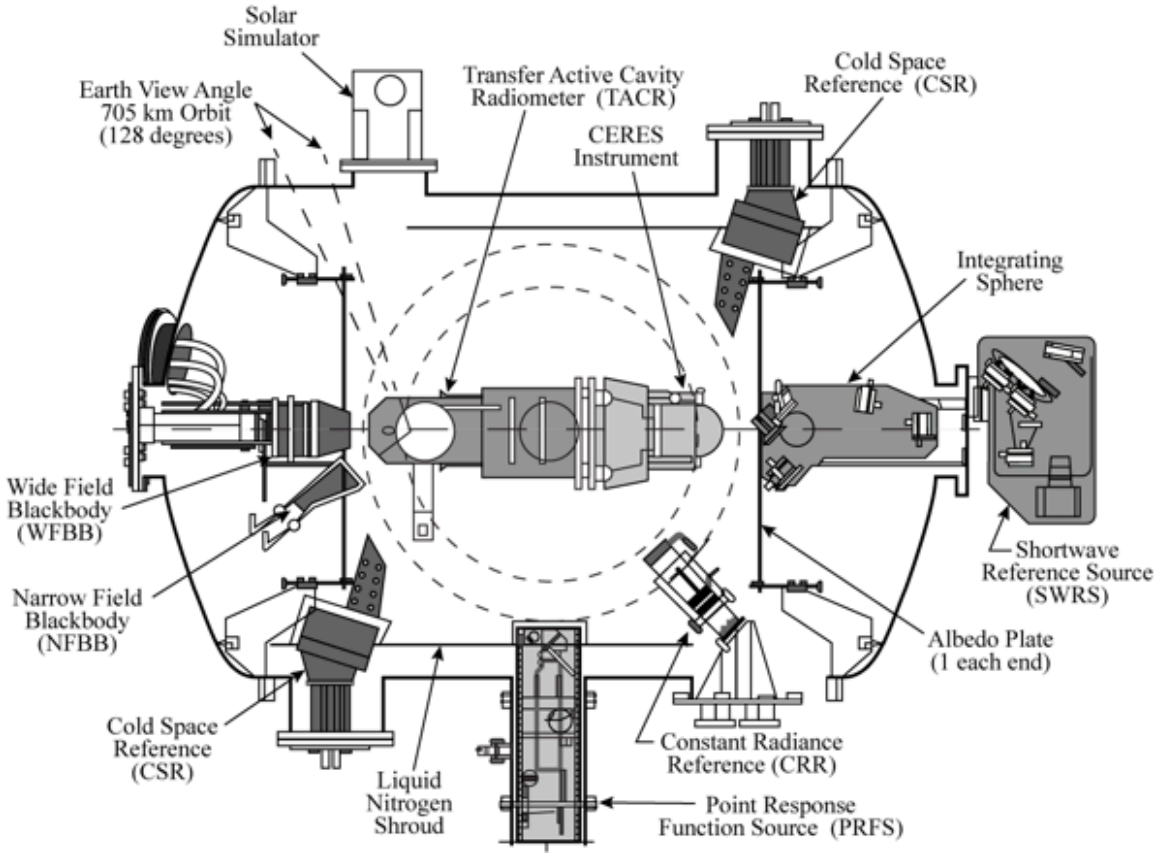

Figure B3 CERES radiometric calibration facility.

B.2.2 In-Flight Calibration Changes

Because all Earth-viewing satellite instruments experience a loss of measurement sensitivity with time (e.g., due to UV exposure, molecular contamination, etc.), the instrument needs to be monitored using a combination of the instrument's onboard calibration subsystem and vicarious calibration methods to detect, quantify and correct for changes in instrument sensitivity throughout the mission so that subtle changes in the climate system can be unambiguously detected. The accuracy and stability of the CERES CDR rests upon the ERB science team's ability to accurately calibrate the instruments and remove artificial instrument drifts. The primary in-flight calibration systems used to detect drifts in CERES sensor gains are the Internal Calibration Module (ICM) and the Mirror Attenuator Mosaic (MAM) (Lee et al., 1992; Priestley et al., 2000, 2011). The ICM consists of two blackbody calibration sources for the TOT and WN sensors and a Shortwave Internal Calibration Source (SWICS) for the SW sensor. The blackbodies operate at temperatures of 295K, 305K and 315K, and are monitored by a platinum-resistance thermometer. The SWICS consists of an evacuated quartz tungsten lamp operating at three discrete current levels producing spectra equivalent to 2100 K, 1900 K and 1700 K brightness temperatures. The radiometers observe the ICM in every normal cross-track elevation scan. Monthly gains are determined from ICM calibrations performed weekly, and a 5-month running mean is used to reduce noise. Figures B4a-e show the FM1-FM5 internal calibration results. The total channel response to LW radiation has gradually increased with time for all five instruments. The increases relative to the beginning-of-mission are 0.6% for FM1, 0.7% for FM2, 0.7% for FM3, 1% for FM4, and 0.4% for FM5. The SW channel response changed only slightly for FM1 (<0.1%), while for FM2 the change is approximately -0.4%, and for FM3 it is 0.4%. There was an increase of about 0.6% for the FM4 SW sensor through April 2005, when it failed prematurely. The FM5 SW channel response decreased by 0.2%. The window sensor gains show an increasing trend for four of the instruments except FM3, which shows a decrease with time. These instrument calibration drifts were observed over 13 years and are very small. These calibration drifts are removed when applying the calibration gain.

The MAM is a solar diffuser plate used for calibrating the shortwave sensor and the total sensor. It consists of a baffle to block stray light and a nickel substrate with aluminum coated spherical divots that attenuate and redirect the solar radiation into the field of view of the sensors. For CERES instruments on Terra and Aqua, the MAM coatings degraded in orbit and therefore were not used (Priestley et al., 2011). For SNPP, the MAMs are performing nominally thus far.

B.3 Instantaneous Clouds and Radiation: Single Scanner Footprint (SSF) Product

Once the CERES measurements have been calibrated, the next step in the CERES processing system is to produce the Level-2 Single Scanner Footprint (SSF) data product. The SSF consists of CERES viewing geometry and radiances, TOA and surface radiative fluxes, imager aerosol and cloud properties (see Section B.3.2), surface type information, solar irradiance, and meteorological data from reanalysis. SSF is a key input to higher-level CERES data products and is also extensively used by the research community in process study research (e.g., especially research on aerosol-cloud-radiation interactions). The following subsections provide a brief overview of the steps used to create the CERES Level-2 SSF product.

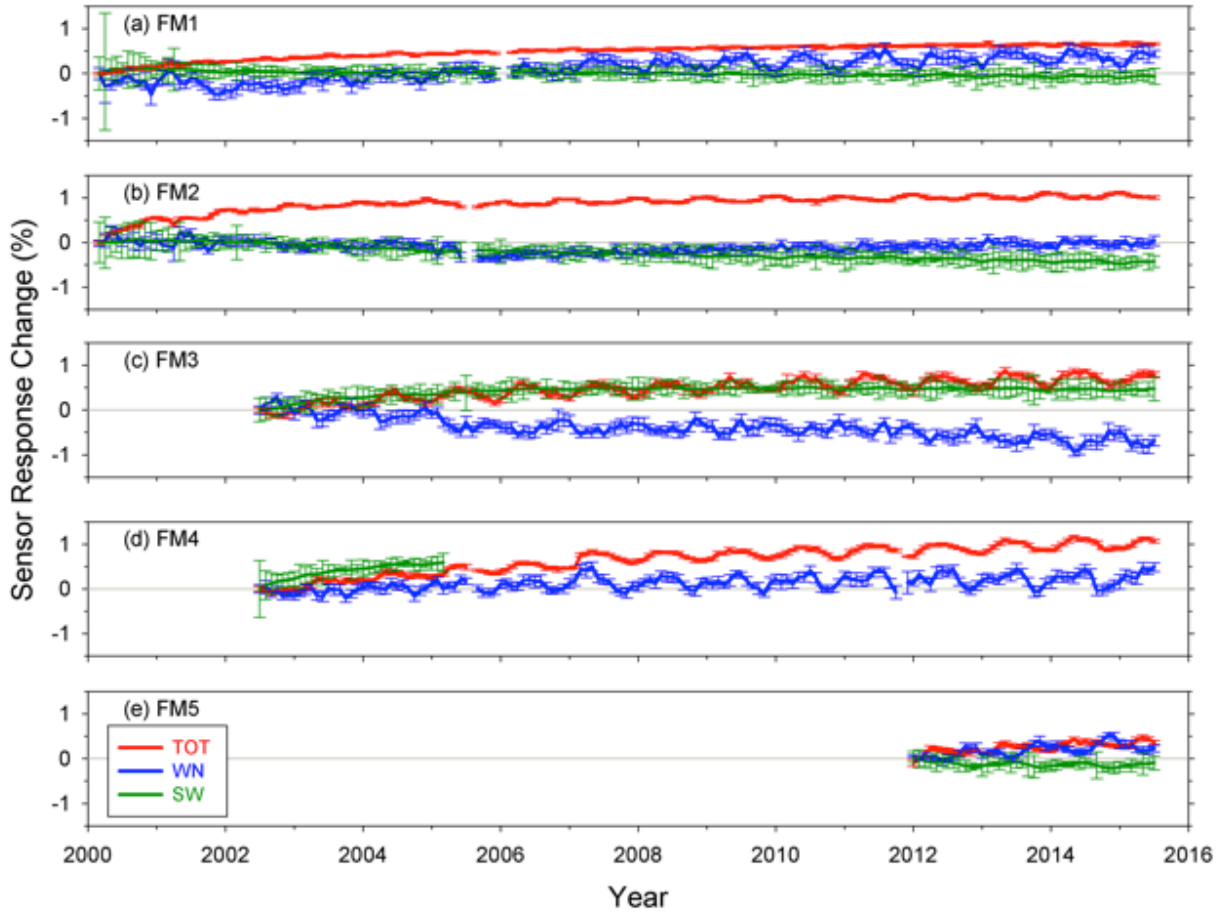

Figure B4 On-orbit sensor gain trends for CERES FM1 – FM5 instruments.

B.3.1 Unfiltered Radiances

The gain coefficients (Figure B4) convert CERES output voltages from digital counts to filtered radiances, which represent the radiation that is filtered through the instrument optics. To correct for the imperfect spectral response of the instrument, filtered radiances are converted to unfiltered radiances, which correspond to radiation received by the instrument prior to entering the optics. It is the unfiltered radiances that are converted to radiative fluxes in the CERES processing system. The unfiltering process involves applying an algorithm that relates unfiltered and filtered radiances based upon knowledge of the instrument SRF and a spectral radiance database representative of Earth scenes (Loeb et al., 2001). Shankar et al. (2010) re-evaluated the ground calibration data collected prior to the CERES Terra and Aqua launches and derived new pre-launch gains and SRFs for each CERES instrument using spectral measurements collected using a Fourier Transform Spectrometer (FTS) system along with the blackbody calibration data. Figure B5 provides CERES SRFs for the FM1 instrument. The SRFs are spectrally flat over most of the spectrum except between 0.3-0.4 μm, where there is a sharp decrease. The shape is characteristic of silver coated primary and secondary mirrors.

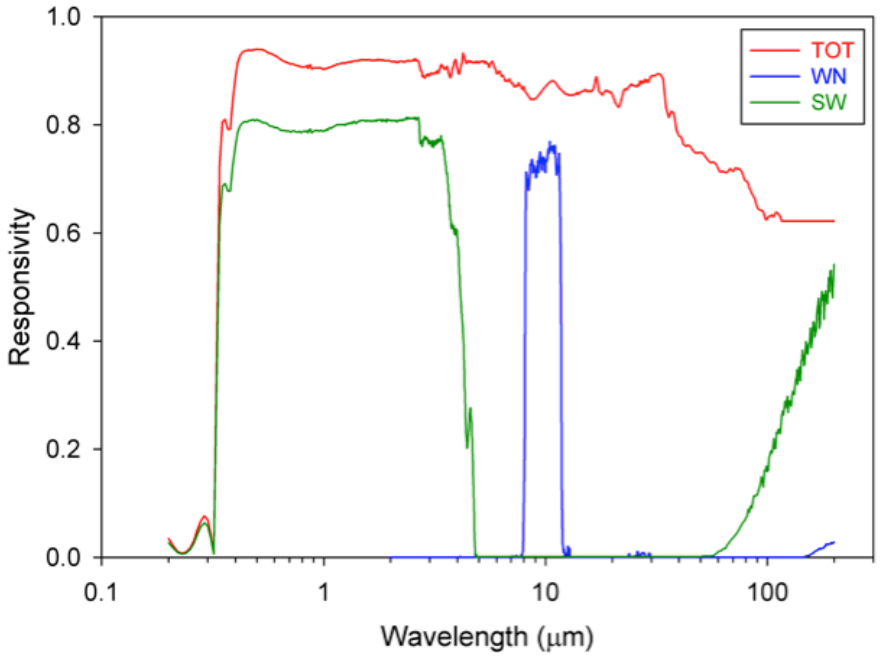

Figure B5 SRFs for CERES Sensors.

B.3.2 Imager-Derived Properties

The availability of imager measurements coincident with CERES helps increase the accuracy of CERES TOA fluxes, improves clear-sky scene identification used in determining cloud radiative effect (CRE), enables surface fluxes to be computed, and provides cloud, aerosol and surface skin temperature retrievals for attribution studies involving CERES radiative fluxes. CERES has flown with the Visible and Infrared Scanner (VIRS) on TRMM, the Moderate-resolution Imaging Spectrometer (MODIS) on Terra and Aqua, and the Visible/Infrared Imager/Radiometer Suite (VIIRS) on SNPP. Aerosol properties in the CERES SSF are produced at NASA Goddard Space Flight Center based upon Remer et al., (2008), Levy et al., (2007), and Hsu et al., (2004). The algorithms developed for MODIS are now being extended to VIIRS on SNPP. The CERES team determines cloud properties and surface skin temperatures directly from imager pixel data based upon Minnis et al. (2011). As a radiation budget project, CERES requires cloud retrievals even for the most challenging cases (e.g., near cloud edges, complex multilayer cloud conditions, etc.), which is not a common feature of cloud property datasets (Stubenrauch et al., 2013). CERES cloud algorithm changes are closely coordinated with higher-level data product algorithm changes in order to minimize sudden discontinuities in the CERES record. Also, in order to minimize the effects of algorithm shock, CERES imager-derived properties are designed to work in a consistent manner across multiple platforms (Terra, Aqua, SNPP, 20 geostationary visible/infrared imagers).

Pixel imager-based cloud property retrievals include cloud boundaries, phase, optical depth, effective particle size, and condensed/frozen water path. In the latest version of CERES SSF (Edition4), improvements to the CERES cloud algorithm (Minnis et al., 2010) include the following: changes to the cloud mask that result in better agreement with the Cloud-Aerosol Lidar and Infrared Pathfinder Satellite Observations (CALIPSO); a new ice crystal reflectance model based on rough hexagonal columns; implementation of a combined 1.38-μm reflectance and infrared technique that extends the range of cirrus optical depth retrievals to below 0.3; a multilayer

cloud detection and retrieval scheme; new clear-sky and surface albedos for the 0.65, 1.24, and 2.13-µm channels to enable cloud effective radius retrievals in all three channels; a new scheme for improved retrievals of low cloud heights based upon matched MODIS and CALIPSO data (Sun-Mack et al., 2014), new cloud thickness parameterizations from matched MODIS, CALIPSO, and CloudSat data; a new cloud-top-height technique for more accurate height assignments for optically thick ice cloud.

B.3.3 Convolution

Convolution involves the process of merging multiple datasets and averaging them over individual CERES footprints. In order to do this accurately, one must account for the instrument's PSF, which provides the weight each pixel value receives in the averaging process. The PSF of a radiometer describes the response of the radiometer to a pencil of radiance from a given direction (Smith, 1994). For a scanning radiometer, the effect of the time response of the detector on the PSF must be considered when the sampling rate is comparable to the response time of the detector. In addition, the signal is usually filtered electronically prior to sampling in order to attenuate electronic noises and to remove high frequency components of the signal, which would cause aliasing errors. The time responses of the detector and filter cause a lag in the output relative to the input radiance, so that the time response causes the centroid of the PSF to be displaced from the centroid of the optical FOV (Figure B6). In addition, the time response also increases the width of the PSF. Thus, the signal as sampled is coming not only from where the radiometer is pointed, but includes a "memory" of the input from where it had been looking (Green and Wielicki, 1996). If we define x as an imager radiance or cloud property, the weighted average value of x over a CERES footprint is given by:

$$\bar{x} = \frac{\int_{FOV} P(\delta,\beta)x(\delta,\beta)cos\delta d\beta d\delta}{\int_{FOV} P(\delta,\beta)cos\delta d\beta d\delta} \tag{B1}$$

where δ and β are the angular coordinates of a point in the CERES FOV. The PSF $P(\delta,\beta)$ provides the weight assigned to x within the FOV and is defined and discussed in detail in Green and Wielicki (1996) and Smith (1994).

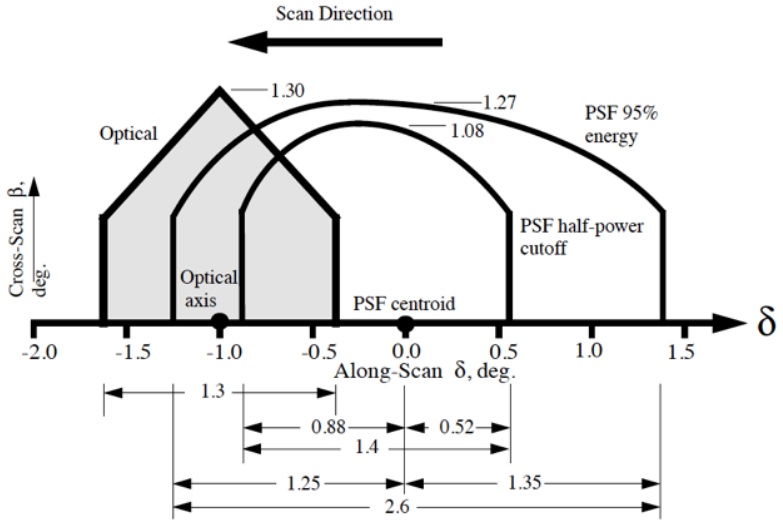

Figure B6 CERES field-of-view.

B.3.4 Radiance-to-Flux Conversion

As a scanning radiometer, CERES measures radiances whereas it is radiative fluxes that are needed for scientific investigations. The radiance-to-flux conversion is produced using empirical ADMs. For a given scene type, an instantaneous flux is inferred from an unfiltered radiance as follows:

$$F(\theta_0) = \frac{\pi I(\theta_0,\theta,\phi)}{R_j(\theta_0,\theta,\phi)} \tag{B2}$$

where F is the flux, I is the unfiltered radiance, θ_0 is the solar zenith angle, θ is the viewing zenith angle, and ϕ is the relative azimuth angle between the satellite and solar plane, R_j is the anisotropic factor for scene type j. R provides a measure of how much a given scene type deviates from an isotropic surface (R=1) in a particular viewing geometry. A commonly used approach for constructing ADMs is the so-called sorting-into-angular bins method (Suttles et al., 1988), whereby measured radiances are sorted and averaged into discrete angular bins for individual scene types. Ideally, the ADMs are constructed using multiple years of observations acquired over a wide range of viewing geometries. The mean radiances ($\hat{I}$) are then integrated over the upwelling hemisphere to produce a mean ADM flux ($\hat{F}$). The anisotropic factors (R) for scene type j are then calculated as:

$$R_j(\theta_0,\theta,\phi) = \frac{\pi \hat{I}_j(\theta_0,\theta,\phi)}{\int_0^{2\pi}\int_0^{\pi/2} \hat{I}_j(\theta_0,\theta,\phi) cos\theta sin\theta d\theta d\phi} = \frac{\pi \hat{I}_j(\theta_0,\theta,\phi)}{\hat{F}_j(\theta_0,\theta,\phi)}. \tag{B3}$$

Prior to CERES, ADMs were developed for the ERBE for 12 scene types (Suttles et al., 1988; Smith et al., 1986) determined using the maximum likelihood estimation (MLE) technique applied to observed SW and LW radiances (Wielicki and Green, 1989). Following the launch of CERES on TRMM, new ADMs were developed for hundreds of scene types with much improved angular resolution (Loeb et al., 2003). This is accomplished by using the CERES RAP mode. Another major advance is in scene identification—the CERES ADMs are based upon coincident imager retrievals for scene information within CERES footprints. The variables used to define CERES ADM scene types are selected based upon their influence on anisotropy. They include cloud fraction, cloud optical depth, cloud phase, cloud effective temperature, wind speed, surface type, snow and ice coverage, sea ice brightness, etc. CERES TRMM ADMs were developed using 9 months of CERES and VIRS data. This set of ADMs represents a much improved anisotropy characterization compared to those used during ERBE. Loeb et al. (2005) developed ADMs for CERES instruments on Terra and Aqua using cloud properties retrieved from MODIS for scene identification (Minnis et al., 2011). More recently, Su et al. (2015a) updated and improved upon these based upon lessons learned from extensive validation efforts. The Su et al. (2015a) ADMs rely on an updated cloud algorithm for scene identification (Edition 4). In addition to using the sorting-into-angular bins method for developing ADMs, the CERES Terra and Aqua ADMs are also derived using analytical functions when appropriate to characterize the anisotropy over some scene types. SW anisotropy is a strong function of θ_0, θ, and ϕ, and therefore the SW ADMs are developed as a function of all these three variables. The LW/WN anisotropy is generally a weak function of θ_0 and ϕ, and thus LW/WN ADMs are developed only as a function of θ. One exception is over clear land where shadowing by vegetation and rough terrain produces a heterogeneous

distribution of surface temperatures, resulting in a stronger dependence on ϕ compared to flat surfaces (Minnis et al., 2004).

Figures B7a-b show anisotropic factors as a function of viewing zenith angle for liquid water clouds with three ln($f\tau$) values and for different cloud phases with ln($f\tau$)=6 (f is the percentage cloud fraction and τ is the cloud optical depth). Here, θ_0=44-46° and ϕ corresponds to the principal plane (forward and back scatting directions correspond to positive and negative viewing zenith angle values, respectively). Anisotropic factors are highly sensitive to ln($f\tau$) within approximately 20° of nadir and at the oblique viewing zenith angles, particularly in the forward scattering direction (Figure B7a). The liquid and mixed clouds exhibit well-defined peaks in anisotropy due to cloud glory and rainbow features, while ice clouds exhibit peaks in anisotropy in the specular reflectance direction (Figure B7b). For cloudy scenes with ln($f\tau$)=6, R is about 0.8 for nadir viewing geometry, so by assuming these clouds are isotropic would result in a 20% underestimation in SW flux. Similarly, for an oblique viewing geometry (θ=63°), R is about 1.5. Here the isotropic assumption would lead to a 50% overestimation in SW flux. Figure B8 shows an example of LW anisotropic factors over cloudy ocean for thick (solid line) and thin (dashed line) clouds. The LW anisotropic factors decrease as the viewing zenith angle increases, often referred to as limb darkening. LW anisotropy is more pronounced for thinner clouds because the contribution from the warm ocean surface transmitted through the cloud at nadir is attenuated rapidly with viewing zenith angle. Thicker clouds are opaque to radiation from the surface at all viewing zenith angles. When the cloud-top is in the upper troposphere, there is relatively little attenuation, resulting in a more isotropic ADM.

These examples clearly show that Earth scenes are far from isotropic and without accurate quantification of the unique anisotropic characteristics of each scene type, large errors in the Earth's radiation budget will occur. Figures B9a and B9c show the annual mean TOA SW and LW fluxes derived using the CERES ADMs, respectively, together with the corresponding differences obtained when one assumes the scenes are isotropic (Figure B9b and B9d). The annual mean CERES SW flux is 98.9 Wm^{-2}. If we use the isotropic assumption, it reduces to 94.8 Wm^{-2}. Regionally, reductions of up to 20 Wm^{-2} over the polar region and slight increases over the tropical land regions are observed. For LW flux, the annual mean increases from 238.9 Wm^{-2} to 241.5 Wm^{-2} if we use the isotropic assumption. The LW difference is more uniform compared to SW, with the largest positive bias occurring in the Saharan desert. The meridional stripes seen in the LW difference plot are related to the large viewing zenith angles at the edge of the cross track swaths.

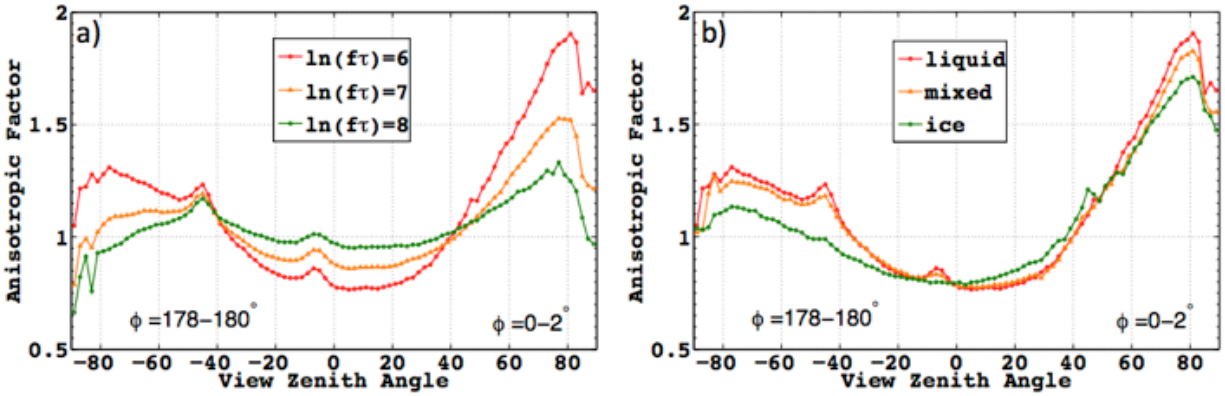

Figure B7 CERES SW anisotropic factors over ocean in the principle plane for a) liquid clouds with different ln(fτ) values, b) clouds of different phases with ln(fτ)=6. Anisotropic factors are derived for θ_0=44-46°.

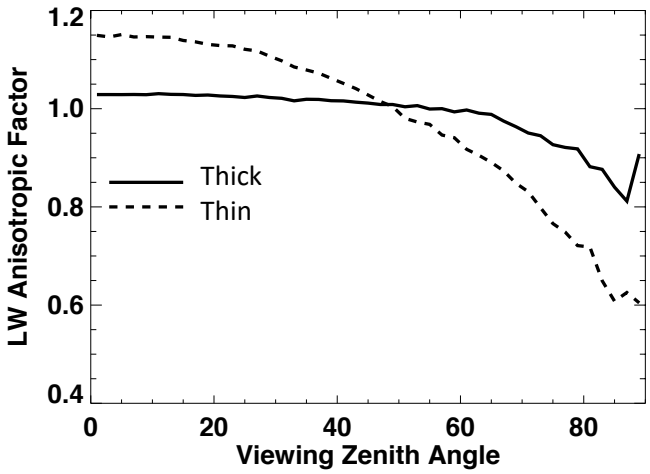

Figure B8 CERES LW anisotropic factors over ocean for thick clouds (solid line) and thin clouds (thin line) under overcast conditions.

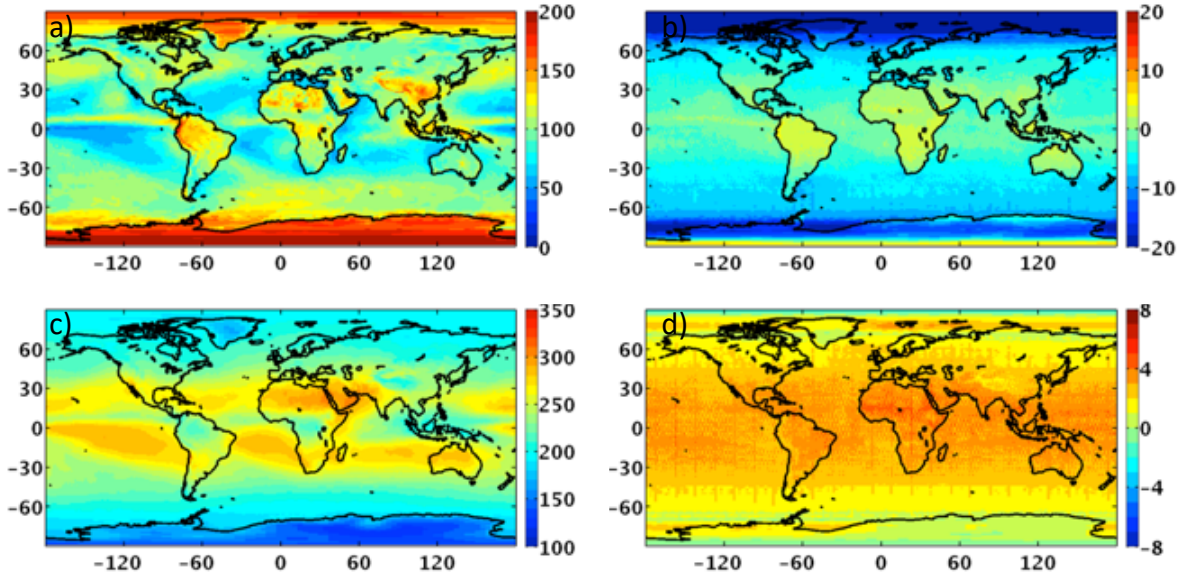

Figure B9 Annual mean TOA SW flux derived using CERES ADMs (a), annual mean difference between SW flux derived assuming isotropic surfaces and using CERES ADMs (b), (c) and (d) are the same as (a) and (b) but for TOA LW flux.

B.4 Temporally and Spatially Averaged CERES Data Products

While CERES instruments aboard Terra, Aqua, SNPP and NOAA-20 provide global coverage daily, they do so from a sun-synchronous, near-polar, circular orbit. Consequently, if one were to simply globally average the instantaneous SW and LW TOA fluxes, the average would be incorrect. In that case, Polar regions would receive too much weight in the average relative to their areal coverage, and radiative flux changes between CERES observation times would go unaccounted for. To overcome this problem, the CERES TOA fluxes undergo a series of steps to produce spatially gridded and time interpolated TOA fluxes (Figure 2.3). CERES instantaneous TOA fluxes and imager cloud properties from the SSF product are first averaged onto a uniform

nested 1° equal-area grid and sorted and averaged into hour boxes. These gridded instantaneous properties are provided in the SSF1deg-Hour product. To determine radiative fluxes in hour boxes in which there are no CERES observations, two separate time-interpolation approaches are used in CERES processing system. The SSF1deg and SYN1deg time-interpolation approaches are briefly discussed in the following subsections and a more in-depth description is in Doelling et al. (2013). After the radiative fluxes have been gridded and time-interpolated, global averages can be computed that have the correct temporal and spatial weighting.

B.4.1 SSF1deg Stream

Time interpolation for the SSF Stream (Figure 2.3) assumes scene properties between CERES observations times remain invariant throughout the day. SW TOA fluxes are determined by accounting for albedo changes with solar zenith angle using scene dependent empirical diurnal models of albedo, or "albedo directional models". The albedo directional models corresponding to the scenes within a given gridbox at the CERES observation time are used together with the observed albedos to determine TOA fluxes during other times of the day or until the next CERES observation time. The CERES directional models are based upon CERES TRMM ADMs for non-polar regions (Loeb et al., 2003) and CERES Terra ADMs for polar regions (Su et al., 2015a). Figure B10 shows examples of CERES TRMM albedo directional models for overcast liquid water clouds over ocean. As the clouds become thicker, the directional model becomes progressively flatter, implying a more Lambertian albedo dependence on solar zenith angle. The mean directional model for a given gridbox on a given day is determined from imager scene information within CERES footprints that fall within the gridbox. Albedos in other hour boxes are computed as follows:

$$\alpha(t_i) = \frac{\bar{\alpha}(t_i)}{\bar{\alpha}(t_o)}\alpha(t_o) \tag{B4}$$

where $\alpha(t_i)$ is the estimated albedo in hour box t_i, $\alpha(t_o)$ is the observed albedo at the CERES observation time, and $\bar{\alpha}(t_i)$ and $\bar{\alpha}(t_o)$ are the albedo directional models at t_i and t_o, respectively. The SW TOA flux at t_i is determined from:

$$F(t_i) = \alpha(t_i) S_o \cos(\theta_{oi}) \left({R_{se}}/{R}\right)^2 \tag{B5}$$

where S_o is the instantaneous TOA solar irradiance at mean sun-Earth distance, θ_{oi} is the solar zenith angle at t_i, R_{se} is the mean sun-Earth distance, and R is the actual sun-Earth distance on the day of the observation. In CERES processing, S_o varies daily according to observations from the Solar Radiation and Climate Experiment (SORCE) mission (Kopp and Rottman, 2005). The daily mean TOA SW flux is determined by averaging $F(t_i)$ over all hourboxes during the day (including nighttime hours where the SW flux is zero).

The LW TOA fluxes in the SSF Stream are determined using a half-sine fit over land, with a peak at local solar noon and using a constant nightly flux, and linear interpolation over ocean and snow surfaces (Young et al., 1998). This methodology of time interpolation is referred to as the CERES-only (CO) temporal interpolation method in Doelling et al. (2013). This approach is similar to what was used in the ERBE temporal averaging algorithm (Young et al., 1998).

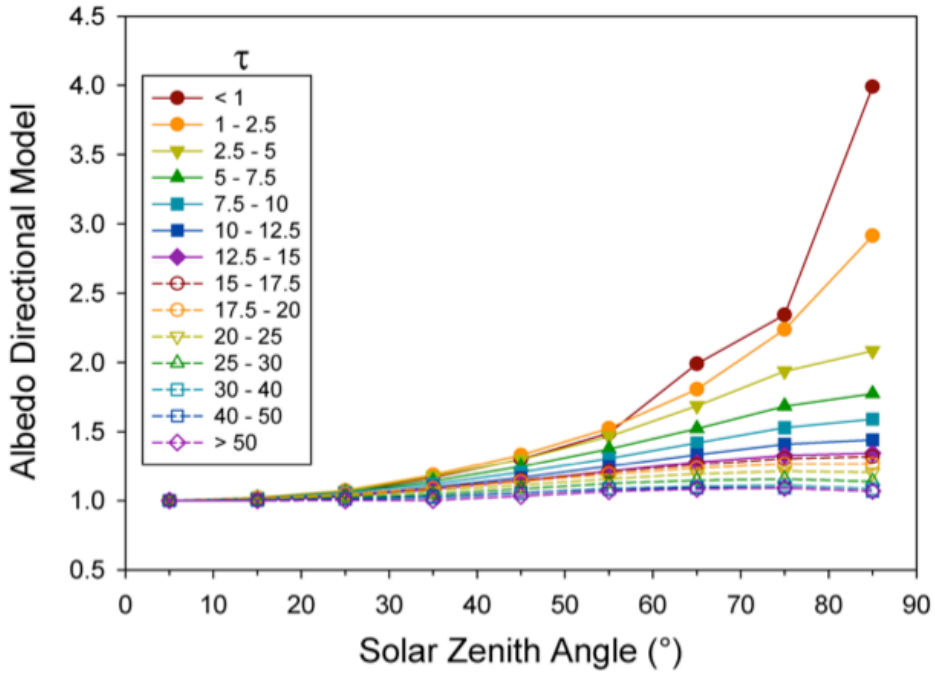

Figure B10 CERES albedo directional models (diurnal albedo normalized to overhead sun) for overcast liquid water clouds over ocean as a function of cloud optical depth (τ).

B.4.2 SYN1deg Stream

In the SYN1deg stream, five geostationary (GEO) imagers covering all longitudes between 60°S and 60°N are used to enable explicit regional estimates of TOA fluxes between CERES observation times. In order for the GEO data to be used for this purpose, they undergo a number of processing steps (Figure B11). GEO images are first screened for artifacts (e.g., bad scan lines) using both automated techniques and visual inspection. Next, the GEO visible radiances are intercalibrated against imager radiances at 0.65 μm. This involves generating linear regressions of coincident ray-matched imager and GEO radiances within 0.5°×0.5° latitude-longitude regions each month and using the regression slopes to adjust the GEO radiances. Next, a cloud retrieval algorithm is used to infer cloud properties from the GEO radiances. The cloud retrieval algorithm applied depends on the available channels. For GEO imagers having no channel at ~3.8 μm, a two channel method (Minnis et al., 1995) is used. Otherwise, the algorithm is similar to that used by the CERES to analyze MODIS and VIIRS (Minnis et al., 2011; Minnis et al., 2008). Next, the GEO narrowband radiances averaged over 1°×1° latitude-longitude regions are converted to broadband radiative fluxes using empirical narrow-to-broadband radiance and radiance-to-flux algorithms. Finally, the GEO broadband flux estimates are normalized on a region-by-region basis using coincident CERES TOA fluxes. This mitigates against GEO artifacts and anchors the GEO derived broadband fluxes to CERES. Using this approach, CERES SYN1deg products incorporate 3-hourly GEO derived fluxes and are produced at 3-hourly, daily and monthly timescales. We note that Edition 4 uses 1-hourly GEO data to produce 1-hourly, 3-hourly, daily and monthly output.

Figure B11 Flowchart of steps used to produce the CERES SYN1deg product.

B.5 Validation

The CERES SSF1deg product provides global coverage daily with excellent calibration stability (Loeb et al., 2012a), but samples only specific times of the day because it relies on CERES data, which are restricted to sun-synchronous satellite orbits. Consequently, regional mean TOA fluxes will be in error over areas with strong diurnal cycles. This is illustrated in Figure B12, which shows annual mean differences in SW TOA flux between CERES Terra SSF1deg and combined CERES Terra-Aqua SYN1deg for the year 2002. In marine stratocumulus regions off the west coasts of North and South America and Africa, SW TOA fluxes from CERES Terra SSF1deg are too high because cloud cover is greater in the morning, when CERES Terra observes these regions. Similarly, SW TOA fluxes from CERES Terra SSF1deg are too low in land convective regions such as South America and central Africa because land convection typically peaks in the afternoon. By combining the CERES Terra, Aqua and GEO products, SYN1deg provides a far more complete

representation of the diurnal cycle compared to SSF1deg, and therefore a more accurate representation of the regional distribution of SW TOA flux. This is further confirmed through comparisons between CERES SYN1deg and observations from the Geostationary Earth Radiation Budget (GERB) instrument (Harries et al., 2005), which provides broadband radiative fluxes between 60°S-60°N centered above the equator at 0° longitude with a time resolution of 15 min. Doelling et al. (2013) show excellent agreement between CERES SYN1deg and GERB TOA fluxes over a range of cloud conditions.

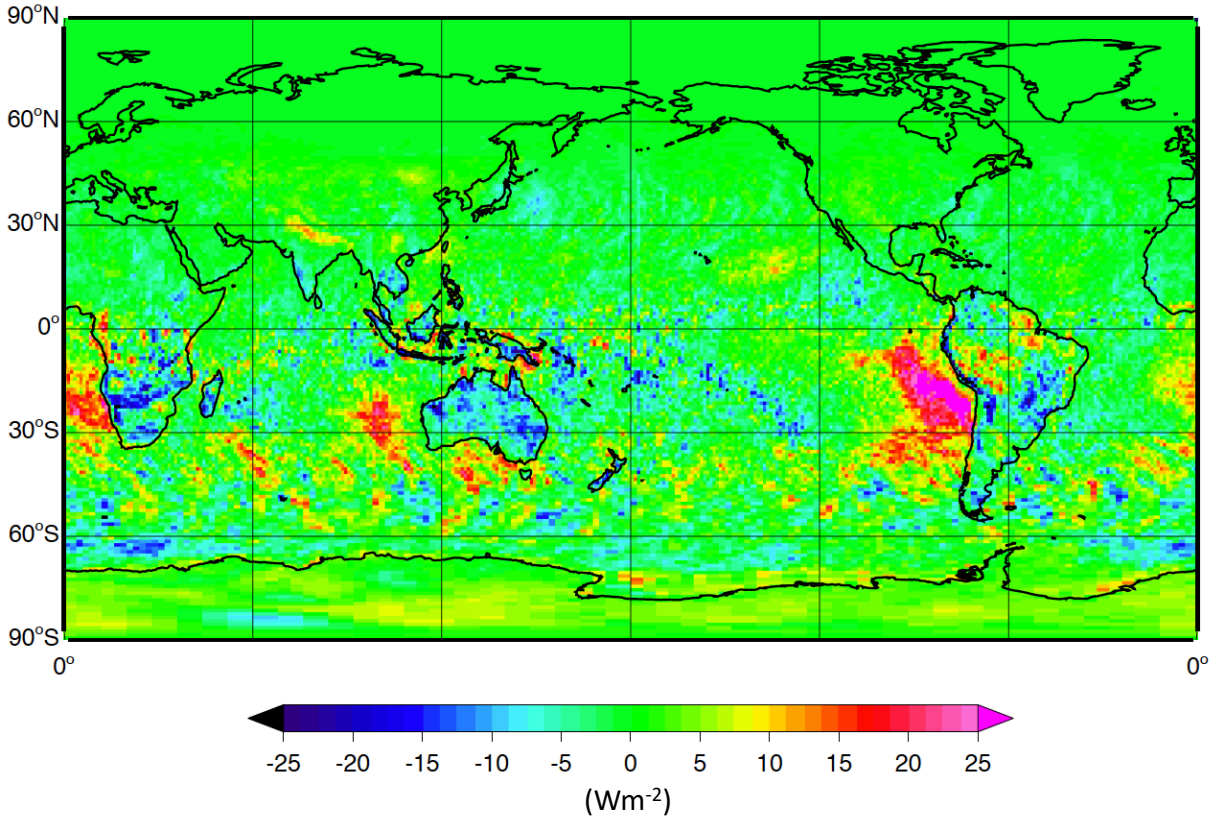

Figure B12 SW TOA flux difference between SSF1deg-Terra and SYN1deg Ed3a for January 2010.

However, because GEO data are used in SYN1deg, artifacts in the GEO derived fluxes over certain regions and time periods can cause discontinuities in the CERES record. This is especially true in the early part of the CERES record. While the CERES team attempts to remove most of the GEO derived flux biases by normalizing the fluxes with CERES at Terra or Aqua observation times, spurious jumps in the SW TOA flux can still occur when GEO satellites are replaced. Discontinuities can arise due to changes in: satellite position along the equator, calibration and/or visible sensor spectral response, and imaging schedules. Such artifacts in the GEO data can be problematic in studies of TOA radiation interannual variability and/or trends. As an example, Figure B13a-b show regional trends in SW TOA flux for CERES SSF1deg-Month Ed3A and SYN1deg-Month Ed3A, respectively, for March 2000–February 2010. While the trend patterns are similar, vertical lines corresponding to geostationary satellite boundaries are clearly visible in Figure B13b near 30°E, 100°E, 180°E, 105°W, and 40°W. The geostationary artifacts are more pronounced over Africa and Asia, but also show up to the east of South America. Similarly, Figure B14a-b show SW TOA flux anomalies for CERES SYN1deg-Month and SSF1deg-Month Ed3A between 60°S-60°N and 110°E-180°E. While the SW TOA flux anomalies

appear to track one another closely (Figure B14a), their difference reveals large discontinuities, particularly when Multi-functional Transport Satellite (MTSAT)-1R replaces Geostationary Operational Environmental Satellite (GOES)-9 in November 2005. A slight blurring effect was observed for the MTSAT-1R imager visible channel, which was mitigated using a pixel PSF correction algorithm (Doelling et al., 2015; Khlopenkov et al., 2015). The correction was included in the SYN1deg Ed4A products. Thus, by incorporating additional information from geostationary satellite instruments, the CERES SYN1deg data product provides a better representation of the regional distribution of SW TOA flux, but because of GEO artifacts early in the CERES record, spurious jumps are observed when interannual variations are compared with SSF1deg.

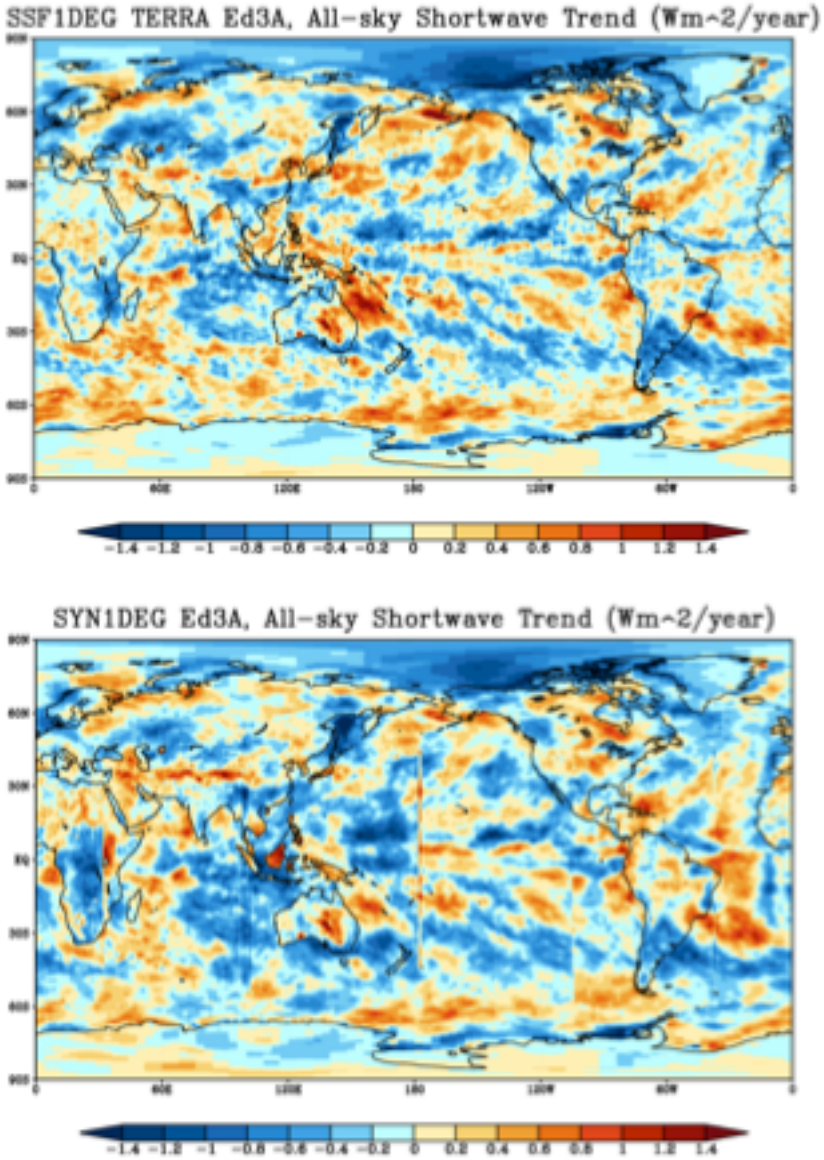

Figure B13 Regional trends in SW TOA flux (Wm^{-2} per year) for March 2000-February 2010 from (a) SSF1deg Ed3A and (b) SYN1deg Ed3A.

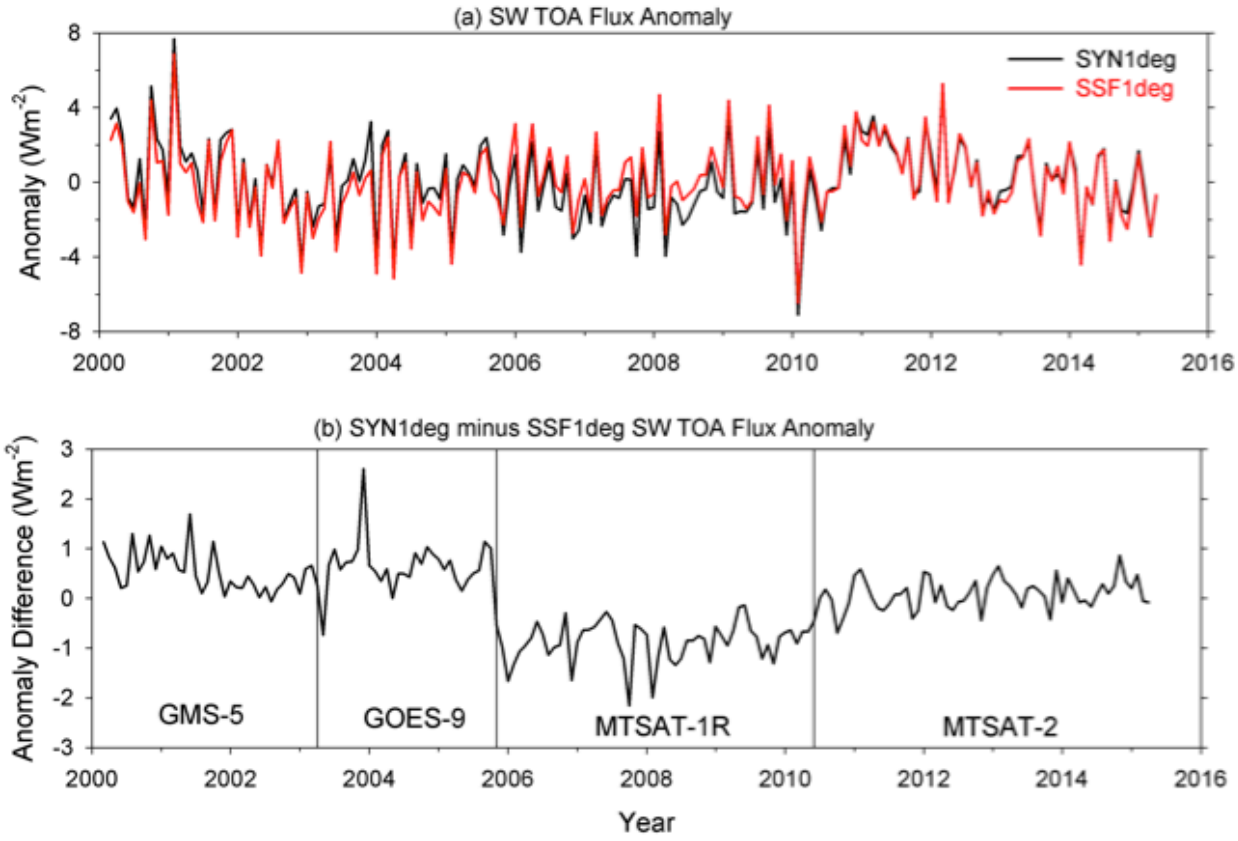

Figure B14 (a) SW TOA flux anomalies for 60°S-60°N and 110°E-180°E between March 2000 and April 2015. (b) SW TOA flux anomaly difference between SYN1deg and SSF1deg. The CERES data product version is Edition 3.

B.6 TOA Energy Balanced and Filled Product (EBAF-TOA)

Despite recent improvements in satellite instrument calibration and the algorithms used to determine CERES SW and LW outgoing TOA radiative fluxes, a sizeable imbalance still persists in the average global net radiation at the TOA (or EEI). For example, using the most recent CERES Edition 4 Instrument calibration improvements, the SYN1deg_Edition4 net TOA flux imbalance is ≈4 W m^{-2}, much larger than the expected mean range of ≈0.5-1.0 Wm^{-2} (von Schuckmann et al., 2016). Constraining the absolute value of EEI from satellite measurements is extremely challenging. EEI is a small residual of incoming and outgoing TOA fluxes that are two orders-of-magnitude larger. Achieving a 50% uncertainty in EEI would require the total outgoing radiation (SW plus LW TOA fluxes) to be known to 0.2 Wm^{-2} or 0.06%, roughly an order-of-magnitude more accurate than present-day ERB sensors. The bias in EEI from CERES is problematic in applications that use ERB data for climate model evaluation, estimations of the Earth's annual global mean energy budget, and studies that infer meridional heat transports. Another limitation problematic for studies requiring clear-sky TOA fluxes is the presence of data gaps in monthly mean clear-sky TOA flux maps owing to a lack of cloud-free CERES footprints within 1°x1° regions as identified by imager data. This occurs frequently over the Southern Oceans, North Atlantic Ocean, and Amazon region (Loeb et al., 2009a). A third issue, noted in the previous section, is that while the SYN1deg and SSF1deg data products are useful either for providing a good representation of regional mean TOA fluxes or for tracking interannual variations, neither is well suited to address both items.

The goal of CERES EBAF product is to provide clear and all-sky monthly mean TOA fluxes on a 1°x1° latitude-by-longitude equal-area grid that has a net TOA flux imbalance that is consistent with our best estimate based upon in-situ ocean heat content measurements, provides monthly clear-sky TOA fluxes in all regions, and provides a good representation of the regional mean TOA flux distribution while at the same time ensuring that spurious jumps from GEO artifacts do not impact TOA flux interannual variations. In the following subsections, we briefly discuss how each of these three items is addressed in the CERES EBAF data product.

B.6.1 Global TOA Net Imbalance

Currently, the most accurate method of determining the EEI is by estimating the rate of change of energy storage in the climate system (Hansen et al., 2011; Trenberth et al., 2014; Church et al., 2011). Approximately 93% of the excess energy in the climate system ends up being stored in the ocean (Bindoff et al., 2013), the remainder is associated with changes in ice, land, and the atmosphere. Thus, EEI can be inferred from in-situ based observations of ocean heating rate obtained from floats measuring vertical temperature profiles in the ocean and estimates of smaller contributions in the atmosphere, land and cryosphere. The most complete in-situ ocean measurements for this purpose is from the Argo network (Gould et al., 2004), which consists of over 3,500 floats sampling temperature and salinity to a depth of 1,800 m. Despite the large number of Argo floats, sampling errors still limit reliable estimates of EEI for time scales of less than 5 years. Loeb et al. (2012b) used 5 years of Argo data between July 2005 and June 2010 together with estimates of other energy storage in the system to determine the EEI to be 0.58 ± 0.38 Wm^{-2}. More recently, Johnson et al. (2016) updated that analysis with 10 years of Argo data for July 2005-June 2015 and obtained an EEI of 0.71 ± 0.1 Wm^{-2}. An objective constrainment algorithm is used to make a one-time adjustment to SW and LW TOA fluxes within their ranges of uncertainty in order to anchor the CERES net TOA flux time-series to the Argo-based estimate of EEI (Loeb et al., 2009a, 2018a). The combination of CERES and Argo provides an optimal way of capitalizing on the strengths of satellite and in-situ measurements, as the CERES data provide the spatial coverage and radiometric stability required to resolve higher temporal variations in EEI (e.g., interannual), and Argo in-situ data enables a more accurate absolute value of EEI.

B.6.2 Clear-Sky TOA Fluxes

In order to significantly reduce the problem of data gaps in monthly mean clear-sky TOA flux maps due to a lack of completely cloud-free CERES footprints within 1°x1° regions, EBAF gridbox mean clear-sky fluxes are determined using an area-weighted average of CERES broadband fluxes from completely cloud-free footprints and imager-derived ‘‘broadband’’ clear-sky fluxes estimated from the cloud-free portions of CERES footprints with <95% cloud cover. In both cases, clear regions are identified using the CERES team’s cloud mask applied to imager pixel data (Minnis et al., 2008; Trepte et al., 2002; Trepte et al., 2018). Clear-sky fluxes in partly cloudy CERES footprints are derived using imager–CERES narrow-to-broadband regressions to convert the imager narrowband radiances over the clear portions of a footprint to broadband SW radiances. The imager-based “broadband” radiances are converted to radiative fluxes using CERES ADMs (Section B.3.4). A more detailed description of the procedure for inferring clear-sky TOA fluxes in EBAF is provided in Loeb et al. (2009a; 2018a).

B.6.3 Temporal Interpolation

(i) SW TOA Flux

To maintain the excellent CERES instrument calibration stability of SSF1deg and also preserve diurnal information in SYN1deg, EBAF uses a new approach to convert daily regional mean SSF1deg fluxes to diurnally complete values analogous to SYN1deg, but without

geostationary artifacts. The idea is to apply pre-determined empirical diurnal correction ratios (DCRs) to daily regional mean SSF1deg SW fluxes, which are then averaged to produce monthly SW TOA fluxes. The DCRs consist of SYN1deg-to-SSF1deg flux ratios derived using daily mean SW TOA fluxes between July 2002 and June 2015. The DCRs are defined according to calendar month, surface type, latitude, and a daily Diurnal Asymmetry Ratio (DAR), defined by the morning-minus-afternoon GEO-derived SW flux normalized by the 24-h average (see Loeb et al., 2018a for details). For March 2000-June 2002, TOA fluxes are based upon CERES observations from the Terra spacecraft, while for July 2002 onwards, CERES observations from both Terra and Aqua are utilized in order to improve the accuracy of the diurnal corrections. The diurnal corrections applied to SSF1deg fluxes dramatically improve the EBAF record by minimizing the impact of geostationary satellite artifacts, especially with respect to temporal regional trends.

The uncertainty in 1°x1° regional SW TOA flux is evaluated separately for 03/2000-06/2002 (Terra-Only period) and for 07/2002-12/2010 (Terra-Aqua period). To determine uncertainties for the Terra-Only period, we use data from the Terra-Aqua period and compare regional fluxes derived by applying diurnal corrections to the Terra SSF1deg product with regional fluxes determined by averaging fluxes from the Terra and Aqua SYN1deg data products. The SYN1deg products combine CERES observations on Terra or Aqua with five geostationary instruments covering all longitudes between 60°S and 60°N, thus providing the most temporally and spatially complete CERES dataset for Terra or Aqua. For 03/2000-06/2002 (Terra-Only period), the overall regional root-mean-square (RMS) error is 4 Wm^{-2}. Uncertainties for months when both Terra and Aqua are available (07/2002-12/2010) are determined by comparing regional fluxes derived by applying diurnal corrections to the average of Terra and Aqua SSF1deg fluxes with average Terra and Aqua regional fluxes from SYN1deg. In that case, the regional RMS error decreases to 2.7 Wm^{-2}. To place these results into context, the regional RMS difference between Terra and Aqua SYN1deg SW TOA fluxes is 4.4 Wm^{-2}.

(ii) LW TOA Flux

LW TOA fluxes in EBAF are derived directly from the Terra+Aqua CERES_SYN1deg data product for March 2000−December 2010. In contrast to the SW, geostationary instruments carry onboard calibration sources (blackbodies) to correct for instrument drift in the LW. Consequently, the trend from EBAF falls within 0.1 Wm^{-2} per decade of SSF1deg, which only relies on CERES.

B.7 Surface Energy Balanced and Filled Product (EBAF-SFC)

Surface radiative fluxes are determined from retrieved cloud and aerosol properties and temperature and humidity from reanalysis through 1D radiative transfer theory. In addition, they are constrained monthly and regionally using TOA fluxes from EBAF-TOA. When compared with surface observations at 46 buoys and 36 land sites (Kato et al. 2018), EBAF-SFC monthly mean downward fluxes are within 5 Wm^{-2} for SW, 2 Wm^{-2} for LW averaged over the ocean sites, and 1 Wm^{-2} for both SW and LW averaged over the land sites. In addition, the correlation coefficient between EBAF-SFC and surface-observed deseasonalized anomalies in monthly mean regional flux is better than 0.93 over ocean (see Figure B15) and 0.97 over land for both SW and LW. The standard deviation of computed minus observed monthly anomalies is < 0 .4 Wm^{-2} for LW while for SW it is < 0.7 Wm^{-2} over ocean and < 0.3 Wm^{-2} over land.

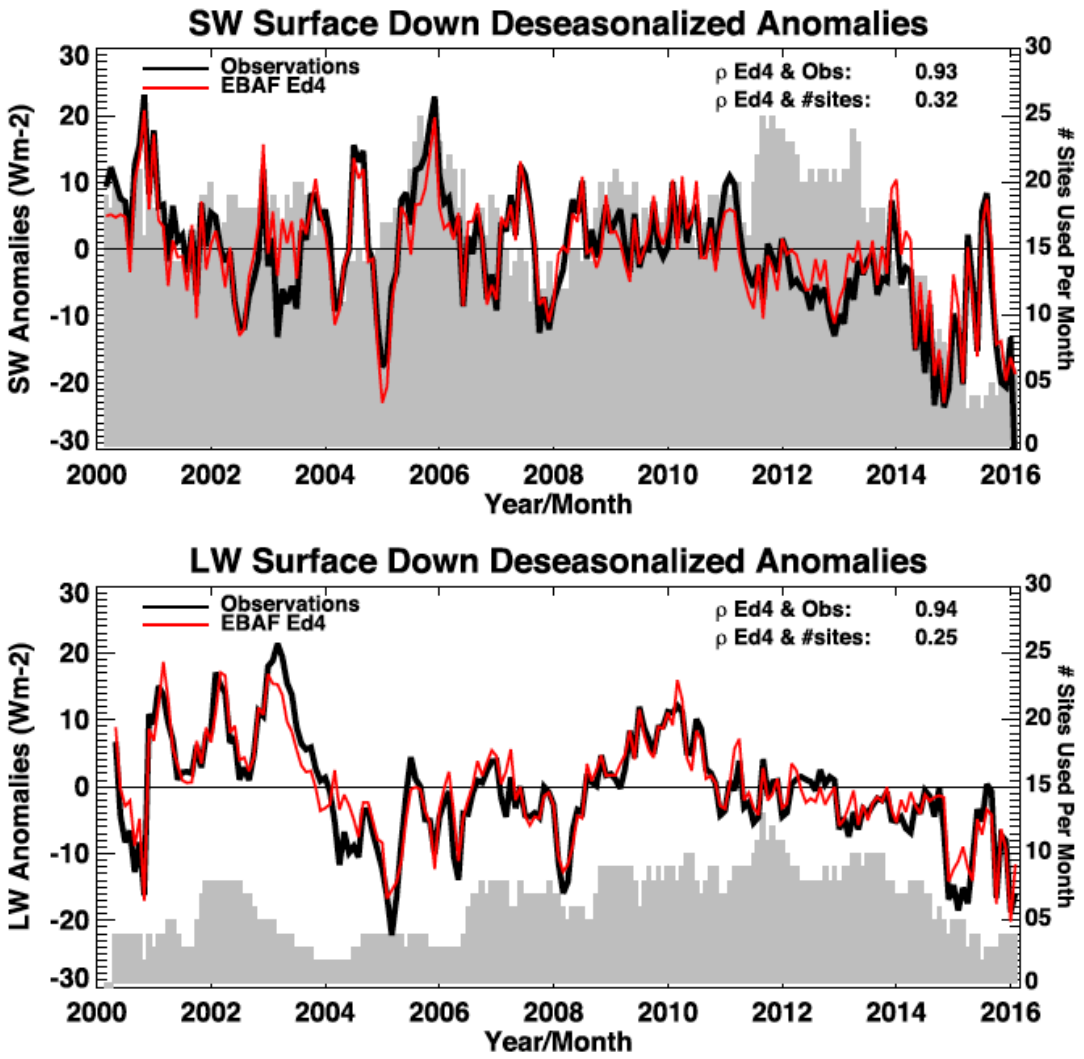

Figure B15 Monthly deseasonalized anomalies computed with downward (top) SW and (bottom) LW irradiances measured at 46 buoys (black lines). Red lines indicate deseasonalized anomalies computed with Ed4 EBAF using grid boxes containing the buoys. Numbers shown on the top-right corner are correlation coefficients between (top) computed and observed deseasonalized anomalies and between (bottom) computed anomalies and number of sites used for computing anomalies. Gray shading indicates the number of sites used to compute anomalies. (From Kato et al., 2018).

Appendix C Selected Highlights from Peer-Reviewed Journal Publications

C.1 Earth's Energy Budget

- Trenberth and Fasullo (2009) used CERES Terra, ocean heat content, and reanalysis data to provide a summary of the overall energy balance for the global atmosphere, ocean and land domains (*Figure C.5.4*). Of the 2.6 PW of net radiation into the system over ocean, approximately 0.4 PW are absorbed by the ocean, and 2.2 PW are transported from ocean to land by the atmosphere to compensate for the net radiation out of the system over land. Approximately 0.01 PW of the net flux imbalance goes into land and melting of ice.

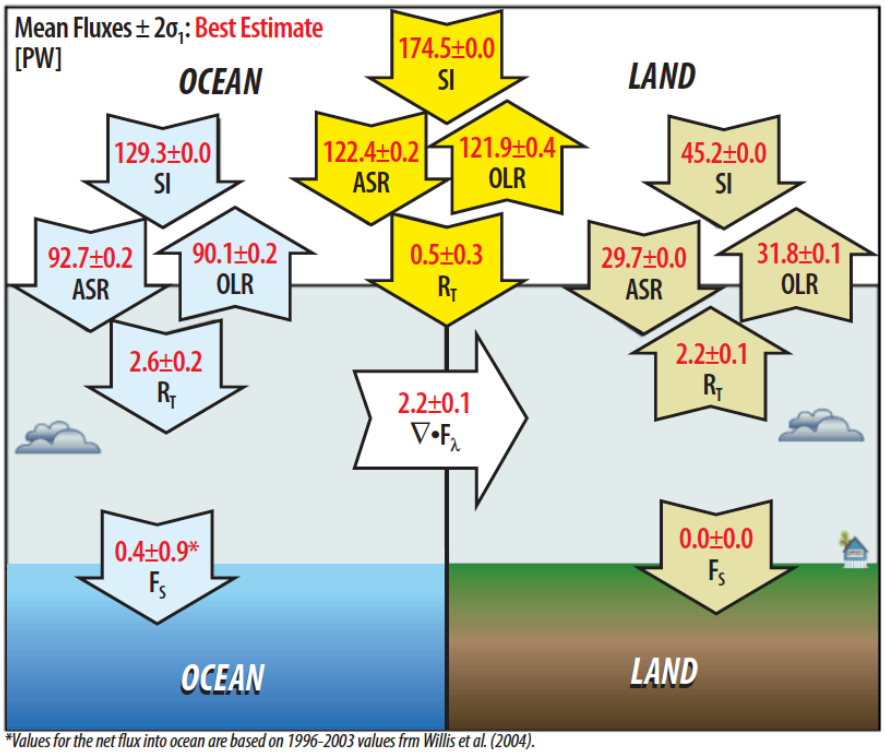

Figure C.5.4 March 2000 to May 2004 mean CERES TOA fluxes (PW) globally (center) and for global land (right) and global-ocean (left) regions. SI is the solar irradiance and the net downward irradiance RT=ASR-OLR. The arrows show the direction of the flow. The net surface flux (Fs) is also given along with the energy flow from ocean to land. From Trenberth and Fasullo, 2009).

- Trenberth and Fasullo (2017) combine CERES TOA radiation and atmospheric and ocean reanalyses to determine a new estimate of ocean heat transports for 2000 through 2013 throughout the Atlantic. Peak Atlantic northward ocean heat transports average 1.18 ± 0.13 PW (1 sigma) at 15°N but vary considerably in latitude and time. Results agree well with observational estimates at 26.5°N from the RAPID array, but for 2004-2013 the meridional heat transport is 1.00 ± 0.11 PW versus 1.23 ± 0.11 PW for RAPID. In addition, these results have no hint of a trend, unlike the RAPID results. Strong westerlies north of a meridian drive ocean currents and an ocean heat loss into the atmosphere that is exacerbated by a decrease in ocean heat transport northward.

- Using satellite records of cloud amount from imager radiances and all-sky albedo from CERES and ERBE spanning the 1980s through the 2000s, Norris et al. (2016) provide evidence of large-scale decadal cloud pattern changes that correlate well with those produced by model simulations of climate with recent historical external radiative forcing. Both cloud amounts and all-sky albedos exhibit significant decreases at mid-latitudes around 40°S and 40°N and increases in the northern tropics. The observed and simulated cloud amount and albedo pattern changes are consistent with a poleward retreat of mid-latitude storm tracks and expansion of the subtropical dry zones. The study highlights the need for maintaining stable observational records over multiple decades.

- Loeb et al. (2015) use CERES TOA and surface radiation data, ERA-Interim divergence of total atmospheric energy transport, and GPCP precipitation observations to evaluate how climate models represent linkages between hemispheric asymmetries in atmospheric and oceanic energy budgets, tropical precipitation and the mean position of the ITCZ. Climate models with greater SH than NH tropical precipitation overestimate the SH-NH asymmetry in net downward surface radiation compared to CERES, and overestimate heating of the SH atmosphere. This results in anomalous SH to NH cross-equatorial heat transport via the upper branch of the northern Hadley Cell and anomalous transport of moisture from the NH to SH via the lower branch, which supplies moisture to a SH ITCZ.

- Hartmann and Ceppi (2014) analyze trends in CERES SW observations from March 2000–February 2013 over the Arctic. The trend in Arctic ice is clearly evident in the time series of reflected shortwave radiation, which closely follows the record of ice extent (*Figure C.5.5*). The data indicate that, for every 10^6 km^2 decrease in September sea ice extent, annual-mean absorbed solar radiation averaged over 75°–90°N increases by 2.5 Wm^2, or about 6 Wm^2 between 2000 and 2012. CMIP5 models generally show a much smaller change in sea ice extent over the 1970–2012 period, but the relationship of sea ice extent to reflected shortwave is in good agreement with recent observations.

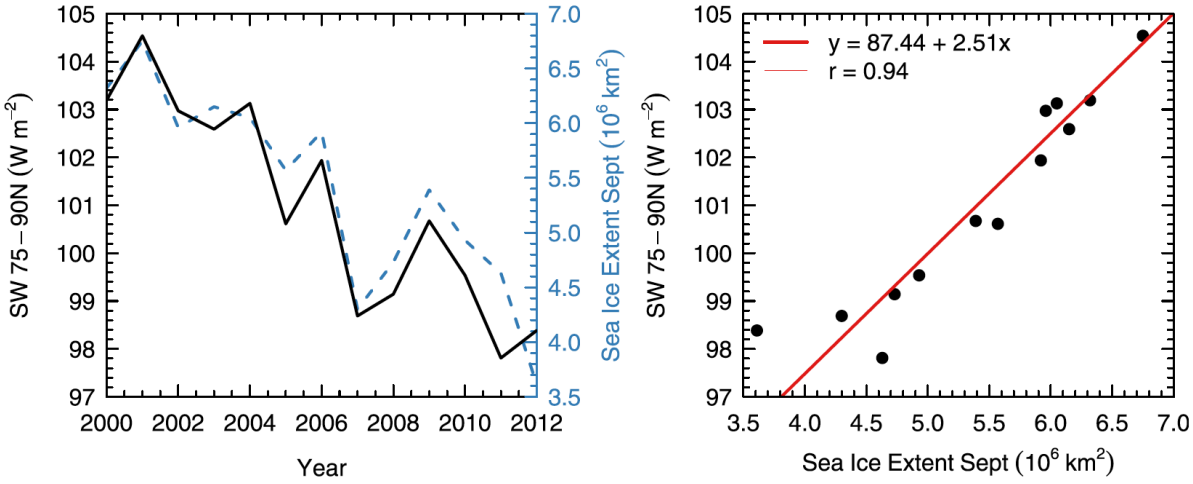

Figure C.5.5 (left) Annual-mean CERES reflected shortwave area averaged from 75° to 90° N for each (March–February average) vs the sea ice extent in September of the same year. (right) Scatterplot of annual-mean CERES shortwave reflected averaged over the area poleward of 75° N vs Arctic sea ice extent in September for 2000–12. (From Hartmann and Ceppi, 2014).

- DeAngelis et al. (2015) use SW flux absorbed in the atmosphere computed from EBAF-TOA and EBAF-SFC to determine the error in atmospheric energy balance and precipitation change predicted by climate models. Using an ensemble of climate models, they show that models that underestimate the increase in shortwave atmospheric absorption associated with increasing water vapor generally overestimate the increase in precipitation.

- Using an atmospheric and surface energy budget closure framework, CERES data products are used to: assess precipitation biases in climate models (Levine and Boos 2017), understand shifts in the latitude of the intertropical convergence zone (Boos and Korty 2016), and diagnose changes in soil moisture and pH balance (Slessarev et al. 2016).

- CERES observations are used together with reanalysis data to determine new estimates of large-scale Arctic atmospheric energy budget (Porter et al., 2010). The convergence of total transport is determined from the residual of net surface flux and time change in atmospheric energy storage using CERES TOA radiation and reanalysis data. This approach yields results that are more physical compared to estimates derived from mass-corrected flux values from reanalysis data alone. Monthly mean anomalies of budget terms are used to examine conditions leading to the extreme seasonal sea ice extent minimum of September 2005 and the role of the ice albedo feedback process.

- Using a decade of CERES observations Voigt et al. (2012) show that while the Northern hemisphere reflects more solar radiation than the Southern hemisphere under cloud-free conditions owing to the asymmetric distribution of continents and aerosols between the hemispheres, the Earth exhibits near-perfect symmetry in planetary albedo between the hemispheres for all-sky conditions. This is a unique property of Earth, as most partitions of Earth into random halfs do not exhibit hemispheric symmetry. The results motivate further research on the possible mechanisms that lead to hemispheric symmetry in planetary albedo.

- Synergistic use of observations from CERES, MODIS, CALIPSO and Cloudsat has led to a major revision of our understanding of the Earth's energy budget (Stephens et al., 2012; Kato et al., 2011; Wild, 2012), particularly at the surface, which controls evaporation at the surface and thus global precipitation response to climate forcing (Figure C.5.6).

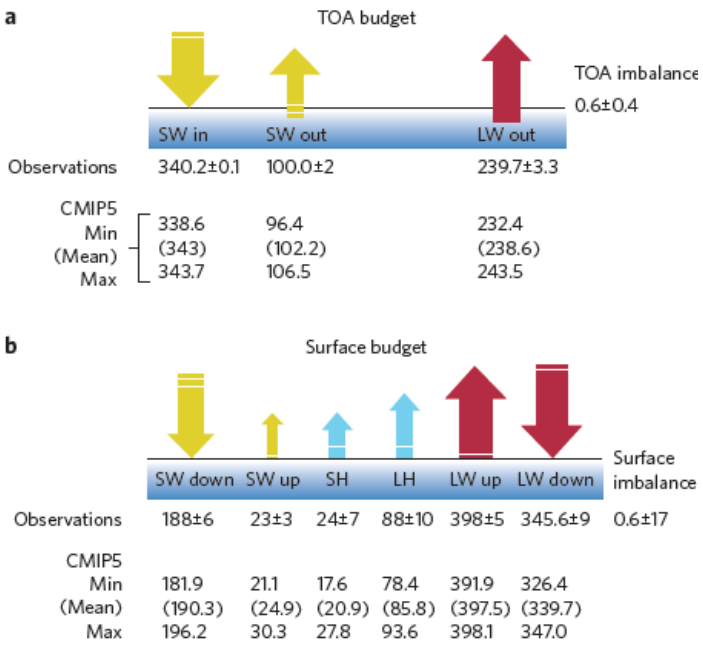

Figure C.5.6 Observed and CMIP5 climate model deduced energy fluxes (all in Wm^{-2}) at the (a) TOA and (b) surface. (From Stephens et al., 2012)

C.2 Cloud Processes and Feedbacks

- Dessler 2013 compares CERES-derived regional cloud feedbacks with those from two climate model ensembles, one dominated by internal variability (the control ensemble) and the other dominated by long-term global warming (the A1B ensemble) (*Figure C.5.7*). There are general similarities between the total cloud feedback in the observations and the control ensemble but almost all of the control runs predict a positive total cloud feedback in the tropical Pacific, which is inconsistent with the observations. For the A1B ensemble, the total cloud feedback is spatially more uniform than the total cloud feedback in response to ENSO.

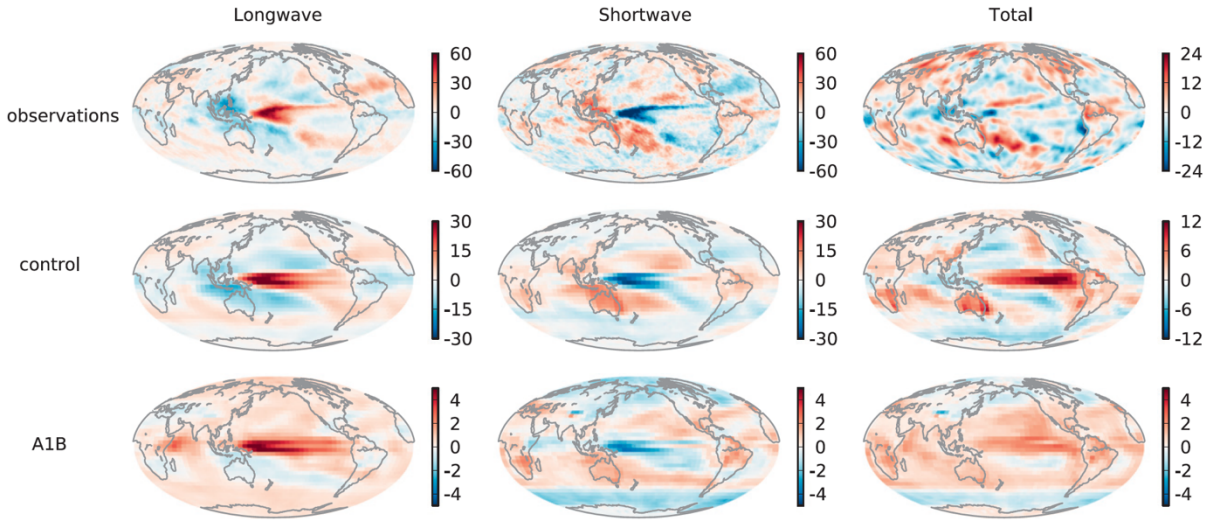

Figure C.5.7 (left) LW cloud feedback, (middle) shortwave cloud feedback, and (right) net cloud feedbacks, for (top) CERES, (middle) the control ensemble, and (bottom) the A1B ensemble. In all panels, the units are $W\ m^{-2}\ K^{-1}$. Note that the color scale varies among the panels. (From Dessler, 2013).

- CERES data products have enabled new insights on climate feedback and climate sensitivity. Brient and Schneider (2016) use CERES data to show that shortwave reflection by low clouds over tropical oceans robustly decreases when the underlying surface warms, implying a positive shortwave feedback from tropical low clouds (TLCs). They use climate model simulations to argue that present-day observations of TLC reflection and surface temperature can narrow uncertainty in the strength of the shortwave TLC feedback under global warming and constrain equilibrium climate sensitivity (ECS). Using a weighting of climate models according to how well they reproduce CERES observations gives a ECS estimate with a most likely value of 4 K, and with a probability of less than 5% for values below 2.3 K.

- Nam et al. (2012) analyze outputs from multiple climate models participating in CMIP5 and compare them with CERES, CALIPSO and PARASOL observations. Compared to CERES all models overestimate the magnitude of both the SW and LW radiative effects of clouds. The models produce overly bright but too few low-clouds, and overestimate mid- and high-clouds above low clouds.

- Stephens et al. (2010) use observations from the A-Train constellation (Cloudsat, CALIPSO, Aqua CERES, MODIS, and AMSR-E) to study the properties of precipitating and non-precipitating low clouds. Results show that approximately 40% of low clouds precipitate (drizzle or rain), and that MODIS and AMSR-E cloud liquid water path (LWP) data agree when carefully screened for both overcast conditions and for a lack of precipitation. Precipitating low clouds tend to have larger liquid water paths, effective radii and optical depths compared to non-precipitating low clouds. Comparisons with global models reveal that models overestimate LWP and underestimate low cloud effective radius. As a result, low cloud optical depths are too high in models, resulting in an underestimation in the absorbed shortwave radiation by 10 Wm^{-2} between 30°S-30°N and 30 Wm^{-2} locally, based upon model comparisons with CERES TOA fluxes.

- Bryan et al. (2010) use satellite observations of surface winds from QuikSCAT, SST from AMSR-E, and TOA albedo from CERES to evaluate the representation of frontal scale air–sea interaction in high-resolution coupled climate models. The characteristics of frontal scale ocean–atmosphere interaction are realistically captured only when the ocean component is eddy resolving. Response to mesoscale SST features is strongest in the atmospheric boundary layer, but there is a deeper reaching response of the atmospheric circulation apparent in free tropospheric clouds. A positive correlation exists between high-pass filtered albedo and SST in the experiments with eddy-resolving oceans as well as in the CERES and AMSR-E satellite observations, but is absent in the experiment with lower ocean resolution. This is the first study to show the mesoscale SST influence on clouds and albedo using global observations over open ocean.

- CERES data have extensively been used to evaluate cloud-radiation processes in climate models. This includes evaluation of new ice cloud parameterizations (Baran et al, 2016; Eidhammer et al., 2016; Chern et al., 2016), low cloud parameterizations (Cheng and Xu, 2015), mixed-phase cloud parameterizations (Furtado et al., 2016), parameterizations of deep

convection (Boyle et al., 2015; Guo et al., 2015; Wang and Zhang, 2016), and parametrizations of subgrid-scale cloud water content variability (Hill et al., 2015). CERES data products provided new insights on CMIP5 GCM model ice cloud biases (Li et al., 2016), solar radiation budget biases due to inadequate representation of supercooled liquid water clouds (Bodas-Salcedo, 2016; McCoy et al., 2016), and biases in surface radiative fluxes (Loew et al., 2016; Zhang et al., 2016; Cretat et al., 2016).

C.3 Aerosol Radiative Forcing

- Satheesh and Ramanathan (2000) introduce a novel method of using CERES/TRMM TOA flux observations combined with independent surface radiometers to quantify aerosol direct radiative forcing (ADRF) simultaneously at the Earth's surface and TOA over the tropical northern Indian Ocean to within 5%. Mean clear-sky solar radiative heating associated with anthropogenic aerosols from the south Asian continent for the winters of 1998 and 1999 decreased at the ocean surface by 12 to 30 Wm^{-2}, but only by 4 to 10 Wm^{-2} at the TOA. This threefold difference (due largely to solar absorption by soot) and the large magnitude of the observed surface forcing both imply that tropical aerosols might slow down the hydrological cycle.

- Stevens (2015) calculate the difference in clear-sky albedo over the oceans between latitudes in the northern hemisphere and the corresponding latitudes in the southern hemisphere from CERES observations and CMIP5 AMIP model simulations for 2001-2013 (*Figure C.5.8*). At latitudes between 25° and 50°, where anthropogenic sources are expected to be large and contributions from mineral dust should be less important, models show roughly a factor of 5 larger hemispheric asymmetry than observations. Because anthropogenic aerosols are far more abundant in the NH, the results suggest that the models may be substantially overstating the magnitude of ADRF.

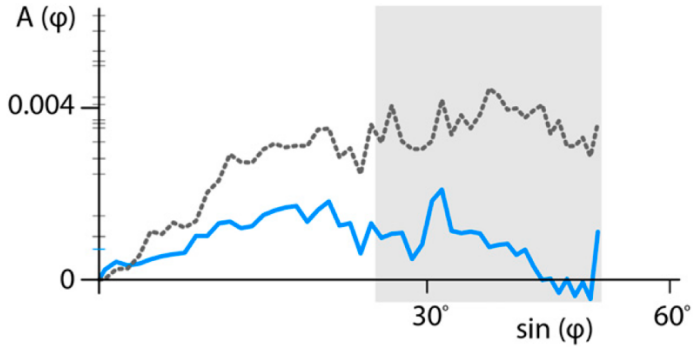

Figure C.5.8 Asymmetry (A(ϕ)) in zonally and annually averaged albedo over the oceans as a function of sine of latitude (ϕ). CERES measurements (blue) and the multimodel mean (dotted), excluding one outlier model (MRI-CGCM3). The mean between 25° and 50° latitude of the individual models and of CERES is indicated by the minor tick marks on the ordinate axis. (From Stevens et al., 2015).

- Conservation of energy is used in Murphy et al. (2009) as a constraint in order to determine the combined aerosol direct and indirect radiative forcing, currently the least understood forcing

acting on the climate system. The time dependence of various components of the Energy budget is derived from observations of surface temperature, ocean heat content, CERES TOA radiative fluxes, and radiative calculations of forcing due to greenhouse gases, volcanic aerosols and the sun. The direct and indirect radiative forcing by aerosols, determined as a residual term in the energy budget, is estimated to be -1.1± 0.4 W/m^2, consistent with the IPCCs AR4 best estimate.

- A novel approach was developed for studying aerosol-cloud interactions by combining MODIS and CERES observations with airmass back trajectory analysis and meteorological assimilation data in a study region off the west coast of Africa (Su et al., 2010). The back trajectory analysis separates oceanic and continental aerosol populations. Differences in MODIS cloud properties and CERES TOA albedo between the two populations were examined after controlling for differences in large-scale dynamics and thermodynamic state using meteorological assimilation data (estimated inversion strength, vertical velocity at 700 hPa). For various cloud liquid water path ranges, regions associated with aerosols of continental origin have higher cloud fraction, smaller cloud droplet effective radii, and significantly larger cloud optical depths and TOA albedos than those associated with oceanic origin. For cloud fraction greater than 80%, differences in effective radius, cloud optical depth and albedo are markedly reduced.

- Yorks et al. (2009) investigated the influences of African dust and smoke aerosols on cloud radiative effects over the tropical Atlantic Ocean for the month of July using 3 years (2006–2008) of collocated CALIPSO and CERES Aqua observations. Aerosol layer height and type below and above clouds are determined using CALIPSO, and SW and LW radiative fluxes are provided by CERES. When elevated Saharan dust layers are present above low-level clouds, SW radiative cooling is reduced by up to 30% compared to low-cloud cases in which there is no overlying dust. Similarly, in the case of smoke above low-level clouds, the SW radiative cooling is reduced by 12%. This study suggests there is a pronounced ADRE whereby absorption by dust or smoke layers above clouds reduces outgoing SW radiation at the TOA.

- Engström et al. (2015) use CERES and MODIS data to examine the spatial distribution of albedo variability that is independent of variations in cloud fraction and liquid water path (LWP) in order to find geographically coherent patterns of albedo enhancement and suppression associated with aerosol sources and sinks. The analysis is capable of sensing very small changes in average albedo of the order of 0.003 out of a total albedo of the order of 0.3.

- Christopher et al (2006) combine MODIS narrowband measurements with broadband CERES radiative fluxes to provide a measurement-based assessment of the global direct climate forcing of anthropogenic aerosols at the TOA for cloud free oceans. They find that the mean TOA DCF of anthropogenic aerosols over cloud-free oceans (60N–60S) is -1.4 ± 0.9 Wm^{-2}.

- Quaas et al. (2008) introduce a new method for deriving measurement-based estimates of aerosol direct and indirect radiative forcing using CERES and MODIS. They derive a statistical relationship between planetary albedo and cloud properties, and between the cloud properties and column aerosol concentration. Combining these relationships with a data set of satellite-

derived anthropogenic aerosol fraction, they estimate an anthropogenic radiative forcing of -0.9 ± 0.4 Wm^{-2} for the aerosol direct effect and -0.2 ± 0.1 Wm^{-2} for the cloud albedo effect. The results suggest that current global climate models may overestimate the cloud albedo effect.

- Sundström et al. (2015) use CERES and MODIS to determine the ADRE over China. Over heavily industrialized areas, the cooling at TOA reached -15 Wm^{-2}, and the associated AODs exceeded 0.5. Over the entire domain (20°N-45°N, 100°E-125°E), ADRE was -5 Wm^{-2}, with a strong seasonal variation.

References

Allan, R.P., C. Liu, N.G. Loeb, M.D. Palmer, M. Roberts, D. Smith, and P.-L. Vidale, 2014: Changes in global net radiative imbalance 1985–2012. Geophys. Res. Lett. 41, 5588–5597.

Andrews, T., J.M. Gregory, M. J. Webb, and K. E. Taylor, 2012b: Forcing, feedbacks and climate sensitivity in CMIP5 coupled atmosphere–ocean climate models. Geophys. Res. Lett., 39, L09712, doi:10.1029/2012GL051607.

Arking, A., and J.S. Levine, 1967: Earth albedo measurements: July 1963 to June 1964. J. Atmos. Sci., 24, 721-724.

Armour, K.C., C. Bitz, G.H. Roe, 2013: Time-varying climate sensitivity from regional feedbacks. J Climate. 26, 4518-34.

Baran, A. J., P. Hill, D. Walters, S. C. Hardiman, K. Furtado, P. R. Field, J. Manners, 2016: The impact of two coupled cirrus microphysics-radiation parameterizations on the temperature and specific humidity biases in the tropical tropopause layer in a climate model, J. Climate, 29 (14), 5299–5316, http://doi.org/10.1175/JCLI-D-15-0821.1.

Barkstrom, B. R., 1984: The Earth Radiation Budget Experiment (ERBE). Bull. Amer. Meteor. Soc., 65, 1170-1185.

Bates, J.J., X. Zhao, (eds), 2011: Report from the workshop on continuity of Earth radiation budget (CERB) observations: Post-CERES Requirements. NOAA Technical Report NESDIS 134. Washington, DC. [Available from: ftp://ftp.library.noaa.gov/noaa_documents.lib/NESDIS/TR_NESDIS/TR_NESDIS_134.pdf]

Bindoff, N. L. e. a., Climate Change 2013: The Physical Science Basis (IPCC). Cambridge Univ. Press: 2013; p 867–952.

Bodas-Salcedo, A., P. G. Hill, K. Furtado, K. D. Williams, P. R. Field, J. C. Manners, P. Hyder, and S. Kato, 2016: Large contribution of supercooled liquid clouds to the solar radiation budget of the Southern Ocean, J. Climate, 29 (11), 4213–4228, http://doi.org/10.1175/JCLI-D-15-0564.1.

Bony, S., B. Stevens, D.M.W. Frierson, C. Jakob, M. Kageyama, R. Pincus, T. G. Shepherd, S.C. Sherwood, A.P. Siebesma, A.H. Sobel, M. Watanabe, and M.J. Webb, 2015: Clouds, circulation and climate sensitivity. 8, 261-268. doi: 10.1038/NGEO2398

Boos, W. R., R. L. Korty, 2016: Regional energy budget control of the intertropical convergence zone and application to mid-Holocene rainfall, Nature Geoscience, 9(12), 892-897.

Boucher, O., et al., 2013: Clouds and Aerosols. In: Climate Change 2013: The Physical Science Basis. Contribution of Working Group I to the Fifth Assessment Report of the Intergovernmental Panel on Climate Change [Stocker, T.F., D. Qin, G.-K. Plattner, M. Tignor, S.K. Allen, J. Boschung, A. Nauels, Y. Xia, V. Bex and P.M. Midgley (eds.)]. Cambridge University Press, Cambridge, United Kingdom and New York, NY, USA.

Boyle, J. S., S. A. Klein, D. D. Lucas, H.-Y. Ma, J. Tannahill, and S. Xie, 2015: The parametric sensitivity of CAM5's MJO. J. Geophys. Res.-Atmospheres, 120 (4), http://doi.org/10.1002/2014JD022507.

Brient, F., and T. Schneider, 2016: Constraints on climate sensitivity from space-based measurements of low-cloud reflection. J. Climate, 29, 5821-5835.

Castet J.-F., and J.H. Saleh, 2009: Satellite reliability: statistical data analysis and modeling. J Spacecr Rocket. 46(5):1065–76.

Chen, Y.-C., M.W. Christensen, G.L. Stephens, J.H. Seinfeld, 2014: Satellite-based estimate of global aerosol–cloud radiative forcing by marine warm clouds, Nat. Geosci., 7(9), 643-646. https://doi.org/10.1038/ngeo2214.

Cheng, A., and K.-M. Xu, 2015: Improved low-cloud simulation from the Community Atmosphere Model with an advanced third-order turbulence closure, J. Climate, 28 (14), 5737–5762, http://doi.org/10.1175/JCLI-D-14-00776.1.

Chern, J.-D., W.-K. Tao, S. E. Lang, T. Matsui, J.-L. F. Li, K. I. Mohr, G. M. Skofronick-Jackson, and C. D. Peters-Lidard, 2016: Performance of the Goddard multiscale modeling framework with Goddard ice microphysical schemes, J. Advances in Modeling Earth Systems, 8 (1), 66–95, http://doi.org/10.1002/2015MS000469.

Christensen, M.W.; Y.-C. Chen, G.L. Stephens, 2016: Aerosol indirect effect dictated by liquid clouds. J. Geophys. Res., 121(24), 14,636–14,650 . https://doi.org/10.1002/2016JD025245.

Christopher, S.A., J. Zhang, Y.J. Kaufman, and L.A. Remer, 2006: Satellite-based assessment of top of atmosphere anthropogenic aerosol radiative forcing over cloud-free oceans. Geophys. Res. Lett., 33. https://doi.org/10.1029/2005GL025535.

Chung, E.-S., B.J. Soden, A.C. Clement, 2012: Diagnosing climate feedbacks in coupled ocean–atmosphere models. Surveys in Geophysics. 2012;33(3-4):733-44.

Church, J.A., N.J. White, C.M. Domingues, D.P. Monselesan, and E.R. Miles 2013: Sea-level and ocean heat-content change. Ocean Circulation and Climate, Vol. 103. 697-725. http://dx.doi.org/10.1016/B978-0-12-391851-2.00027-1.

Church, J.A., N.J. White, L.F. Konikow, C.M. Domingues, J.G. Cogley, E. Rignot, J.M. Gregory, M.R. van den Broeke, A.J. Monaghan, and I. Velicogna, 2011: Revisiting the Earth's sea-level and energy budgets from 1961 to 2008. Geophys. Res. Lett., 38, L18601, doi:10.1029/2011GL048794.

Coldewey-Egbers, M., S. Slijkhuis, B. Aberle, and D. Loyola, 2008: Long-term analysis of GOME in-flight calibration parameters and instrument degradation, Appl. Opt., 47, 4749-4761.

Collins, M., and Coauthors, 2013: Long-term Climate Change: Projections, Commitments and Irreversibility. In Climate Change 2013: The Physical Science Basis. Contribution of Working Group I to the Fifth Assessment Report of the Intergovernmental Panel on Climate Change. Stocker, T. F. et al., Ed.; Cambridge University Press; pp. 1029–1136.

Colman R., 2003: A comparison of climate feedbacks in general circulation models. Climate Dynamics. 20:865–73.

Cooper, D.L., P.C. Hess, J.L. Gleason, and K.J. Priestley, 2013: Clouds and the Earth's Radiant Energy System (CERES) Data Management system BiDirectional Scans (BDS) Collection Document, Version 4. [Available from: https://ceres.larc.nasa.gov/documents/collect_guide/pdf/BDS_CG_R3V4.pdf].

Crétat, J., S. Masson, S. Berthet, G. Samson, P. Terray, J. Dudhia, F. Pinsard, and C. Hourdin, 2016: Control of shortwave radiation parameterization on tropical climate SST-forced simulation, Climate Dynamics, 1–20, http://doi.org/10.1007/s00382-015-2934-1.

Daniels, J.L., G.L. Smith, K.J. Priestley, and S. Thomas, 2015: Using lunar observations to validate in-flight calibrations of Clouds and the Earth's Radiant Energy System Instruments, IEEE Trans. Geosci. Rem. Sens. 53, 5110- 5116.

DeAngelis, A. M., X. Qu, M. D. Zelinka, and A. Hall, 2015: An observational radiative constraint on hydrologic cycle intensification. Nature, 528, 249–253.

Dessler, A.E., 2010: A Determination of the cloud feedback from climate variations over the past decade. Science. 2010;330:1523–7.

Dessler, A.E., T. Mauritsen, and B. Stevens, 2018: The influence of internal variability on Earth's energy balance framework and implications for estimating climate sensitivity. Atmos. Chem. Phys., 18, 5147-5155, 2018. https://doi.org/10.5194/acp-18-5147-2018

Doelling, D. R., N. G. Loeb, D. F. Keyes, M. L. Nordeen, D. Morstad, C. Nguyen, B. A. Wielicki, D. F. Young, and M. Sun, 2013: Geostationary enhanced temporal interpolation for CERES flux products. J. Atmos. Oceanic Technol., 30, 1072-1090.

Doelling, D. R., K.V. Khlopenkov, A. Okuyama, C.O. Haney, A. Gopalan, B.R. Scarino, M. Nordeen, R. Bhatt, and L.A. Avey, 2015: MTSAT-1R visible imager point spread correction function, Part I: The need for, validation of, and calibration with. IEEE Trans. Geosci. Rem. Sens., 53 (3), 1513-1526.

Eidhammer, T., H. Morrison, D. Mitchell, A. Gettelman, and E. Erfani, 2016: Improvements in global climate model microphysics using a consistent representation of ice particle properties. J. Climate, in press, https://doi.org/10.1175/JCLI-D-16-0050.1.

England, M. H., and Coauthors, 2014: Recent intensification of wind-driven circulation in the Pacific and the ongoing warming hiatus. Nat. Climate Change, 4, 222–227, doi:10.1038/nclimate2106.

Engström, A., F.A.-M. Bender, R.J. Charlson, and R. Wood, 2015: Geographically coherent patterns of albedo enhancement and suppression associated with aerosol sources and sinks, Tellus B: Chemical and Physical Meteorology, 67:1, 26442, DOI:10.3402/tellusb.v67.26442.

Feng, N., S.A.Christopher, 2013: Satellite and surface-based remote sensing of Southeast Asian aerosols and their radiative effects. Atmos. Res., 122, 544-554. doi: 10.1016/j.atmosres.2012.02.018.

Forster, P.M., T. Andrews, P. Good, J.M. Gregory, L.S. Jackson, and M. Zelinka, 2013: Evaluating adjusted forcing and model spread for historical and future scenarios in the CMIP5 generation of climate models: Forcing in CMIP5 climate models. J. Geophys. Res. 118, 1139–1150. https://doi.org/10.1002/jgrd.50174.

Forster P.M., 2016: Inference of climate sensitivity from analysis of Earth's energy budget. Annual Review of Earth and Planetary Sciences. 2016;44:85-106.

Furtado, K., P. R. Field, I. A. Boutle, C. J. Morcrette, and J. M. Wilkinson, 2016: A physically based subgrid parameterization for the production and maintenance of mixed-phase clouds in a general circulation model, J. Atmos. Sci., 73 (1), 279–291, http://doi.org/10.1175/JAS-D-15-0021.1.

GCOS, 2010: Implementation Plan for the Global Observing System for Climate in Support of the UNFCCC (2010 Update), Global Climate Observing System GCOS-138, WMO/TD No. 1523, World Meteorological Organization, Geneva, Switzerland, 186 pp.

Gould, J., et. al., 2004: Argo profiling floats bring new era of in situ ocean observations. Eos Trans. AGU, 85, 185-191.

Green, R. N., and B.A. Wielicki, 1996: Clouds and the Earth's Radiant Energy System (CERES) Algorithm Theoretical Basis Document: Convolution of imager cloud properties with CERES footprint point spread function.

Gryspeerdt, E., J. Quaas, N. Bellouin, 2016: Constraining the aerosol influence on cloud fraction. J. Geophys. Res.: 121(7), 3566–3583 . doi:10.1002/2015JD023744.

Guo, Z., M. Wang, Y. Qian, V. E. Larson, S. Ghan, M. Ovchinnikov, P. A. Bogenschutz, A. Gettelman, and T. Zhou, 2015: Parametric behaviors of CLUBB in simulations of low clouds in the Community Atmosphere Model (CAM). J. Advances in Modeling Earth Systems, 7 (3), 1005–1025, http://doi.org/10.1002/2014MS000405.

Hansen, J., L. Nazarenko, R. Ruedy, M. Sato, J. Willis, A. Del Genio, D. Koch, A. Lacis, K. Lo, S. Menon, T. Novakov, J. Perlwitz, G. Russell, G.A. Schmidt, and N. Tausnev, 2005: Earth's energy imbalance: confirmation and implications. Science, 308, 1431-1435.

Hansen, J., M. Sato, P. Kharecha, and K. von Schuckmann, 2011: Earth's Energy Imbalance and Implications. Atmos. Chem. Phys., 11, 13421-13449. doi:10.5194/acp-11-13421-2011.

Harries, J.E., et al., 2005: The Geostationary Earth Radiation Budget Project. Bull. Amer. Meteor. Soc., 86(7), 945-960 . https://doi.org/10.1175/BAMS-86-7-945.

Harrison, E. F., P. Minnis, and G. Gibson, 1983: Orbital and cloud cover sampling analyses for multisatellite earth radiation budget experiments. J. Spacecraft and Rockets, vol. 20, no. 5, 491-495, DOI:10.2514/3.25634.

Harrison, E. F., D. R. Brooks, P. Minnis, B. A. Wielicki, W. F. Staylor, G. G. Gibson, D. F. Young, F. M. Denn, and the ERBE Science Team, 1988: First Estimates of the Diurnal Variation of LW Radiation from the Multiple-Satellite Earth Radiation Budget Experiment (ERBE).Bulletin of the American Meteorological Society, vol. 69, no. 10, 1144-1151, DOI: 10.1175/1520-0477(1988)069<1144:FEOTDV>2.0.CO;2.

Hartmann, D. L., and Ceppi, P., 2014: Trends in the CERES dataset, 2000 - 2013: the effects of sea ice and jet shifts and comparison to climate models. Journal of Climate, 27 (6), 2444 - 2456, doi: 10.1175/JCLI-D-13-00411.1

Herzig, H., A. R. Toft, and C. M. Fleetwood, Jr., 1993: Long-duration orbital effects on optical coating materials. Appl. Opt., 32, 1798-1804.

Hill, P. G., C. J. Morcrette, and I. A. Boutle, 2015: A regime-dependent parametrization of subgrid-scale cloud water content variability, Quarterly J. Royal Meteorolog. Soc., 141 (691), 1975–1986, http://doi.org/10.1002/qj.2506.

House, F. B., A. Gruber, G.E. Hunt, and A.T. Mecherikunnel, 1986: History of Satellite Missions and Measurements of the Earth Radiation Budget (1957-1984), Rev. Geophys. 24, 357 – 377.

Hsu, N.C., S.-C. Tsay, M.D. King, and J.R. Herman, 2004: Aerosol properties over bright-reflecting source regions. IEEE Geosci. Rem. Sens., 42 (3), 557-569.

Huang, X., N.G. Loeb, and H. Chuang, 2012: Assessing stability of CERES-FM3 daytime LW unfiltered radiance with AIRS radiances, J. Atmos. Ocean. Tech., 29(3), 375-381. doi: 10.1175/JTECH-D-11-00066.1.

Hunt, G.E., R. Kandel, and A.T. Mecherikunnel, 1986: A history of presatellite investigations of the Earth's radiation budget. Rev. Geophys., 24, 351-356.

IPCC, 2013: Summary for Policymakers. In: Climate Change 2013: The Physical Science Basis. Contribution of Working Group I to the Fifth Assessment Report of the Intergovernmental Panel on Climate Change [Stocker, T.F., D. Qin, G.-K. Plattner, M. Tignor, S.K. Allen, J. Boschung, A. Nauels, Y. Xia, V. Bex and P.M. Midgley (eds.)]. Cambridge University Press, Cambridge, United Kingdom and New York, NY, USA.

Jacobowitz, H., and R. J. Tighe, 1984: The Earth Radiation Budget derived from the NIMBUS 7 ERB Experiment. J. Geophys. Res., vol. 89, no. D4, 4997–5010, DOI:10.1029/JD089iD04p04997.

Johnson, G.C., J. M. Lyman, and N. G. Loeb, 2016: Improving estimates of Earth's energy imbalance. Nature Climate Change, 6, 639-640.

Jones, T.A., S.A. Christopher, and J. Quaas, 2009: A six year satellite-based assessment of the regional variations in aerosol indirect effects. Atmos. Chem. Phys., 9, 4091–4114, 2009

Kato, S., N. G. Loeb, F. G. Rose, D. R. Doelling, D. A. Rutan, T. E. Caldwell, L. Yu, R. A. Weller, 2013: Surface Irradiances Consistent with CERES-Derived Top-of-Atmosphere Shortwave and LW Irradiances. J. Climate, 26 (9), 2719-2740.

Kato, S., F.G. Rose, D.A. Rutan, T.J. Thorsen, N.G. Loeb, D.R. Doelling, X. Huang, W.L. Smith, W. Su, S.-H. Ham, 2018: Surface irradiances of Edition 4.0 Clouds and the Earth's Radiant Energy System (CERES) Energy Balanced and Filled (EBAF) data product, J. Climate, (In Press). https://doi.org/10.1175/JCLI-D-17-0523.1.

Khlopenkov, K. V., D.R. Doelling, and A. Okuyama, 2015: MTSAT-1R visible imager point spread function correction, Part II: Theory. IEEE Trans. Geosci. Rem. Sens., 53 (3), 1504-1512.

Kopp, G., G. Lawrence, and G. Rottman, 2005: The total irradiance monitor (TIM): Science results. Solar Physics, 230, 129-139.

Kopp, G., P. Smith, C. Belting, Z. Castleman, G. Drake, J. Espejo, K. Heuerman, J. Lanzi, and D. Stuchlik, 2017. Radiometric flight results from the HyperSpectral Imager for Climate Science (HySICS). Geosci. Instrum. Method. Data Syst., 6, 169–191. doi:10.5194/gi-6-169-2017.

Kratz, D.P., S.K. Gupta, A.C. Wilber, and V.E. Sothcott, 2010: Validation of the CERES Edition 2B Surface-Only Flux Algorithms, J. Appl. Meteorol. Climatol., 49(1), 164-180. doi:10.1175/2009JAMC2246.1

Kyle, H. L., 1990: Nimbus-7 earth radiation budget data set and its uses. In Long-Term Monitoring of the Earth's Radiation Budget, Proc. SPIE: Orlando, FL, 1990; Vol. 1299, p 27.

Lebsock, M.D., G.L. Stephens, and C. Kummerow, 2008: Multisensor satellite observations of aerosol effects on warm clouds. J. Geophys. Res., 113, D15205, doi:10.1029/2008JD009876.

Lee III, R.B. et al., 1997: Clouds and the Earth's radiant energy system (CERES) Algorithm Theoretical Basis Document: Instrument geolocate and calibrate Earth radiances. [Available from: https://ceres.larc.nasa.gov/documents/ATBD/pdf/r2_2/ceres-atbd2.2-s1.0.pdf].

Lee III, R. B., B.R. Barkstrom, H.C. Bitting, D. Crommelynck, J. Paden, D.K. Pandey, K.J. Priestley, G.L. Smith, S. Thomas, K. Thornhill, R.S. Wilson, 1998: Prelaunch calibrations of the Clouds and the Earth's Radiant Energy System (CERES) tropical rainfall measuring mission and Earth Observing System morning (EOS-AM1) spacecraft thermistor bolometer sensors. IEEE Trans. Geosci. Rem.Sens., 36 (4), 1173-1185.

Lee, R. B., L.M. Avis, M.A. Gibson, L.P. Kopia, 1992: Characterizations of the Mirror Attenuator Mosaic - Solar Diffuser Plate. Appl. Opt., 31 (31), 6643-6652.

Levine, X. J., and W. R. Boos 2017: Land surface albedo bias in climate models and its association with tropical rainfall, Geophys. Res. Lett., 44, 6363–6372, doi:10.1002/ 2017GL072510.

Levy, R.C.; L.A. Remer, S. Mattoo, E.F. Vermote, and Y.J. Kaufman, 2007: Second-generation operational algorithm: Retrieval of aerosol properties over land from inversion of Moderate Resolution Imaging Spectroradiometer spectral reflectance. J. Geophys. Res., 112 (D13).

Li, J.-L. F., D. E. Waliser, G. Stephens, and S. Lee, 2016: Characterizing and understanding cloud ice and radiation budget biases in global climate models and reanalysis, Meteorolog. Monographs, 56, 13.1-13.20, http://doi.org/10.1175/AMSMONOGRAPHS-D-15-0007.1.

Li, Y., D. W. J. Thompson, Y. Huang, and M. Zhang (2014), Observed linkages between the northern annular mode/North Atlantic Oscillation, cloud incidence, and cloud radiative forcing, Geophys. Res. Lett., 41, 1681–1688, doi:10.1002/2013GL059113.

Loeb, N. G., K. J. Priestley, D. P. Kratz, E. B. Geier, R. N. Green, B. A. Wielicki, P. O. R. Hinton, and S. K. Nolan, 2001: Determination of unfiltered radiances from the Clouds and the Earth's Radiant Energy System (CERES) instrument. J. Appl. Meteor., 40, 822– 835.

Loeb, N.G. and S. Kato, 2002: Top-of-atmosphere direct radiative effect of aerosols from the Clouds and the Earth's Radiant Energy System Satellite instrument (CERES). J. Climate, 15, 1474-1484.

Loeb, N. G., K. Loukachine, N. Manalo-Smith, B.A. Wielicki, and D.F. Young, 2003: Angular distribution models for top-of-atmosphere radiative flux estimation from the Clouds and the Earth's Radiant Energy System instrument on the Tropical Rainfall Measuring Mission satellite. Part II: Validation. J. Appl. Meteorol., 42 (12), 1748-1769.

Loeb, N.G., and N. Manalo-Smith, 2005: Top-of-atmosphere direct radiative effect of aerosols over global oceans from merged CERES and MODIS observations, J. Climate, 18, 3506-3526.

Loeb, N.G., S. Kato, K. Loukachine, N. and Manolo-Smith, 2005: Angular distribution models for top-of-atmosphere radiative flux estimation from the Clouds and the Earth's Radiant Energy System Instrument on the Terra satellite. Part I: Methodology, J. Atmos. Oceanic Technol., 22, 338 – 351.

Loeb, N.G., and G. L. Schuster, 2008: An observational study of the relationship between cloud, aerosol and meteorology in broken low-level cloud conditions, J. Geophys. Res., 113, doi:10.1029/2007JD009763.

Loeb, N.G., B.A. Wielicki, D.R. Doelling, G.L. Smith, D.F. Keyes, S. Kato, N.M. Smith, and T. Wong, 2009a: Towards optimal closure of the earth's top-of-atmosphere radiation budget. *J. Climate*, **22**, 748-766.

Loeb, N. G., B. A. Wielicki, T. Wong, and P. A. Parker, 2009b: Impact of data gaps on satellite broadband radiation records, J. Geophys. Res., 114, D11109, doi:10.1029/2008JD011183.

Loeb, N.G., S. Kato, W. Su, T. Wong, F.G. Rose, D.R. Doelling, J.R. Norris, and X. Huang, 2012a: Advances in understanding top-of-atmosphere radiation variability from satellite observations. Surv. Geophys., **33**, 359-385. DOI 10.1007/s10712-012-9175-1.

Loeb, N. G., J.M. Lyman, G.C Johnson, R.P. Allan, D.R. Doelling, T. Wong, B.J. Soden, and G.L. Stephens, 2012b: Observed changes in top-of-the-atmosphere radiation and upper-ocean heating consistent within uncertainty. Nat. Geosci., 5 (2), 110-113.

Loeb, N. G., W. Su, D.R. Doelling, T. Wong, P. Minnis, S. Thomas, W.F. Miller, **2016a**: Earth's top-of-atmosphere radiation budget. ScienceDirect, Reference Module in Earth Systems and Environmental Sciences. doi: 10.1016/B978-0-12-409548-9.10367-7.

Loeb, N.G., and B.A. Wielicki, **2016b**: Satellites and satellite remote sensing: Earth's Radiation Budget. Encyclopedia of Atmospheric Sciences (Second Edition), 67-76. doi:10.1016/B978-0-12-382225-3.00349-2.

Loeb, N.G., N. Manalo-Smith, W. Su, M. Shankar, and S. Thomas, **2016c**: CERES top-of-atmosphere Earth radiation budget climate data record: Accounting for in-orbit changes in instrument calibration. *Remote Sens*., 8, 182; doi:10.3390/rs8030182.

Loeb, N. G., D. R. Doelling, H. Wang, W. Su, C. Nguyen, J. G. Corbett, L. Liang, C. Mitrescu, F. G. Rose, and S. Kato, **2018a**: Clouds and the Earth's Radiant Energy System (CERES) Energy Balanced and Filled (EBAF) Top-of-Atmosphere (TOA) Edition 4.0 data product, J. Climate, 31, 895-918. doi: 10.1175/JCLI-D-17-0208.1.

Loeb, N.G., T. Thorsen, J. Norris , H. Wang , and W. Su, **2018b**: Changes in Earth's energy budget during and after the "pause" in global warming: An observational perspective. Climate (submitted).

Loew, A., A. Andersson, J. Trentmann, and M. Schröder, 2016: Assessing surface solar radiation fluxes in the CMIP ensembles, J. Climate, 29 (20), 7231–7246. https://doi.org/10.1175/JCLI-D-14-00503.1.

London, J., 1957: A study of the atmospheric heat balance. Final Rept., Contract AF 19(122)-165, Dept. of Meteorology and Oceanography, New York University, 99 pp.

Lukashin, C., B. A. Wielicki, D. F. Young, K. Thome, Z. Jin, and W. Sun, 2012: Uncertainty estimates for imager reference inter-calibration with CLARREO reflected solar spectrometer. IEEE Trans. on Geo. and Rem. Sensing, 51, no.3, pp.1425,1436, doi:10.1109/TGRS.2012.2233480.

Lukashin, C., B. A. Wielicki, D. F. Young, K. Thome, Z. Jin, and W. Sun, 2013: Uncertainty Estimates for Imager Reference Inter-Calibration With CLARREO Reflected Solar Spectrometer, IEEE Trans. Geo. Rem. Sens., 51, 1425-1436, doi:10.1109/TGRS.2012.2233480.

McCoy, D. T., I. Tan, D. L. Hartmann, M. D. Zelinka, and T. Storelvmo, 2016: On the relationships among cloud cover, mixed-phase partitioning, and planetary albedo in GCMs, J. Advances in Modeling Earth Systems, 8 (2), 650–668. http://doi.org/10.1002/2015MS000589.

Minnis, P., S. Sun-Mack, D.F. Young, P.W. Heck, D.P. Garber, Y. Chen, D.A. Spangenberg, R.F. Arduini, Q.Z. Trepte, W.L. Smith, J.K. Ayers, S.C. Gibson, W.F. Miller, V. Chakrapani, Y. Takano, K.-N. Liou, Y. Xie, P. Yang, 2011: CERES Edition-2 cloud property retrievals using TRMM VIRS and Terra and Aqua MODIS data, Part I: Algorithms. IEEE Trans. Geosci. Rem. Sens., 49 (11), 4374-4400.

Minnis, P., S. Sun-Mack, Q. Z. Trepte, F.-L. Chang, P. W. Heck, Y. Chen, Y. Yi, R. F. Arduini, K. Ayers, K. Bedka, S. Bedka, R. Brown, S. Gibson, E. Heckert, G. Hong, Z. Jin, R. Palikonda, R. Smith, W. L. Smith, Jr., D. A. Spangenberg, P. Yang, C. R. Yost, and Y. Xie, 2010: CERES Edition 3 cloud retrievals. In AMS 13th Conf. Atmospheric Radiation, Portland, OR, , 2010; p 7 pp.

Minnis, P., W.L. Smith, Jr., D.P. Garber, J.K. Ayers, and D.R. Doelling, 1995: Cloud properties derived from GOES-7 for the Spring 1994 ARM Intensive Observing Period using Version 1.0.0 of the ARM satellite data analysis program. NASA RP 1366, August 1995, 59 pp.

Minnis, P. et al., 2008: Near-real time cloud retrievals from operational and research meteorological satellites, Proc. SPIE Remote Sens.Clouds Atmos. XIII, Cardiff, Wales, UK, 15-18 September, 2008, Cardiff, Wales, UK, 2008; pp 7107-2, 8 pp.

Minnis, P., Q.Z. Trepte, S. Sun-Mack, Y. Chen, D.R. Doelling, D.F. Young, D.A. Spangenberg, W.F. Miller, B.A. Wielicki, R.R. Brown, S.C. Gibson, and E.B. Geier, 2008: Cloud detection in nonpolar regions for CERES using TRMM/VIRS and Terra and Aqua MODIS data. IEEE Trans. Geosci. Rem.Sens., 46, 3857-3884.

Minnis, P., A.V. Gambheer, and D.R. Doelling, 2004: Azimuthal anisotropy of LW and infrared window radiances from CERES TRMM and Terra data. J. Geophys. Res., 109, D08202,doi:10.1029/2003JD004471.

Minnis, P., S. Sun-Mack, C. R. Yost, Y. Chen, F.-L. Chang, P. W. Heck, R. F. Arduini, Q. Z. Trepte, K. Ayers, K. Bedka, S. Bedka, R. R. Brown, D. R. Doelling, A. Gopalan, E. Heckert, G. Hong, Z. Jin, R. Palikonda, R. Smith, W. L. Smith, Jr., B. Scarino, D. A. Spangenberg, P. Yang, Y. Xie, and Y. Yi, 2018: Changes to CERES MODIS cloud product retrieval algorithms for Edition 4. IEEE Trans. Geosci. Remote Sens. (in preparation).

Minnis, P., E. F. Harrison, L. L. Stowe, G. G. Gibson, F. M. Denn, D. R. Doelling, and W. L. Smith Jr., 1993: Radiative Climate Forcing by the Mt. Pinatubo Eruption. Science, vol. 259, 1411-1415, DOI:10.1126/science.259.5100.1411.

National Academies of Sciences, Engineering, and Medicine, 2018, Thriving on Our Changing Planet – A Decadal Strategy for Earth Observation from Space. Washington, DC: The National Academies Press, doi:10.17226/24938.

National Research Council, 2004: Climate Data Records from Environmental Satellites: Interim Report. Washington, D.C.: The National Academies Press, doi:10.17226/10944.

National Research Council, 2007, Earth Science and Applications from Space: National Imperatives for the Next Decade and Beyond. Washington, D.C.: The National Academies Press, doi: 10.17226/11820.

National Academies of Sciences, Engineering, and Medicine. 2015. Continuity of NASA Earth Observations from Space: A Value Framework. Washington, DC: The National Academies Press.

Ohring, G., B. Wielicki, R. Spencer, B. Emery, and R. Datla, (eds), 2004: Satellite Instrument Calibration for Measuring Global Climate Change, Report of a Workshop, NIST Publication NISTIR 7047, 101 pp.

Ohring, G., B. Wielicki, R. Spencer, W.J. Emery, and R. Datla, 2005: Satellite instrument calibration for measuring global climate change: Report of a workshop. Bull. Am. Met. Soc ., 86 , 1303–1313.

Ohring, G. et al, 2007: Achieving satellite instrument calibration for climate change. EOS, Transactions American Geophysical Union , 88 , 136.

Painemal, D., S. Kato, and P. Minnis, 2014: Boundary layer regulation in the southeast Atlantic cloud microphysics during the biomass burning season as seen by the A-train satellite constellation. J. Geophys. Res. 119(19), 2014JD022182. doi:10.1002/2014JD022182.

Patadia, F., P. Gupta, and S.A. Christopher, 2008a: First observational estimates of global clear sky shortwave aerosol direct radiative effect over land. Geophys. Res. Lett., 35(4), L04810 . doi:10.1029/2007GL032314.

Patadia, F., P. Gupta, S.A. Christopher, and J.S. Reid, 2008b: A multisensor satellite-based assessment of biomass burning aerosol radiative impact over Amazonia. J. Geophys. Res., 113(D12, D12214, doi: 10.1029/2007JD009486.

Paulot, F., D. Paynter, P. Ginoux, V. Naik, and L. Horowitz, 2018: Changes in the aerosol direct radiative forcing from 2001 to 2015: observational constraints and regional mechanisms. Atmos. Chem. Phys., doi:10.5194/acp-2018-148.

Priestley, K. J., B.R. Barkstrom, R.B. Lee, R.N. Green, S. Thomas, R.S. Wilson, P.L. Spence, J. Paden, D.K. Pandey, A. Al-Hajjah, 2000: Postlaunch radiometric validation of the Clouds and the Earth's Radiant Energy System (CERES) Proto-flight Model on the Tropical Rainfall Measuring Mission (TRMM) spacecraft through 1999. J Appl. Meteor., 39 (12), 2249-2258.

Priestley, K.J., G.L. Smith, S. Thomas, D. Cooper, R.B. Lee, D. Walikainen, P. Hess, Z.P. Szewczyk, and R. Wilson, 2011: Radiometric performance of the CERES earth radiation budget climate record sensors on the EOS Aqua and Terra spacecraft through April 2007. J. Atmos. Ocean. Technol. 28, 3–21.

Quaas, J., O. Boucher, N. Bellouin, and S. Kinne, 2008: Satellite-based estimate of the direct and indirect aerosol climate forcing, J. Geophys. Res., 113, doi:10.1029/2007JD008962.

Ramanathan V., R. D. Cess, E. F. Harrison, P. Minnis, B. R. Barkstrom, E. Ahmad, D. Hartmann, 1989: Cloud-Radiative Forcing and Climate: Results from the Earth Radiation Budget Experiment. Science. vol. 243, no. 4887, 57-63, DOI:10.1126/science.243.4887.57.

Raschke, E., and W.R. Bandeen, 1970: The radiation balance of the planet Earth from radiation measurements of the satellite Nimbus II. J Appl Meteorol 1970, 9, 215-238.

Raschke, E., T. H. Vonder Haar, W.R. Bandeen, and M. Pasternak, 1973: The annual radiation balance of the earth-atmosphere system during 1969-70 from Nimbus-3 measurements. J. Atmos. Sci., 30, 341-364.

Remer, L. A., R.G. Kleidman, R.C. Levy, Y.J. Kaufman, D. Tanré, S. Mattoo, J.V. Martins, C. Ichoku, I. Koren, H. Yu, and B.N. Holben, 2008: Global aerosol climatology from the MODIS satellite sensors. J. Geophys. Res., 113 (D14).

Rhein, M., and Coauthors. Observations: Ocean. In Climate Change 2013: The Physical Science Basis, Stocker, T. F. et al., Ed.; Cambridge University Press, 2013; pp. 255–315.

Roca, R., H. Brogniez, P. Chambon, O. Chomette, S. Cloché, M.E. Gosset, J.-F. Mahfouf, R. Raberanto, N. Viltard, 2015: The Megha-Tropiques mission: a review after three years in orbit, Atmospheric Science, 3, doi:10.3389/feart.2015.00017.

Roithmayr, C.M., Lukashin, C., Speth, P.W., Kopp, G., Thome, K.,Wielicki, B.A., Young, D.F, 2014a: "CLARREO Approach for Reference Inter-Calibration of Reflected Solar Sensors: On-Orbit Data Matching and Sampling" IEEE TGRS, Special Issue on Satellite Intercalibration, 52, 10.1109/TGRS.2014.2302397.

Roithmayr, C. M., C. Lukashin, P. W. Speth, D. F. Young, B. A. Wielicki, K. J. Thome, G. Kopp, 2014b: "Opportunities to Intercalibrate Radiometric Sensors from International Space Station," J. Atmos. Oceanic Technol., 31, pp. 890 - 902.

Rose, F. G., D. A. Rutan, , T. Charlock, G. L. Smith, and S. Kato, 2013: An Algorithm for the Constraining of Radiative Transfer Calculations to CERES-Observed Broadband Top-of-Atmosphere Irradiance. J. Atmos. and Ocean. Tech., 30 (6), 1091-1106.

Rutan, D. A., S. Kato, D.R. Doelling, F.G. Rose, L.T. Nguyen, T.E. Caldwell, and N.G. Loeb, 2015: CERES Synoptic Product: Methodology and Validation of Surface Radiant Flux. J. Atmos. Ocean. Tech., 32 (6), 1121-1143.

Rutan, D. A., G.L. Smith, and T. Wong, 2014: Diurnal Variations of Albedo Retrieved from Earth Radiation Budget Experiment Measurements. J. Appl. Meteor. Climatol., vol. 53, 2747–2760, DOI:10.1175/JAMC-D-13-0119.1.

Satheesh, S.K.; V. Ramanathan, 2000: Large differences in tropical aerosol forcing at the top of the atmosphere and Earth's surface. Nature, 405(6782), 60-63. doi:10.1038/35011039.

Sena, E.T., P. Artaxo, and A.L. Correia, 2013: Spatial variability of the direct radiative forcing of biomass burning aerosols and the effects of land use change in Amazonia, Atmos. Chem. Phys., 13(3), 1261-1275. doi:10.5194/acp-13-1261-2013.

Sena, E.T., and P. Artaxo, 2015: A novel methodology for large-scale daily assessment of the direct radiative forcing of smoke aerosols. Atmos. Chem. Phys., 15, 5471-5483. doi:10.5194/acp-15-5471-2015.

Shankar, M., S. Thomas, and K.J. Priestley, 2010: Pre-launch characterization of spectral response functions for the Clouds and Earth's Radiant Energy System (CERES) instrument sensors. In Earth Observing Systems Xv, Butler, J. J.; Xiong, X.; Gu, X., Eds., Vol. 7807.

Slessarev, E. W., Y. Lin, N. L. Bingham, J. E. Johnson, Y. Dai, J. P. Schimel, O. A. Chadwick, 2016: Water balance creates a threshold in soil pH at the global scale , Nature, 540(7634), 567-569.

Smith, G. L., 1994: Effects of time response on the point spread function of a scanning radiometer. Appl Optics, 33 (30), 7031-7037.

Smith, G. L., R.N. Green, E. Raschke, L.M. Avis, J.T. Suttles, B.A. Wielicki, and R. Davies, 1986: Inversion methods for satellite studies of the Earth's radiation budget: Development of algorithms for the ERBE Mission. Rev. Geophys., 24, 407-421.

Smith, G. L. and D. A. Rutan, 2003: The Diurnal Cycle of Outgoing LW Radiation from Earth Radiation Budget Experiment Measurements. J. Atmos. Sci., vol. 60, 1529–1542, DOI:10.1175/2997.1.

Smith, W. L., J. Hickey, H. B. Howell, H. Jacobowitz, D. T. Hilleary and A. J. Drummond, 1977: Nimbus 6 Earth Radiation Budget Experiment. Appl. Opt., vol. 16, 306-318, DOI:10.1364/AO.16.000306.

Soden B., and I.M. Held, 2006: An assessment of climate feedbacks in coupled ocean–atmosphere models. J Climate. 19:3354-60.

Stackhouse, P. W., S. K. Gupta, S. J. Cox, J. C. Mikovitz, and M. Chiacchio, 2004: 12-year surface radiation budget dataset. GEWEX News, 14, 10-12, November.

Stephens, G.L., J. Li, M. Wild, C.A. Clayson, N. Loeb, S. Kato, T. L'Ecuyer, P.W. Stackhouse, M. Lebsock, and T. Andrews, 2012: An update on Earth's energy balance in light of the latest global observations. Nature Geoscience 5, 691–696. https://doi.org/10.1038/ngeo1580.

Stephens, G.L., and T. L'Ecuyer, 2015: The Earth's energy balance. Atmos. Res., 166, 195–203. doi: 10.1016/j.atmosres.2015.06.024.

Stevens, B., and S. Bony, 2013: What are climate models missing? Science, 340, 1053-1054.

Stocker, T.F., and Coauthors, 2013: Technical Summary. In: Climate Change 2013: The Physical Science Basis. Contribution of Working Group I to the Fifth Assessment Report of the Intergovernmental Panel on Climate Change [Stocker, T.F., et al., (eds.)]. Cambridge University Press, Cambridge, United Kingdom and New York, NY, USA.

Stubenrauch, C.J., W.B. Rossow, S. Kinne, S. Ackerman, G. Cesana, H. Chepfer, L. Di Girolamo, B. Getzewich, A. Guignard, A. Heidinger, B.C. Maddux, W.P. Menzel, P. Minnis, C. Pearl, S. Platnick, C. Poulsen, J. Riedi, S. Sun-Mack, A. Walther, D. Winker, S. Zeng, and G. Zhao, 2013: Assessment of Global Cloud Datasets from Satellites: Project and Database Initiated by the GEWEX Radiation Panel. Bull. Amer. Met. Soc., 94 (7), 1031-1049.

Su, W., N.G. Loeb, K.-N. Xu, G.L. Schuster, Z.A. Eitzen, 2010: An estimate of aerosol indirect effect from satellite measurements with concurrent meteorological analysis. J. Geophys. Res., 115(D18), D18219. doi:10.1029/2010JD013948.

Su, W., J. Corbett, Z. Eitzen, and L. Liang, 2015a: Next-generation angular distribution models for top-of-atmosphere radiative flux calculation from CERES instruments: methodology. Atmos. Meas. Tech., 8(2), 611-632. http://dx.doi.org/10.5194/amt-8-611-2015.

Su, W., J. Corbett, Z. Eitzen, and L. Liang, 2015b: Next-generation angular distribution models for top-of-atmosphere radiative flux calculation from CERES instruments: validation. Atmos. Meas. Tech., 8, 3297–3313, doi:10.5194/amt-8-3297-2015.

Su, W., L. Liang, W.F. Miller, and V.E. Sothcott, 2017: The effects of different footprint sizes and cloud algorithms on the top-of-atmosphere radiative flux calculation from the Clouds and Earth's Radiant Energy System (CERES) instrument on Suomi National Polar-orbiting Partnership (NPP), Atmos. Meas. Tech., 10, 4001-4011. https://doi.org/10.5194/amt-10-4001-2017.

Su, W., N.G. Loeb, L. Liang, N. Liu, and C. Liu, 2017: The El Niño-Southern Oscillation effect on tropical outgoing LW radiation: A daytime versus nighttime perspective. J. Geophys. Res., 122(15), 7820–7833 . doi:10.1002/2017JD027002.

Sun-Mack, S., P. Minnis, Y. Chen, S. Kato, Y. Yi, S.C. Gibson, P.W. Heck, and D.M. Winker, 2014: Regional apparent boundary layer lapse rates determined from CALIPSO and MODIS data for cloud-height determination. J. Appl. Meteor. Climatol., 53 (4), 990-1011.

Sundström, A.-M., A. Arola, P. Kolmonen, Y. Xue, G. de Leeuw, and M. Kulmala, 2015: On the use of a satellite remote-sensing-based approach for determining aerosol direct radiative effect over land: a case study over China. Atmos. Chem. Phys., 15(1), 505-518 . doi:10.5194/acp-15-505-2015.

Susskind, J., G. Molnar, L. Iredell, and N.G. Loeb, 2012: Interannual variability of outgoing LW radiation as observed by AIRS and CERES. J. Geophys. Res., 117(D23), D23107. doi:10.1029/2012JD017997.

Suttles, J. T., R.N. Green, P. Minnis, G.L. Smith, W.F. Staylor, B.A. Wielicki, I.J. Walker, D.F. Young, V.R. Taylor, and L.L. Stowe, 1988: Angular radiation models for Earth-atmosphere system: Volume I - Shortwave radiation. NASA Rep. RP-1184, NASA, Washington, DC, 144 pp.

Suttles, J. T., R. N. Green, G. L. Smith, B. A. Wielicki, I. J. Walker, V. R. Taylor, L. L. Stowe, 1989: Angular radiation models for the Earth-atmosphere system, 2, LW radiation. NASA Ref. Publ., RP-1184-Vol 2, [Online]. Available: https://hdl.handle.net/2060/19890011216.

Taylor, R., and L.L. Stowe, 1984: Reflectance characteristics of uniform Earth and cloud surface derived from Nimbus 7 ERB. J. Geophys. Res., 89, 4987-4996.

Thomas S., K. J. Priestley, N. Manalo-Smith, N. G. Loeb, P. C. Hess, M. Shankar, D. R. Walikainen, Z. P. Szewcyzk, R. S. Wilson, D. L. Cooper, 2010: Characterization of the Clouds and the Earth's Radiant Energy System (CERES) sensors on the Terra and Aqua spacecraft, Proc. SPIE, Earth Observing Systems XV, Vol. 7807, 780702, August 2010.

Tobin, D., R. Holz, F. Nagle, and H. Revercomb (2016), Characterization of the Climate Absolute Radiance and Refractivity Observatory (CLARREO) ability to serve as an infrared satellite intercalibration reference, J. Geophys. Res. Atmos., 121, doi:10.1002/2016JD024770.

Trenberth, K.E., J.T. Fasullo, K. von Schuckmann, L. Cheng, 2016: Insights into earth's energy imbalance from multiple sources. J. Clim. 29, 7495–7505.

Trenberth, K. E., Belward, A., Brown, O., Haberman, E., Karl, T. R., Running, S., Ryan, B., Tanner, M., & Wielicki, B. A., 2013: Challenges of a sustained climate observing system. In G. R. Asrar & J.W. Hurrell (Eds.), Climate Science for Serving Society: Research, Modeling, and Prediction Priorities (p. 480). Springer Press.

Trenberth, K.E., and J.T. Fasullo, 2013: An apparent hiatus in global warming? Earth's Future. 1, 19-32.

Trenberth, K.E., 2009: An imperative for climate change planning: tracking Earth's global energy. Current Opinion in Environmental Sustainability, 1:19–27.

Trenberth, K. E., J.T. Fasullo, M.A. Balmaseda, 2014: Earth's Energy Imbalance. J. Clim., 27 (9), 3129-3144.

Trenberth, K.E., and J.T. Fasullo, 2009: Changes in the flow of energy through the Earth's climate system. Meteor. Zeitsch., 18, 369-377. Doi: 10.1127/0941-2948/2009/0388.

Trepte, Q., P. Minnis, and R.F. Arduini, 2002: Daytime and nighttime polar cloud and snow identification using MODIS data. In Proc. SPIE 3rd Intl. Asia-Pacific Environ. Remote Sens. Symp., Hangzhou, China, 2002; Vol. 4891, pp 449–459.

Trepte, Q. Z., P. Minnis, C. R. Yost, S. Sun-Mack, and Y. Chen, 2018: Global cloud detection for CERES Edition 4 using Terra and Aqua MODIS data. J. Atmos. Oceanic Technol. (in preparation).

Tselioudis, G., B. Lipat, D. Konsta, K. Grise, and L. Polvani, 2016: Midlatitude cloud shifts, their primary link to the Hadley cell, and their diverse radiative effects. Geophys. Res. Lett., 43, no. 9, 4594-4601, doi:10.1002/2016GL068242.

von Schuckmann, K., M.D. Palmer, K.E. Trenberth, A. Cazenave, D. Chambers, N. Champollion, J. Hansen, S.A. Josey, N. Loeb, P.-P. Mathieu, B. Meyssignac, and M. Wild, 2016: An imperative to monitor Earth's energy balance. Nature Clim. Change, 6, 138-144. DOI: 10.1038/NCLIMATE2876.

Vonder Haar, T.H., and V.E. Suomi, 1971: Satellite observations of the Earth's radiation budget. Science, 163, 667-669.

Vonder Haar, T.H., and V.E. Suomi, 1971: Measurements of the Earth's radiation budget from satellites during a five-year period. Part I: Extended time and space means. J. Atmos. Sci., 28, 305-314.

Wang, Y., and G. J. Zhang, 2016: Global climate impacts of stochastic deep convection parameterization in the NCARCAM5, J. Advances in Modeling Earth Systems, https://doi.org/10.1002/2016MS000756.

Weatherhead, E.C., et al., 2018: Designing the Climate Observing System of the Future, Earth's Future, 6, 80–102, https://doi.org/10.1002/2017EF000627.

Weaver, W. L., and F. B. House, 1979: Analyses of earth radiation budget data from unrestricted broadband radiometers on the ESSA 7 satellite. NASA Technical. Paper, TP-1402, [Online]. Available: https://hdl.handle.net/2060/19790014538.

Weinstein, M., and V.E. Suomi, 1961: Analysis of satellite infrared radiation measurements on a synoptic scale. Monthly Weather Review, 89, 419-428.

Wielicki, B. A., and R.N. Green, 1989: Cloud identification for ERBE radiative flux retrieval. J Appl Meteorol 1989, 28 (11), 1133-1146.

Wielicki, B. A., T. Wong, R. P. Allan, A. Slingo, J. T. Kiehl, B. J. Soden, C. T. Gordon, A. J. Miller, S.-K. Yang, D. A. Randall, F. Robertson, J. Susskind, and H. Jacobowitz, 2002: Evidence for Large

Decadal Variability in the Tropical Mean Radiative Energy Budget. Science, vol. 295, no. 5556, 841-844, DOI:10.1126/science.1065837.

Wielicki, B. A., E.F. Harrison, R.D. Cess, M.D. King, D.A. Randall, 1995: Mission to Planet Earth: Role of Clouds and Radiation in Climate, Bull. Amer. Met. Soc., 76(11), 2125-2153. doi:10.1175/1520-0477(1995)076<2125:MTPERO>2.0.CO;2.

Wielicki, B.A., B.R. Barkstrom, E.F. Harrison, R.B. Lee III, G.L. Smith, and J.E. Cooper, 1996: Clouds and the Earth's Radiant Energy System (CERES): An Earth Observing System Experiment, Bull. Amer. Meteorol. Soc., 77, 853–868.

Wielicki, B. A., et al., 2013: Climate Absolute Radiance and Refractivity Observatory (CLARREO): Achieving Climate Change Absolute Accuracy in Orbit. Bull. Amer. Met. Soc., 93, 1519-1539.

Wielicki B. A., David R. Doelling, David F. Young, Norman G. Loeb, Donald P. Garber, and David G. MacDonnell, 2008: Climate Quality Broadband and Narrowband Solar Reflected Radiance Calibration Between Sensors in Orbit. IEEE IGARRS, July 2008, 4pp.

Wong, T., G.L. Smith, S. Kato, N.G. Loeb, G. Kopp, and A.K. Shrestha, 2018: On the lessons learned from the operations of the ERBE nonscanner instrument in space and the production of the nonscanner TOA radiation budget dataset. IEEE Trans. Geosci. Rem. Sens., doi:10.1109/TGRS.2018.2828783.

Wong, T., B.A. Wielicki, R.B. Lee, G.L. Smith, K.A. Bush, J.K. Willis, 2006: Reexamination of the observed decadal variability of the Earth radiation budget using altitude-corrected ERBE/ERBS nonscanner WFOV data. J. Climate, 19(16), 4028-4040. doi:10.1175/JCLI3838.1.

Xiong, X., A. Angal, A. Wu, W. Barnes, and V. Salomonson, 2016: Terra and Aqua MODIS instrument performance, IEEE Trans. Geosci. Rem. Sens., 7388 – 7391.

Yan, X.-H., T. Boyer, K. Trenberth, T. R. Karl, S.-P. Xie, V. Nieves, K.-K. Tung, and D. Roemmich, 2016: The global warming hiatus: Slowdown or redistribution?, Earth's Future, 4, 472–482, doi:10.1002/2016EF000417.

Yorks, J.E.; M. McGill, S. Rodier, M. Vaughan, Y. Hu, and D. Hlavka, 2009: Radiative effects of African dust and smoke observed from Clouds and the Earth's Radiant Energy System (CERES) and Cloud-Aerosol Lidar with Orthogonal Polarization (CALIOP) data. J. Geophys. Res., 114(D4), D00H04. doi:10.1029/2009JD012000.

Young, D. F., P. Minnis, G.G. Gibson, D.R. Doelling, and T. Wong, 1998: Temporal interpolation methods for the clouds and Earth's Radiant Energy System (CERES) Experiment. J. Appl. Meteorol., 37, 572-590.

Zhang, J., S.A. Christopher, L.A. Remer, and Y.J. Kaufman, 2005: Shortwave aerosol radiative forcing over cloud-free oceans from Terra: 2. Seasonal and global distributions. J. Geophys. Res., 110(D10), D10S24. doi:10.1029/2004JD005009.

Zhang, X., S. Liang, G. Wang, Y. Yao, B. Jiang, and J. Cheng, 2016a: Evaluation of the reanalysis surface incident shortwave radiation products from NCEP, ECMWF, GSFC, and JMA using satellite and surface observations, Remote Sensing, 8 (3), 225, http://doi.org/10.3390/rs8030225.

Zhang, Y.-C., W. B. Rossow, A. A. Lacis, V. Oinas, and M. I. Mishchenko (2004), Calculation of radiative fluxes from the surface to top of atmosphere based on ISCCP and other global data sets: Refinements of the radiative transfer model and the input data, J. Geophys. Res., 109, D19105, doi:10.1029/2003JD004457.

Zhao, T. X.-P., Yu, H., Lazlo, I., Zhin, M., and Conant, W., 2008: Derivation of component aerosol direct radiative forcing at the top of atmosphere for clear-sky oceans, J. Quant. Spectrosc. Radiat. Transfer, 109, 1162–1186.

Zhou, C., M. D. Zelinka, A. E. Dessler, and S. A. Klein, 2015: The relationship between interannual and long-term cloud feedbacks, Geophys. Res. Lett., 42, 10,463–10,469, doi:10.1002/2015GL066698.

Zhou, C., M. D. Zelinka, and S. A. Klein, 2016: Impact of decadal cloud variations on the Earth's energy budget, Nature Geoscience, 9, 871–874, doi:10.1038/ngeo2828.

Zhou, C., M. D. Zelinka, and S. A. Klein, 2017: Analyzing the dependence of global cloud feedback on the spatial pattern of sea surface temperature change with a Green's Function approach, J. Adv. Model. Earth Syst., 9, 2174–2189, doi:10.1002/2017MS001096.

List of Acronyms

ADM	Angular Distribution Model
ADRE	Aerosol Direct Radiative Effect
ADRF	Aerosol Direct Radiative Forcing
AIRE	Aerosol Indirect Radiative Effect
AMSR-E	Advanced Microwave Scanning Radiometer for EOS
AO	Announcement of Opportunity
AOD	Aerosol Optical Depth
$ASIC^3$	Achieving Satellite Instrument Calibration for Climate Change
ATBD	Algorithm Theoretical Basis Document
BDS	BiDirectional Scan
CALIPSO	Cloud-Aerosol Lidar and Infrared Pathfinder Satellite Observation
CCSDS	Consultative Committee for Space Data Systems
CDR	Climate Data Record

CERB	Continuity of Earth Radiation Budget
CERES	Clouds and the Earth's Radiant Energy System
CLARREO	Climate Absolute Radiance and Refractivity Observatory
CMIP	Coupled Model Intercomparison Project
CRE	Cloud Radiative Effect
DS	Decadal Survey
EBAF	Energy Balanced and Filled
EDOS	EOS Data and Operations System
EEI	Earth's Energy Imbalance
EOS	Earth Observing System
ERB	Earth Radiation Budget
ERBE	Earth Radiation Budget Experiment
ERBS	Earth Radiation Budget Satellite
ESD	Earth Science Division
EUMETSAT	European Organization for the Exploitation of Meteorological Satellites
EV	Earth Venture
EVC	Earth Venture-Continuity
EVI	Earth Venture-Instrument
EVM	Earth Venture-Mission
EVS	Earth Venture-Suborbital
FACA	Federal Advisory Committee Act
FM	Flight Model
GCM	General Circulation Model
GCOS	Global Climate Observing System
GERB	Geostationary Earth Radiation Budget
GSICS	Global Space-Based Intercalibration System
ICM	Internal Calibration Module
IPCC	Intergovernmental Panel on Climate Change
JPSS	Joint Polar Satellite System
LW	LW
MAM	Mirror Attenuator Mosaic
MLT	Mean Local Time
MODIS	Moderate Resolution Imaging Spectroradiometer
NFBB	NFOV Blackbody
NFOV	Narrow Field-Of-View
NASA	National Aeronautics and Space Administration
NASEM	National Academies of Sciences, Engineering, and Medicine
NCDC	National Climate Data Center
NCEI	National Centers for Environmental Information
NOAA	National Ocean and Atmospheric Adminstration
NRC	National Research Council
OLR	Outgoing LW Radiation
PAP	Programmable Azimuth Plane
PDO	Pacific Decadal Oscillation

PFM	Proto-Flight Model
PI	Principal Investigator
PSF	Point-Spread Function
RAP	Rotating Azimuth Plane
RBI	Radiation Budget Instrument
RBSP	Radiation Budget Science Project
RCF	Radiometric Calibration Facility
RCP	Representative Concentration Pathways
RMS	Root-Mean-Square
RMSE	Root-Mean-Square Error
RSR	Reflected Solar Radiation
ScaRaB	Scanner Radiation Budget
SFC	Surface
SI	Système Internationale
SNPP	Suomi National Polar-orbiting Partnership
SNO	Simultaneous Nadir Overpass
SORCE	Solar Radiation and Climate Experiment
SRF	Spectral Response Function
SSF	Single Scanner Footprint
SST	Sea-Surface Temperature
SW	Shortwave
SWG	Science Working Group
SWICS	Shortwave Internal Calibration Source
SWRS	Shortwave Reference Source
TACR	Transfer Active Cavity Radiometer
TOA	Top-Of-Atmosphere
TOT	Total
TRMM	Tropical Rainfall Measuring Mission
VIIRS	Visible Infrared Imaging Radiometer Suite
VIRS	Visible and Infrared Scanner
WFOV	Wide Field-Of-View
WN	Window